SANDIA REPORT
SAND2020-10124
Printed September 2020

Sandia National Laboratories

Dispersion Validation for Flow Involving a Large Structure Revisited: 45 Degree Rotation

Alexander L. Brown, Blake W. Lance, Michael Clemenson, Samuel T. Jones, Michael Benson, Chris Elkins

Prepared by
Sandia National Laboratories
Albuquerque, New Mexico
87185 and Livermore,
California 94550

Issued by Sandia National Laboratories, operated for the United States Department of Energy by National Technology & Engineering Solutions of Sandia, LLC.

Available to DOE and DOE contractors from
U.S. Department of Energy
Office of Scientific and Technical Information
P.O. Box 62
Oak Ridge, TN 37831

Telephone: (865) 576-8401
Facsimile: (865) 576-5728
E-Mail: reports@osti.gov
Online ordering: http://www.osti.gov/scitech

Available to the public from
U.S. Department of Commerce
National Technical Information Service
5301 Shawnee Rd
Alexandria, VA 22312

Telephone: (800) 553-6847
Facsimile: (703) 605-6900
E-Mail: orders@ntis.gov
Online order: https://classic.ntis.gov/help/order-methods/

ABSTRACT

The atmospheric dispersion of contaminants in the wake of a large urban structure is a challenging fluid mechanics problem of interest to the scientific and engineering communities. Magnetic Resonance Velocimetry (MRV) and Magnetic Resonance Concentration (MRC) are relatively new techniques that leverage diagnostic equipment used primarily by the medical field to make 3D engineering measurements of flow and contaminant dispersal. SIERRA/Fuego, a computational fluid dynamics (CFD) code at Sandia National Labs is employed to make detailed comparisons to the dataset to evaluate the quantitative and qualitative accuracy of the model. This work is the second in a series of scenarios. In the prior work, a single large building in an array of similar buildings was considered with the wind perpendicular to a building face. In this work, the geometry is rotated by 45 degrees and improved studies are performed for simulation credibility. The comparison exercise shows conditionally good comparisons between the model and experiment. Model uncertainties are assessed through parametric variations. Various methods of quantifying the accuracy between experiments and data are examined. Three-dimensional analysis of accuracy is performed. The effort helped identify deficiencies in the techniques used to make these comparisons, and further methods development therefore becomes one of the main recommendations for follow-on work.

ACKNOWLEDGEMENTS

Michael Brown (at Los Alamos National Laboratory) consulted on the design and selection of test conditions for the experiment. We acknowledge the work of the testing team, including students Nick DiVito, Matt Byers, and Will White. Programmatic support came from the CIESESE internship program, as well as from other programmatic sponsors. Connor Laktasic and Arturo Rodriguez supported the computational work as summer interns. Programmatic interest from the Defense Threat Reduction Agency (DTRA), and Jon Rogers (SNL) were key to the progress and completion of this study. Heeseok Koo (SNL) and Ethan Zepper (SNL) provided helpful guidance key to completion of this activity. Andrew Glen and Andrew Kurzawski provided reviews of the manuscript, and Stan Mathews provided a technical edit.

CONTENTS

LIST OF FIGURES

LIST OF APPENDIX FIGURES

LIST OF TABLES

This page left blank

ACRONYMS AND DEFINITIONS

Abbreviation	Definition
2D	2 Dimensional
3D	3 Dimensional
CFD	Computational Fluid Dynamics
CFL	Courant-Friedrichs-Lewy
CV	Control Volume
CVFEM	Control Volume Finite Element Method
FFT	Fast Fourier Transform
LANL	Los Alamos National Laboratory
LES	Large Eddy Simulation
MRC	Magnetic Resonance Concentration
MRI	Magnetic Resonance Imaging
MRV	Magnetic Resonance Velocimetry
MUSCL	Monotonic Upwind Scheme for Conservation Laws
PIV	Particle Image Velocimetry
RANS	Reynolds Averaging of the Navier-Stokes equations
SNL	Sandia National Labs
TFNS	Temporal-Filtered Navier-Stokes
UPW	Upwinding
USMA	United States Military Academy
V&V	Verification and Validation

1. INTRODUCTION

The release of toxic substances into the atmosphere can have adverse effects on the population and environment. With increasing population and the variety of activities for which this phenomenology is significant, it becomes increasingly important to understand and predict contaminant dispersion in highly populated areas. Improved understanding can help to mitigate potential negative health and environmental effects.

Contaminants may originate from ordinary sources, such as emissions from vehicles (e.g. Brown and Dabbert, 2003), and exhaust stacks from structures (e.g., Saathoff et al., 2009). Improved understanding of contaminant transport from these sources can affect design and construction. Sources may also originate from a deliberate or accidental release of harmful chemical agents (e.g., Heist et al., 2009; Brixey et al., 2009). Understanding how contaminants are influenced by urban geometries can aid government agencies to prepare an emergency response in the event of a chemical attack or unintended release.

This report builds on and is subsequent to a prior report (Brown and Benavidez, 2018) which details a simulation exercise that was performed to compare simulated dispersal of a contaminant in a water flow to novel test data from the MRC/MRV technique. The simulations in the prior report focused on the first of several scenarios of interest. A uniform array of square structures was conceived with a single structure much taller than the others. A contaminant is released down-wind of the tall structure in a flow characteristic of a wind environment. In the Brown-Benavidez report, comparisons between the model and data are made for iso-contours, planes, lines, and points. The concentration data compare very well for adequately resolved transient models, and the velocity data suggest the main features of the flow are captured in the model. This report differentiates from the first in that the second test scenario is the topic of interest. The second scenario is identical to the first except that the domain is rotated 45 degrees such that the upwind point of each building is a corner, not a face. Another differentiating factor is increased exposure to the results from the experimental team through full 3D comparisons. Shim et al. (2018) detail an experimental analysis of the flow from the two urban contaminant scenarios. They include different analysis methods, and exhibit different features of the flow. This report will take advantage of the additional information on the data (i.e. a more complete dataset with a more detailed analysis) to apply different methods of analyzing the data.

This report is also differentiated by the fact that additional attention is paid to validation methods through a more detailed study including experimental and numerical uncertainty estimation, a separate parameter study, and perspectives on solution verification via a grid convergence study. These studies increasingly follow Verification, Validation, and Uncertainty Quantification standards.

1.1. Background and Literature Review

This section mirrors the background and literature review from Brown and Benavidez (2018). A few modifications and updates have been made, but it largely duplicates the prior review.

The urban environment is particularly challenging because of the complexity of the surface layer. Buildings are constructed in a variety of shapes and orientations. There are a wide variety of arrangements of buildings. There is an effect of the urban structures on the atmospheric boundary layer that is a necessary consideration for bounded domain predictions (e.g. Lateb et al. 2016). The urban boundary layer is significantly different from the rural boundary layer, an effect that is caused by the urban structures. It is typically thicker, extending higher than would be normally expected in a

rural or suburban setting. Urban dispersion is often governed by the characteristic length scales in the turbulent urban boundary layer (Lateb et al. 2016; Franzese and Huq, 2011).

Urban structures also can significantly impact the mixing and dispersion in their immediate vicinity, and there has been a focus in the recent literature on scenarios involving a single structure significantly taller than the surrounding structures. Here some specific examples of recent activity are given. Heist et al. (2009) and Brixey et al. (2009) detail scaled wind tunnel experiments and Computational Fluid Dynamics (CFD) simulations that were motivated by a field study of a Brooklyn, NY, USA urban dispersion exercise. They were motivated by findings that the large structure significantly enhanced vertical dispersion in the wake region. Addepalli and Pardyjak (2015) used a wind tunnel with approximately a 1 meter cross-section and a scaled domain to study the effect of a tall structure. Particle Image Velocimetry (PIV) was used to extract planar velocities mostly between a single tall structure and a down-stream structure of varying heights. Hayati et al. (2017) explore simulation comparisons to the dataset using three modeling techniques. Two Navier-Stokes based CFD solvers including Large Eddy Simulation (LES) and Reynolds Averaging of the Navier-Stokes equations (RANS) methods were used, along with QUIC-URB, which uses mass consistency to approximate a flow field. Tominaga et al. (2008) detail working group results from the Architectural Institute of Japan, which focuses on the use of CFD to model the pedestrian wind environment. Several of their characteristic qualification problems involve tall structures. Pascheke et al. (2008) tested scale wind-tunnel dispersion using naphthalene sublimation and propane point sources with equal-height structure and variable height structure urban configurations. They found the variable height structures contributed to increased lateral and vertical plume spread. Xie et al. (2008) examined flow around variable height structures, and found that the flows were complex and that the tallest structures can have a disproportionate effect on the turbulence in their wakes.

The scenario of a single taller building is challenging because the dispersion (particularly vertical) is enhanced due to the turbulence formed in the wake of the large building. The enhanced dispersion challenges modeling techniques that do not appropriately resolve the turbulent behavior. Such geometry therefore represents a good quality metric for detailed simulation capabilities.

As already noted in some of the above examples, scaling is often used to study large and complex flow geometries that are difficult to study natively. The primary parameter for flow scaling is the Reynolds number, which is the self-similarity parameter relating momentum to viscous forces. In the case of air flow, one studies a smaller scaled geometry at a higher velocity to maintain similar Reynolds number for the flow conditions. Altering the fluid can change density and viscosity, the other two component parameters of the Reynolds number. Flows relevant to large-scale domains can be reproduced at a much smaller scale. Reynolds number matching still results in self-similar results provided that other properties of the fluids are reasonably inconsequential to the flow characteristics. Thus, air flows can, to a first order, be approximated with liquids by maintaining the appropriate scaling and conditional requirements. Regimes where surrogacy might become increasingly questionable would include where compressibility effects become significant, and where density gradients such as thermal variations significantly affect the buoyancy in a flow. The compressibility of air compared to water is significantly different. Froude or Richardson number scaling might be more appropriate and/or significant in some applications of this nature because they include buoyancy effects and density gradient effects. Diffusional effects are often computationally managed through the Schmidt number, which relates viscous and diffusional flow effects. The Schmidt number is also a parameter of interest relating to the self-similarity approximation for turbulent dispersion problems. The Schmidt number may relate to laminar and/or turbulent properties depending on the model assumptions.

A notable example of utilizing a water flow as a surrogate for a gas flow is found in Laskowski et al. (2007). Here, a mixed convection turbulent flow scenario was developed experimentally to study the turbulence and heat transfer from the flow in a water channel with the aim of validating CFD models for heat transfer in a fire application. Richardson number scaling was primarily observed for these flows. The convective heat transport to a cylinder was monitored, having components of natural and forced convection contributing to the heat transfer. Water flow was used as a validation exercise with the intent of using the modeling tools later for gas flow conditions involving similar phenomenology. Experimental data included 2-dimensional (2D) PIV and heat flux deduced from thermal measurements around the perimeter of a cylinder in the flow.

The medical field and the diagnostic requirements thereof have led to several well-established non-invasive methods for probing 3-dimensional (3D) complex systems. One technique that has thus far had limited application to engineering problems is Magnetic Resonance Imaging (MRI). Elkins et al. (2003, 2004, 2009), Elkins and Alley (2007), Chang et al. (2009), and Benson et al. (2011) detail some of the prior application of the existing technology in the medical industry to flows of engineering interest. MRI equipment uses nuclear magnetic resonance tuned to the hydrogen atom and tomographic reconstruction to extract sub-millimeter resolved concentration and flow information. MRI equipment is scaled for human body interrogation, and because of the strong magnetic fields is limited to materials that are compatible with the environment (non-ferromagnetic). The primary advantage of this technique is the existence of apparatus and post-processing tools to readily interpret test conditions. The technique was recently applied to a series of flow conditions motivated by the atmospheric dispersion literature described above in collaboration with the modeling team at Sandia. A notional geometry was generated to produce flows involving dispersion of a contaminant down-wind of a very tall structure in a mock urban setting. Shim et al. (2019) published a report of the results of the 90 and 45 degree experimental study. This paper provides additional information on the configuration, operation, set-up, and output from the testing program to which this simulation exercise is making comparisons.

The presence of detailed scaled data on the flow behavior of a domain motivated by the atmospheric dispersion of contaminants downwind of a tall structure provides the unique opportunity to explore the computational accuracies obtained from simulation tools. The validation exercise circumvents some of the main issues of many of the prior validation exercises. The principal boundary condition is well characterized in 2-dimensions. The domain results are fully 3-dimensional, and include velocity and concentration time-means. Reynolds number scaling is observed to produce a flow representative of characteristic atmospheric conditions. Comparisons between simulations and data are not constrained to experimentally pre-selected locations of interest. Data exist throughout the domain in scan regions of interest.

This study computationally examines flow and dispersion around a tall building in an otherwise uniform array of cubical buildings. The presence of the one tall building influences significantly the surrounding velocity fields and contaminant dispersion. Comparisons are made between predictions employing a variety of modeling assumptions and the detailed dataset. The results are intended to expose model limitations, characterize expected model accuracy and provide confidence in the ability to simulate dispersion events in a complex flow environment. This scenario was selected because it relates to past studies of similar geometric configurations (e.g., Heist et al., 2009 and Brixey et al., 2009), and is the first of several scenarios expected to be simulated using the combined MRV/MRC and SIERRA/Fuego techniques.

1.2. Objectives

The main objectives of this work are:

1. Generate simulations corresponding to the 45 degree MRC/MRV data.

2. Repeat the analysis done in the 90 degree simulation campaign with modifications targeted towards improving the assessment quality.

3. Draw inferences related to the validation of the simulation software based on the comparison with data.

4. Assess methods and propose alternate methods for this type of activity.

5. Develop recommendations for follow-on work and improvements to the activity.

2. METHODS

2.1. Experimental Configuration

This study considers the experimental configuration developed in collaboration with the United States Military Academy (USMA) and Stanford University. Experimental data were collected in a scaled down meteorological EPA wind-tunnel placed inside a Magnetic Resonance Imaging machine. The upstream section of the water channel is composed of roughness layers and a Counihan vortex generator designed to generate turbulence and simulate atmospheric conditions before reaching the test section. Roughness layers included an array of Lego ™ blocks arranged uniformly on the floor of the channel. The test section was printed using a 3D print technology, and the same geometry representations delivered to the printing systems could be adapted to generate the computational meshes of the flow area (see Figure 2-1). The 3D printing was done with a 3D Systems Viper Stereolithography machine with an Accura 60 resin from 3D systems. The resolution was 0.004 inches (0.10 mm) in the x/y plane with 0.010 inch (0.254 mm) layers.

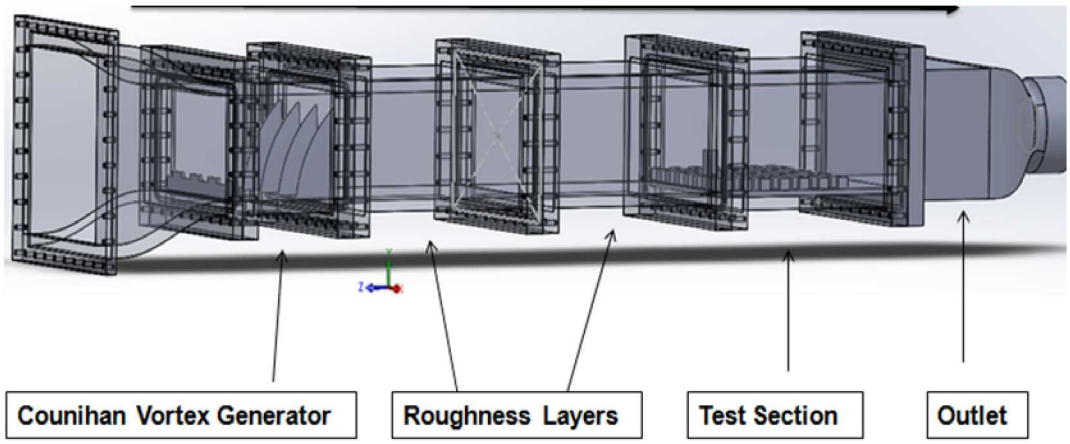

Figure 2-1. Water Channel Design

The test domain was proposed by Mike Brown (Los Alamos National Laboratory, or LANL), who was a participant in some of the past studies on atmospheric flow described in the introduction (and based on prior detailed literature). The test section (illustrated in Figure 2-2) was manufactured from a non-ferrous resin using stereolithography . It is 196 mm wide, 110 mm high and 239 mm long (internal flow dimensions). The mock buildings are arranged in an evenly spaced array. The uniform cubical buildings have a characteristic length of L=12.25mm. The tallest building is of the same length and width and with a height of 36.75mm, three times that of the surrounding structures (3L). The gap between the buildings is the same characteristic length (L). The tall building is centered in the x-direction, and in the second row of buildings in the z-direction (flow direction). The contaminant injection site is located immediately downstream of the tallest building. The contaminant is injected directly into the water channel through holes drilled over the top of a 12.25 mm x 12.25 mm injector located down-stream of the tall building at the channel floor. The contaminant, an aqueous solution of Copper (II) Sulfate ($CuSO_4$), is injected at a low constant flow rate of 0.4L/min compared to a bulk flow rate of 410L/min. This was done to limit the disruption of the bulk flow by the contaminant injection. Concentration measurement resolution limitations exist, so multiple tests were simulated with different contaminant concentrations. The resultant data were scaled and stitched together to give a more comprehensive range of contaminant

measurements. The baseline specific gravity of the aqueous solution was 1.003, and an elevated specific gravity was employed for higher resolution data (1.015). There are not expected to be significant density variations and buoyancy effects in the tests, as density variations are minimal. The water (including both inlet streams) was maintained at a constant temperature of 21°C throughout testing. The entire test section was scanned by the MRI machine to collect average velocity and concentration data. Scans were conducted immediately upstream of the buildings to collect initial condition data for numerical simulations at the interface between the test section and the roughness layer section. During Magnetic Resonance Concentration (MRC) measurements, a waste water reservoir was incorporated to prevent the concentration of contaminant in the bulk flow from rising over time as would occur if recirculation were used.

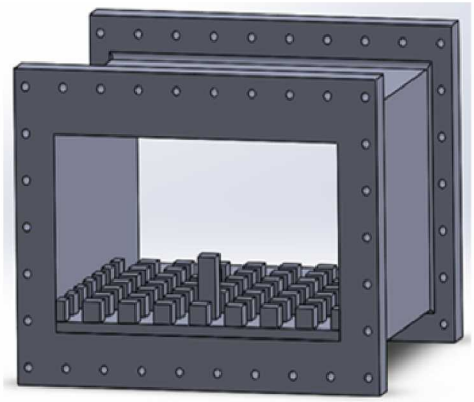

Figure 2-2. Test Section Geometry Image form the 90 Degree Simulation Work

The MRI technique (MRV and MRC) is able provide a data resolution of 0.8mm. Such resolution data exist throughout the test section, however in this comparison effort only a subset of the experimental data are evaluated primarily via detailed line comparisons. The rich nature of the data is not typical of CFD validation comparison studies. With the new richness of data, there is a need for methods to be developed, discovered, or identified (if existing in other fields) that can be used for more comprehensive validation comparisons between the 3D simulation and the 3D experiment results. Data accuracies have been assessed, and preliminary estimates suggest the velocity data are accurate to 6%, and concentrations to 4%. These were provided by the test team, and it is expected that final figures will be independently documented and detailed by them in an independent forthcoming publication.

The CAD geometry from the test design team was passed to the modeling team. The fluid mesh was constructed from the same geometry file that was used to generate the 3D prints of the domain for the flow experiments. Figure 2-3 illustrates graphically the standard measurement locations as well as the general layout of the rotated configuration. Figure 2-4 shows a top view of the geometry. Rows A through I and columns 1 through 9 can be used to reference buildings as well as building gaps when discussing results. The red dashed line indicates principal measurement locations.

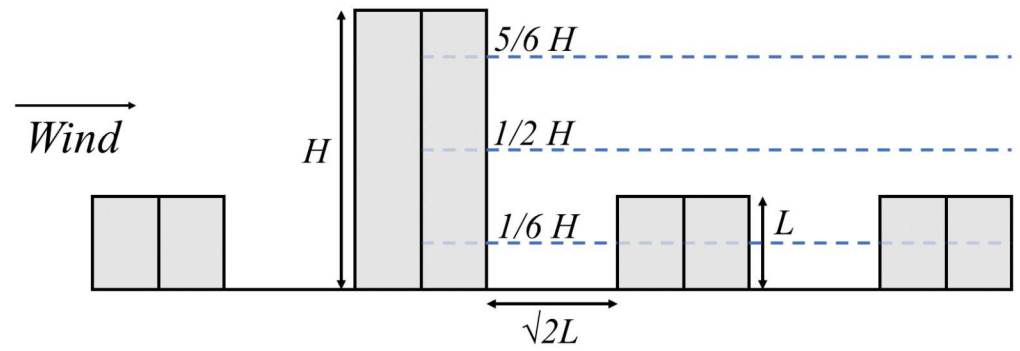

Figure 2-3. Side-View of the Test Section with Standard Measurement Elevations Indicated by the Dashed Lines

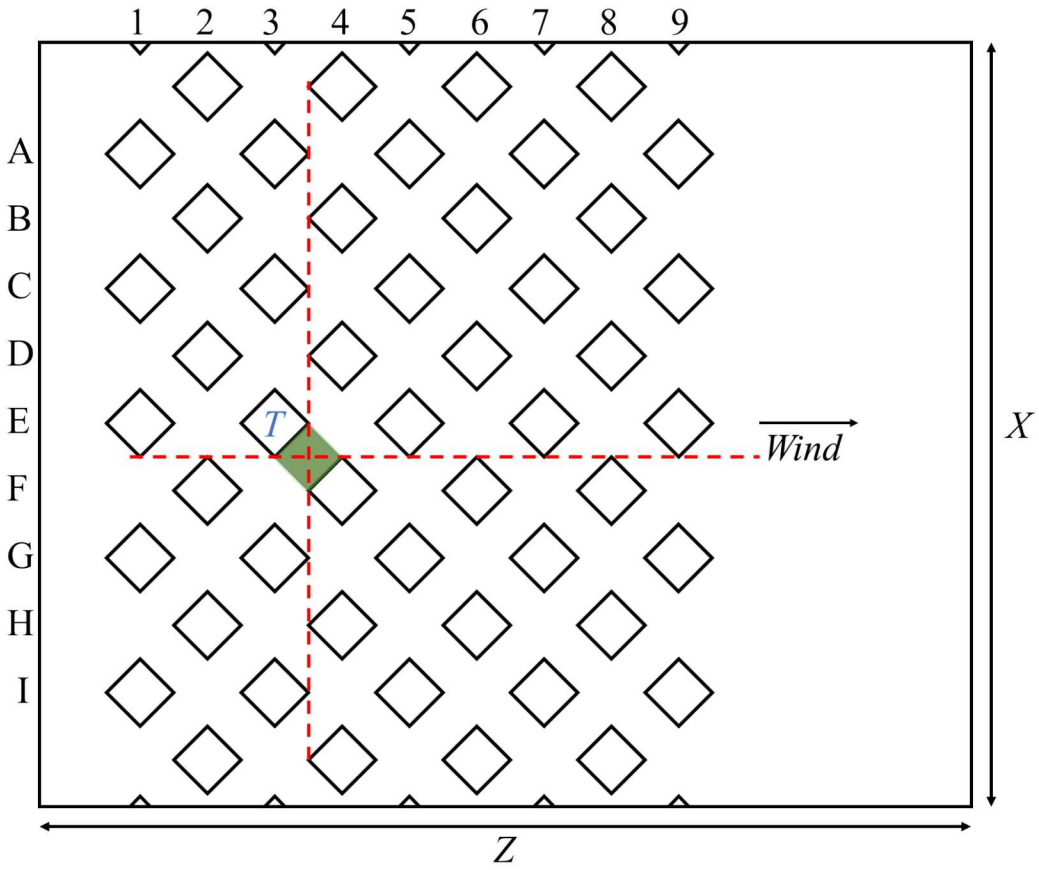

Figure 2-4. Top View of the Test Section with Row/Column Nomenclature and Standard Measurement Planes and Line Locations Illustrated by the Dashed Lines

2.2. Numerical Configuration

Sierra/Fuego, a low-Mach CFD code developed by Sandia National Laboratories, was used to conduct simulations (Sierra, 2017a and 2017b). Sierra is a general architecture for engineering computational tools developed and maintained at Sandia National Labs. Fuego is the low-Mach number CFD solver initially designed to predict fire behavior and conjugate heat transport to objects in the fire. It is particularly distinguished from other current fire CFD solvers in common

use in that it is a control volume finite element method (CVFEM) formulation rather than a pure control volume (CV) method. The code is massively parallel, and inherits the solver and numerical packages developed for Sierra which are aimed at supporting and leveraging advanced capabilities of evolving computer hardware. Fuego couples to other multi-mechanic codes in the same Sierra framework, however this capability is not necessary for this exercise. The solver is a segregated solver, and sequentially solves the governing continuity, momentum, turbulence, and mixture fraction equations. Within a timestep, the segregated solver would repeat for Time-Filtered Navier-Stokes (TFNS) and k-ε simulations to achieve improved timestep convergence.

All calculations for this study were performed with version 4.48.2 of the code, and simulations were run on a variety of the current high performance clusters at Sandia National Labs. The version is a differentiating factor between this study and the prior study with the 90 degree simulations, which were performed with version 4.46.2. There are no known differences between the versions that would be expected to result in major variations in the outcome, and release notes can be evaluated for details on code changes between versions. Corresponding documentation can be accessed for the equation set solved. No unique model variations or user subroutines were employed for this study.

2.2.1. Domain and Grid Size

The numerical domain is modeled based on the nominal conditions created for the experimental program, the CAD file that was used to 3D print the geometry for the tests. The simulation domain is 196 mm wide, 110 mm high and 239 mm long. The computational domain is composed of hexagonal grid elements of varying size. This mesh was more complicated than the 90 degree scenario mesh, which could be designed with fully orthogonal mesh elements. The 45 degree rotated buildings required elements conformal to the buildings in the inner part of the domain. This was achieved by first meshing the internal region with conformal hexahedrons, then at the boundaries of the mesh allowing adaptive algorithms to use distorted hexahedron mesh cells to conform to the boundary shape. A horizontal and vertical mesh bias scheme was utilized to yield a less computationally expensive domain with tapered mesh relaxation outside the region of primary interest. The inlet and outlet boundary conditions were placed more than H, the height of the tallest building, away from the edge of the buildings to avoid artificial acceleration near the boundaries.

A grid sensitivity study was performed to evaluate mesh convergence. Three meshes were generated to examine the solution sensitivity to mesh size (coarse, medium, fine). The coarse mesh contained 1.0 million cells with a uniform cell size of 1.5 mm. The medium mesh had a localized grid refinement closest to the target building yielding a local resolution of 0.5 mm and 3.6 million cells overall and was considered the baseline mesh during the parameter sensitivity study. The fine mesh contained 14 million cells with a local resolution of 0.375 mm closest to the tall building. Figure 2-5 shows the mesh for the baseline LES scenario. Hex element adaptation to rotate the mesh inside the domain was used, with the adapted regions near the model boundary conditions so as to minimally influence the flow in the domain. The adaptivity was not symmetric about the y-z plane. The $CuSO_4$ injection area is green in the surface structure plot. The time step for each mesh was determined by the smallest cell size. The time step was adjusted for each consecutive refinement such that the Courant-Friedrichs-Lewy (CFL) number did not significantly exceed 0.5. A fixed timestep was used. This helped assure stable flow, and provided a timestep consistent with the resolved flow on the mesh. Table 2-1summarizes mesh and timestep model parameters for simulations run for this study. Most cases were run with the medium mesh.

Table 2-1. Mesh and Timestep Details for Simulation Cases

Mesh	Cells (million)	High Resolution (mm)	Cases	Timestep (s)
Coarse	1.0	1.5	k-ε, LES (1)	0.0015
Medium	3.6	0.5	TFNS, LES (all others)	0.0005
Fine	14.0	0.375	LES (1)	0.000375

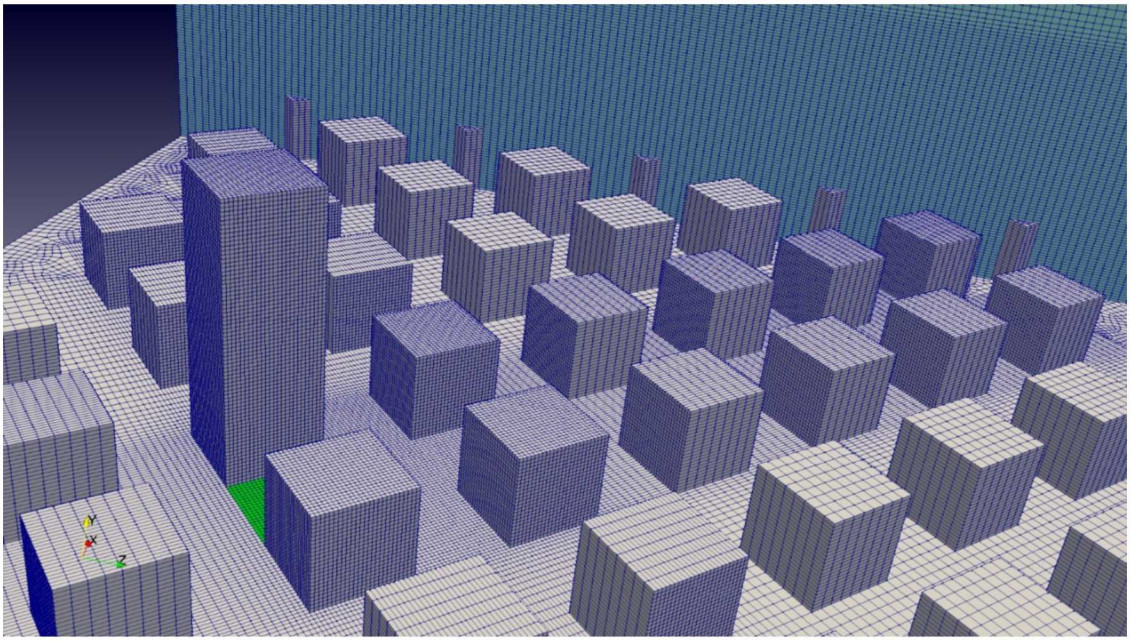

Figure 2-5. The Medium Mesh with the Inflow on the Left

A consistent coordinate system is used throughout this report. The z-direction is the direction of flow, and the flow is in the negative direction. The y-direction is vertical. The x-direction is span-wise. This is consistent with the coordinate system from the CAD model as drawn in Figure 2-1.

2.2.2. Turbulence Models

This study examined the performance of multiple turbulence models. The turbulence models considered for this study were k-ε, LES and TFNS. The aim of this study is to compare the results of different turbulence models and model parameters in comparison to experimental data and evaluate the accuracy of SIERRA/Fuego for applications of dispersion for urban flow geometries.

k-ε is a relatively inexpensive RANS method for simulating flows and is widely used in engineering applications. It was conceived in the 1960-1970 timeframe, and is meant to simulate scenarios with insufficient resolution to resolve the turbulent scales (e.g. Launder and Spalding, 1983, Jones and Launder, 1972). The standard k-ε model is a two-equation method which solves turbulent kinetic energy and rate of turbulent dissipation numerically through transport equations and treats turbulent viscosity as isotropic. Dispersion is related directly to the turbulent viscosity, which is augmented due to the increased dissipation modeled in the eddy dissipation. Thus, dispersion at the sub-grid scale is heavily linked to the turbulent parameters.

LES applies a spatial filter to the turbulent equations, resolving turbulence at the grid level and modeling sub-grid turbulence. Dispersion is primarily advective as resolved on the grid, with a lesser fraction of the dispersion relating to the turbulent viscosity through the sub-grid model. In our case, we utilize the KSGS model (Kim and Menon, 1997). A single equation turbulent kinetic energy model is used to simulate the sub-grid turbulence.

Time-Filtered Navier-Stokes (TFNS) is a hybrid method containing aspects of LES methods and standard RANS models. TFNS applies a time filter to limit the sub-grid scale turbulence. It bases the sub-grid scale on the standard k-ε model (Tieszen et al., 2005). It has been used mostly in the past at Sandia National Labs (SNL) for fire simulation applications, and to our knowledge is not widely adopted in the CFD community. Dispersion depends on the turbulent viscosity at the sub-grid level. Advective dispersal is resolved to the temporal filter. In the case of these simulations, the magnitude of the temporal filter selected was two times the timestep.

2.2.3. Mixture Fraction Approximation

A mixture fraction approximation was applied to model the contaminant dispersion throughout the numerical domain. The mixture fraction is the ratio of the amount of injected flow present in the bulk flow to the bulk flow originating at the primary inlet. A transport equation for scalar mixture fraction was used to model the dispersion of the contaminant. Constant properties with the surrounding water flow were assumed. This means that no buoyancy effects were resolved in the simulation. Buoyancy effects are anticipated to be negligible, as concentrations were insufficiently large to change the density by more than a few percent at the greatest.

Because both the experiment and model were optimized to give concentration levels in stream fractional magnitudes, we represent concentration in this way for the remainder of this report. Concentration for this study is therefore unitless, and represents more accurately stream mass fraction subject to a constant density approximation.

2.2.4. Boundary Conditions

MRV data were collected immediately upstream of the building array to provide velocity data to apply to the inlet boundary condition in the numerical model. The test team gave the modeling team instruction that the inflow conditions for the 45 degree and the 90 degree scenario were identical. Consequently, there is reason to consider replicating the activity for the 90 degree scenario analysis. That analysis used a piece-wise interpolation to approximate the 2D plane of velocity data, and propagated that to a series of boundary surfaces (horizontal stripes). The inflow boundary condition is simplified in this effort by mapping the inflow condition from the 90 degree work onto a planar mesh, and using a single upwind boundary condition onto which the flow condition is mapped. Figure 2-6 shows a graphical contour plot comparison between the numerical inlet velocity profile as applied in the models versus the measured experimental inlet profile. The inlet profile appears to be a reasonable approximation of the experimental condition. Stream-wise velocities from the experiments were applied at the inflow boundary. The other velocity components were relatively small, and omitted (assumed zero) in the simulation boundary conditions. An example input file is shown in Appendix A The Baseline Les Input Files, which contains the details of the inflow boundary condition implementation. The MRV data consisted of average flow conditions during the test, and lacked any fluctuations.

Because of the perforated plate and presumed pressure drop across the boundary, the contaminant injection site was assumed to be a single uniform bulk flow over a flat surface at the bottom of the

water channel floor. The fixed velocity condition was 0.044 m/s, and the turbulent kinetic energy was assumed to be low (1e-6 m^2/s^2). All incoming flows were considered isothermal at a temperature of 21°C with a constant density and viscosity. The test team took the concentration data during an injection, and took the velocity data with the injector replaced with a wall slug in place of the injector (no inflow). The results were stitched together in a data file for comparison with the simulations.

A.

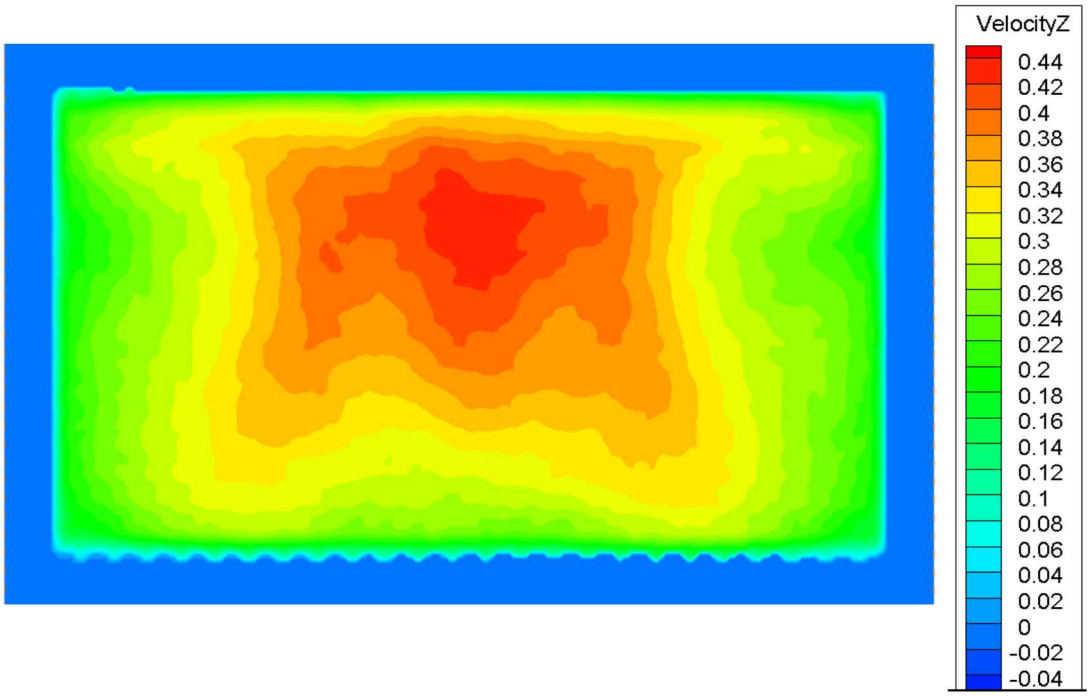

B.

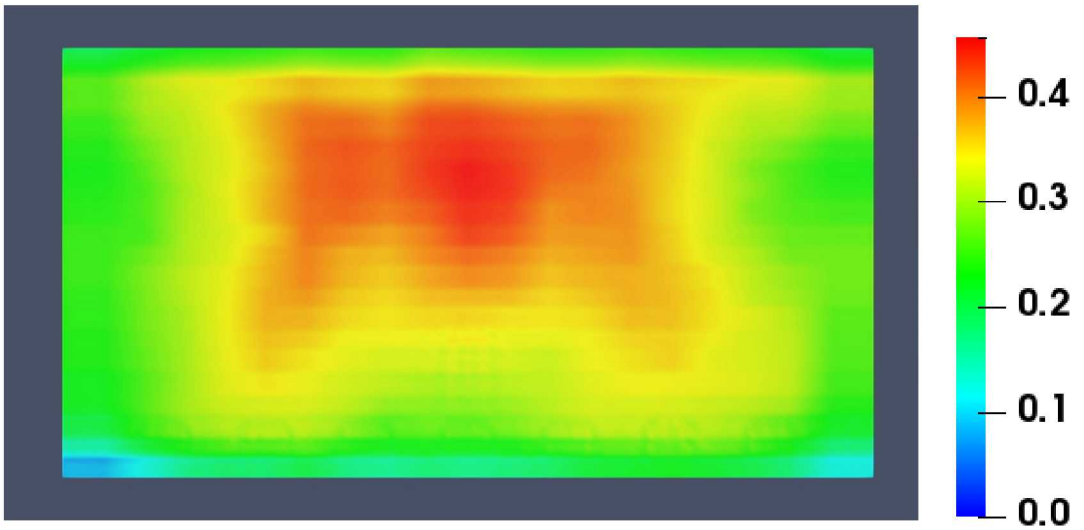

Figure 2-6. Inlet Velocity (m/s) Comparison (x-y plane) for data (A) and Model (B)

The walls and buildings within the simulation were treated as smooth walls with a no-slip condition applied. Wall functions were utilized to simulate the viscous effect of a developed turbulent boundary layer at the location of the wall in the first node perpendicularly above the flow. The adequacy of this assumption was assessed previously for the 90 degree scenario, and because velocity did not change it is presumed to be of similar sensitivity in this study.

2.3. 3D Comparison Metrics

We interpolate experimental results between a 0.8 mm data mesh and the computational medium mesh with slightly higher resolution in the focal region. Using this test case, the data were interpolated onto the model results, as well as vice-versa using the mesh_transfer capability in the Percept code developed at Sandia (Carnes and Kennon, 2016).

This comparison work was initially guided by the approach Hanna and Chang (2012) proposed for comparing campaign-level test results to simulations (heretofore referred to as HC-2012). They proposed the following metrics for assessing performance of computational models:

- The Fractional Mean Bias (FB): $2(\overline{C_o} - \overline{C_p})/(\overline{C_o} + \overline{C_p})$
- The Normalized Mean-Square Error (NMSE): $(C_o \bar{-} C_p)^2/(\overline{C_o} \times \overline{C_p})$
- The Geometric Mean (MG): $exp(\overline{lnC_o}) - exp(\overline{lnC_p})$
- The Geometric Variance (VG): $exp\overline{((lnC_o - lnC_p)^2)}$
- The Fraction of Predictions with in a Factor of 2 of the Observations (FAC2): $0.5<(C_p/C_o)<2$
- The Normalized Absolute Difference (NAD): $|\overline{C_o} - \overline{C_p}|/(\overline{C_o} + \overline{C_p})$

They propose an urban acceptance criteria of $|FB| < 0.67$, NMSE < 6, FAC2 > 0.3, and NAD < 0.5 for concentration data (c_p being the predicted variable and c_o being the observed). Under the assumption that these statistical parameter comparisons are agnostic to the type of variable, we apply these to the velocity as well.

We introduce in this context three additional measures for quantifying model and experimental differences. Two of these are identified as:

1. The local normalized difference (LND): $$LND = \frac{|C_p - C_o|}{max(C_p, C_o)}$$
2. The local logarithmic ratios (LLR): $$LLR = ln\left(\frac{max(C_p, C_o)}{min(C_p, C_o)}\right)$$

These two additional measures provide alternate expressions of accuracy. Both quantities approach zero for ideal comparisons. LND cannot exceed 1.0, which represents the worst-case comparison between model and experiment. LLR is not similarly bounded, however larger numbers represent poorer comparisons. These have advantages over many of the HC-2012 metrics in that they do not have terms in the denominator that depend on the entire dataset. Full dataset assessments can be made on the average values. The third additional measure is the square of the correlation coefficient. This is assessed on the raw velocity and concentration data, as well as on the relevant accuracy measures listed above and variable gradients including the vorticity and q-criterion. The R^2 term is the square of the correlation coefficient, also known as the coefficient of determination.

Preliminary evaluations suggested that the results of the 3D comparison analysis were reasonably equivalent regardless of the source/destination mesh. Figure 2-7 shows the concentration predictions from this initial comparison using a clipping threshold of 0.025. The best-fit slope of the comparison is well off of the ideal value of 1.0 for a perfect comparison. This issue will be noted and further discussed throughout the results and discussion section. The fit R^2 parameter is good, however, at 0.82, suggesting linearity between the model and experiment.

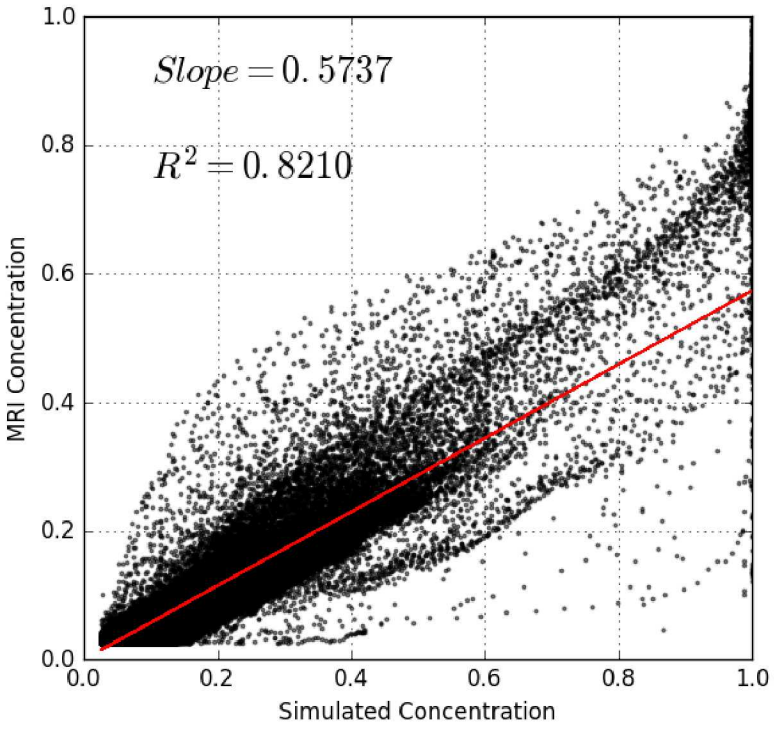

Figure 2-7. Concentration Comparison Based on Data Interpolated to the Model Mesh

If the source/destination meshes are switched, fewer data exist for comparison due to the lower local resolution of the experiment in the active region of the plume release. A similar scatter plot of these results is found in Figure 2-8. The slope is nearly identical, with the R^2 also quite close in magnitude. Employing a few additional metrics of comparison, the quantitative results of the mesh comparison activity are found in Table 2-2. The LND and LLR metrics suggest greater differences, but still a good comparison between simulation and data magnitudes for the error terms. This is taken as evidence that the quality of the comparison is nearly equivalent regardless of whether the interpolation is performed on the data onto the simulation mesh, or of the simulation results onto the data mesh.

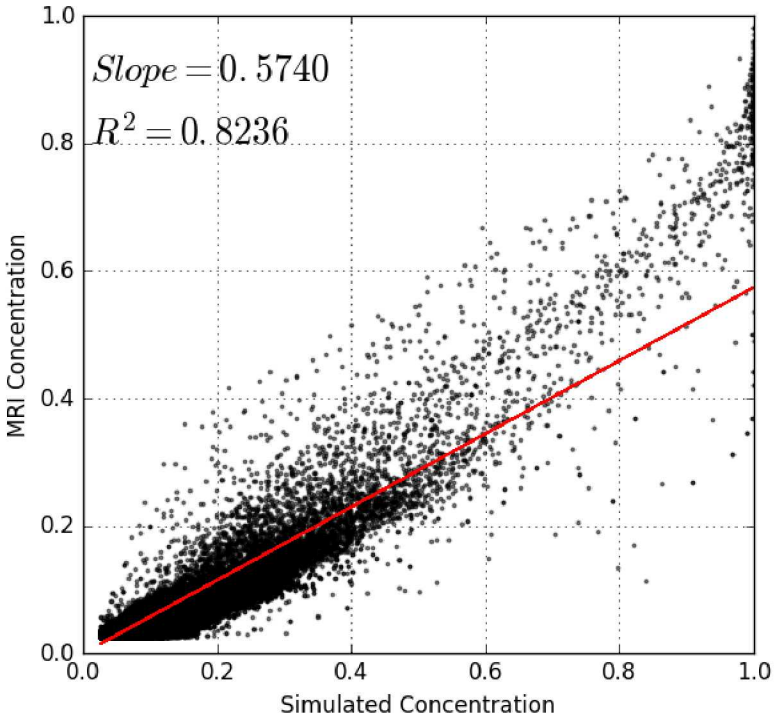

Figure 2-8. Concentration Comparison Based on Simulation Results Interpolated to the Data Mesh

Table 2-2. Quantitative Results from Interpolation Evaluation

Parameter	Data-on-Simulation	Simulation-on-Data
Comparison Points	191,868	55,200
Slope	0.5737	0.5740
R^2	0.8210	0.8236
LND	0.4655	0.4349
LLR	0.6539	0.6064

2.4. Credibility Assessment

One aspect of this work is to assess the credibility of the simulation predictions. These efforts include the grid refinement study, parameter study, and validation comparisons between experimental data and simulation predictions. An initial assessment was made following the processes from the American Society of Mechanical Engineers Standard for Verification and Validation in Computational Fluid Dynamics and Heat Transfer (ASME V&V 20-2009) that have been developed for this purpose. It is commonly used and accepted by many simulation assessment practitioners.

Fluids dynamics with contaminant transport are the physics of interest in this work. Verification is the process of determining if the simulations are solving the governing equations properly that describe the physics. Model validation, or simply validation, is the process of determining if the simulations and subsequent models are solving the correct equations (ASME, 2009).

A useful process to assess credibility is to calculate the validation comparison error:

$$E = S - D$$

where S are a simulation output(s) and D are experimental data. This error has both a sign and a magnitude. The validation uncertainty (U_{val}) is defined as:

$$U_{val} = \sqrt{U_{num}^2 + U_{input}^2 + U_D^2}$$

Where U_{num} is the numerical uncertainty commonly assessed by grid convergence studies, U_{input} is the input parameter uncertainty, and U_D is the experimental data uncertainty on simulation inputs propagated through the simulation (ASME, 2009). Note the intentional use of U to represent the expanded uncertainty as in $U = Cu$ where C is a confidence coefficient and u is the standard uncertainty as found in the standard. This work uses the expanded uncertainty at the common 95% confidence level with $C \cong 2$. Both the error and uncertainty are quantitative measures that can be used for credibility assessment in cases where experimental data are available and verification studies have been performed. This work has been setup to provide the required information for this assessment, but as will be shown, there are challenges to advance this work in this regard.

2.5. Grid Convergence Study

The grid convergence study used procedures in the V&V 20 standard (ASME, 2009) that have been commonly accepted. The results of this study are represented herein by U_{num} and are understood to be the contribution of the mesh resolution on the simulation uncertainty. The best practice is to run the simulation on three meshes with systematic refinement everywhere and in all directions so that the cell/element shapes are similar. Refining by a factor of two is preferred but is typically prohibitively expensive in three dimensions. Nevertheless, the refinement ratios should remain greater than 1.3.

The first step is to quantify the characteristic mesh length scale h for each of the three meshes. The refinement ratios are then $r_{21} = h_2/h_1$ and $r_{32} = h_3/h_2$ where $h_1 < h_2 < h_3$ so that h_1 is fine, h_2 is medium, and h_3 is coarse. The observed spatial order of convergence is:

$$p = \frac{1}{\ln(r_{21})}\left[\ln\left|\frac{\epsilon_{32}}{\epsilon_{21}}\right| + q(p)\right]$$

$$q(p) = \ln\left(\frac{r_{21}^p - s}{r_{32}^p - s}\right)$$

$$s = sign\left(\frac{\epsilon_{32}}{\epsilon_{21}}\right)$$

where the simulation result differences are $\epsilon_{32} = \phi_3 - \phi_2$ and $\epsilon_{21} = \phi_2 - \phi_1$. Note that $q(p) = 0$ for $r = const$ which is the best practice but was not followed exactly in this study. Fixed point iteration is

required with the initial guess equal to the first term ($q = 0$). In practice, it was found that the iterative scheme was unstable and the updating of p required sizeable levels of relaxation as in:

$$p = \frac{\omega}{\ln(r_{21})}\left[\ln\left|\frac{\epsilon_{32}}{\epsilon_{21}}\right| + q(p)\right] + (1-\omega)p$$

where ω is the relaxation factor. Relaxation of 0.1 provided for a stable scheme. These calculations were performed on every point in the line profiles. Iterations continued until the observed order of convergence residuals from one iteration to the next had a spatial mean less than 10^{-6}.

In this work, the baseline simulation used the medium mesh, so the uncertainty on this mesh was estimated. The next step is to calculate the extrapolated simulation predictions from the coarse (3) and medium (2) results as in:

$$\phi_{ext}^{32} = \frac{r_{32}^{p}\phi_2 - \phi_3}{r_{32}^{p} - 1}.$$

The absolute value of the error is used for subsequent uncertainty calculations as in:

$$e_a^{32} = |\phi_2 - \phi_3|.$$

Finally the Grid Convergence Index, considered equivalent to U_{num}, is:

$$U_{num} = GCI_{fine}^{32} = \frac{Fs * e_a^{32}}{r_{32}^{p} - 1}$$

where Fs is the factor of safety. This factor is 3.0 by default. But in cases where the observed order or convergence is within 10% of the formal order of the numerical scheme, a value of 1.25 has been shown to be conservative (Oberkampf and Roy, 2010). Another recommendation is that the observed order p be constrained to be between 0.5 and the formal order if not within 10% of the formal order to reduce the incongruous results that are observed moderately frequently.

2.6. Parameter Sensitivity

A parameter sensitivity analysis is intended to assess the impact of input uncertainties on model predictions. Through this, it is intended to provide insight on the numerical uncertainty related to modeling assumptions in relation to the LES turbulence model. Table 2-3 shows the main parameters of interest and the changes that were made with respect to the baseline simulation. The baseline time-step ensured that the CFL number did not exceed 0.5, while larger time step corresponding to a CFL limit of 0.95 was also considered. The inflow sub-grid scale turbulence intensity was increased by 10%. The laminar Schmidt number was varied according to values motivated by previous research (Shen et al., 2017). The inlet velocity profile was adjusted by +/- 5%. Experimental conditions with inherent uncertainty, temperature and contaminant injection rate, were also examined. Because the energy equation was not solved for this case, the temperature was modified by adjusting the density and viscosity based on literature information. This included about a 0.1% change in density, and 10% change in viscosity.

Table 2-3. Parameter Study Details

Variable	Type	Baseline	Variation
Turbulence Model	Numerical	KSGS LES	TFNS, k-ε
Turbulence Intensity	Experimental	0%	+10%
Schmidt Number	Experimental	0.9	0.7, 0.5
Inlet Velocity Profile	Experimental	Profile	Profile +/- 5%
Temperature	Experimental	21°C	±5°C
Contaminant Injection Velocity	Experimental	4.4 cm/s	±5%

Input parameter uncertainty was propagated by the methods of the V&V 20 standard as in

$$u_{input} = \sqrt{\sum_{i=1}^{n}\left(\frac{\partial S}{\partial X_i}u_{X_i}\right)^2}$$

Where X_i are the input parameters, u_{X_i} are the uncertainties in the input parameters, and n is the number of parameters (ASME, 2009), five in this case. The partial gradient $\frac{\partial S}{\partial X_i}$ was approximated using finite differences by calculating the change in the simulation output (concentration or velocity) divided by the change in input parameter. In cases where the parameter had double-sided variation symmetrically around the baseline, the partial gradient was approximated by using the outer values. For single-sided variation, the variation and baseline were used. The uncertainty values were often those by which the parameter was varied except for the inlet and injection velocity magnitude where the experimental uncertainty was 5.5%.

2.7. Experimental Data Uncertainty

The experimental data uncertainty was considered in the validation comparisons and in the parameter study. The experimental team quantified three uncertainty values with concentration uncertainty $U_{conc,exp} = 4\%$ of measured value, velocity uncertainty $U_{vel,exp} = 5.5\%$ of measured value, and spatial uncertainty $U_{space} = 0.4\ mm$. These uncertainties were taken at the common 95% confidence level. The spatial uncertainty was propagated to both the concentration and velocity predictions through the spatial gradients of these quantities as in $U_{conc,exp,total} = \sqrt{U_{conc,exp}^2 + \left(\frac{\partial Conc}{\partial space}U_{space}\right)^2}$ and $U_{vel,exp,total} = \sqrt{U_{vel,exp}^2 + \left(\frac{\partial Vel}{\partial space}U_{space}\right)^2}$. The local gradients were approximated by second order central differencing in the central region and second order forward or backward differencing for the endpoints (Chapra and Canale, 2010).

This page left blank

3. RESULTS

3.1. Planar and 3D Comparisons

Planar and 3D results are limited to the baseline scenario performed on the medium mesh. Three techniques are used for 2D and 3D comparisons. Specific planes are selected upon which the simulation results are compared against the data. Visualization software is also used to extract and illustrate temporal planar and volumetric output, with the primary objective being to illustrate the dynamics of the flow from the simulations. There are no corresponding data to these output figures. The third technique is a full comparison across the 3D domain field. This is accomplished by interpolating between the data and simulation meshes and using a variety of metrics to compare the similarities between the vector and scalar fields.

3.1.1. Planar Comparisons

The planar output was extracted for each simulation using a python script in kitware ParaView software (version 5.5) that was designed to precisely extract planes and use common scales among the figures. The data were extracted from a Tecplot software formatted file containing the results from the MRC/MRV data and provided by the test team. The Tecplot file was imported to ParaView to obtain consistent scaling of the experimental and simulation contours. Some adjustments were necessary to align the output data, as the scaling and coordinate system were not identical between the two data sources. Several bugs were found in ParaView that challenged the ability to extract quality figures. One related to the font sizes of the output scale labels. These have been retained in the planar plots because they are key to understanding scale, even though they are clearly too small to be reasonably read. A scale reference line has been independently provided in the figures to help with the scale problem. Domain size between the test data and model were different. Planar figures were manually arranged for the composition figures using the boarder ticks as guides to provide uniformity to the alignment.

Figure 3-1 shows the experimental and simulation results at the E-F plane. The tall building is easily identifiable in the figure, as the corner of the building touches the E-F plane and the contours for concentration (mass fraction) as well as velocity exhibit an abrupt transition along the edge up to the full height of the building. The smaller down-stream buildings also exhibit such stark transitions in the concentration contours as the contours remain sufficiently high, and in the velocity contours. The contour data and simulations are similar, with the most significant differences being the larger size of the high concentration (red) region in the model near the building and the size of the green/light-blue region in the wake of the largest building. The velocity simulation results also compare well to the data, with the most noteworthy differences in the region below the tops of the small buildings, especially just down-wind of the tallest structure. The irregularity in the velocity field downwind of 15 cm are an artifact of the model methods. A light porous buffer layer was used just inside of the open boundary in the model to help maintain stability and reduce the potential for the negative effects of transient eddy interacting with the open boundary condition. Both data plots show up-wind gaps in the data near the ground surface. These are real, and part of the roughness layer used to help generate a wind profile to mimic that of a surface atmospheric boundary layer.

Figure 3-2 shows the planar results at the E plane. Concentrations are generally a little lower in the data than in the model in the wake of the tallest structure. The velocity profile in the wake of the tallest structure also differs in the near-field.

Figure 3-3 shows results at the 3 plane, which appear to be reasonably similar. The most notable differences are that the model predicts more concentration at the top of the tall building than in the experiment. Also, there appears to be a steeper gradient in the velocity just above the short buildings in the model than in the experiment. This is manifested in the larger yellow color band in the data compared to the model.

Figure 3-4 shows results from the 3-4 plane. These results show significant similarity between the measurements and experiments. The general shape of the high concentration is nearly identical. The model has sharper edges to the data, and there are slightly higher concentrations near the centerline rising above the surface. The velocity fields also have remarkable similarity. The tests were more symmetric than the simulations, with the most notable divergence near the ground at centerplane.

Figure 3-5 has similar symmetry differences in the velocity field at the 4 plane. Otherwise, the results are similar. The experimental data and model are remarkably similar, with the concentrations being a little lower in the data.

Figure 3-6 concentration data and model compare very well in shape and magnitude. This figure shows the lowest cut-plan results. The velocities are quite good as well, with the wake of the tall building being more symmetric in the data than in the model.

Moderate differences between concentration data and model are found in Figure 3-7. The simulation field is longer, and greater in magnitude. The velocity fields also show more differences than typically found. There is much greater red color in the model results near the tall building and immediately upwind of it indicating a higher concentration. These differences appear extensive, spanning the transverse length of the domain. There is also more asymmetry in the wake of the tall building in the model than in the experiments.

Figure 3-8 continues to show magnitude differences in the concentration field in the wake of the tall building. The velocity portion of the plot is much more similar between experiment and simulation, with the extended red region found at 3/6H diminished. The primary difference is the asymmetry in the wake of the tall building, and this is diminished also compared with the 3/6H and 1/6H planar data.

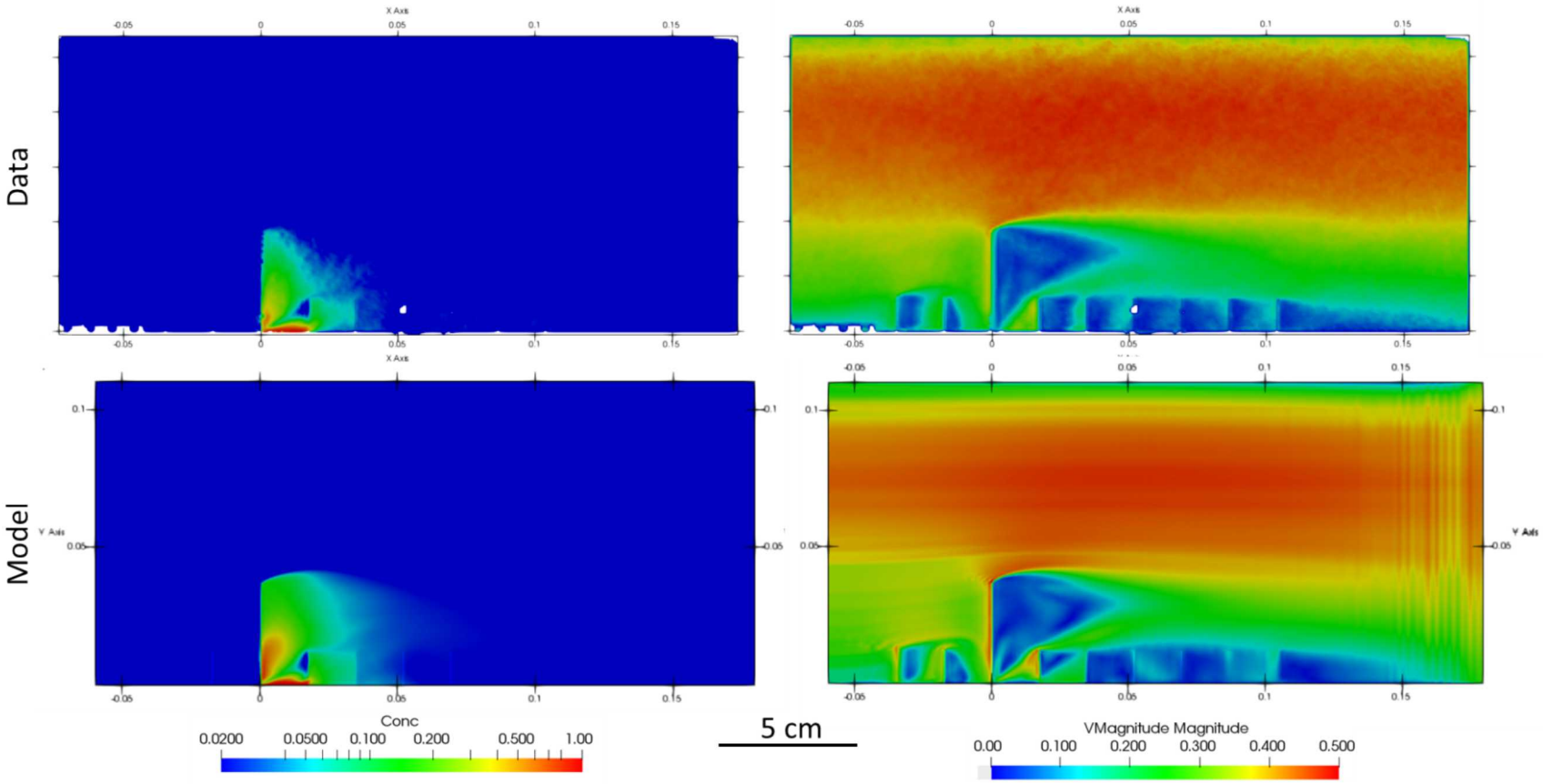

Figure 3-1. Concentration and Velocity Magnitude Data and Predictions for the E-F Plane

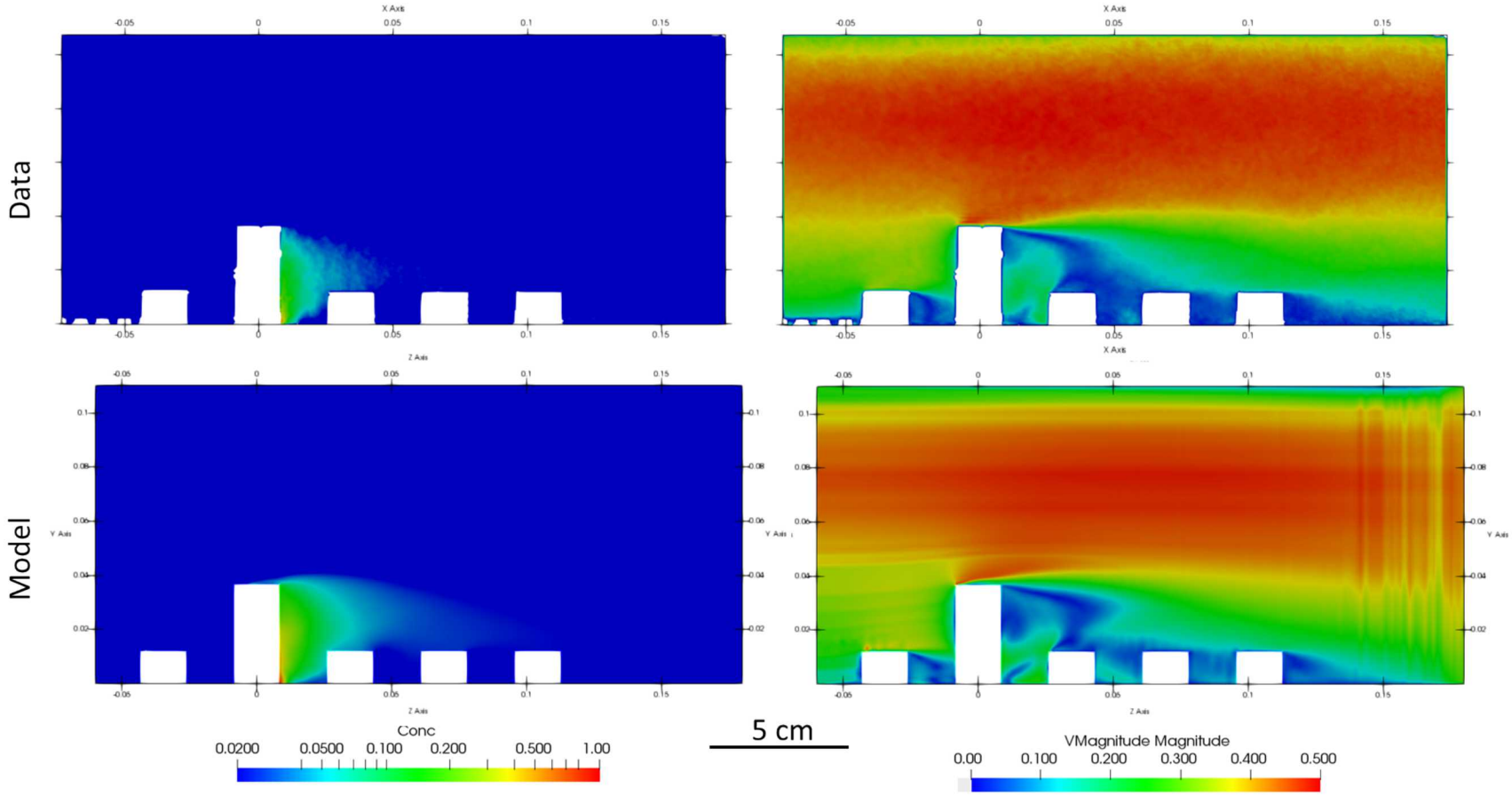

Figure 3-2. Concentration and Velocity Magnitude Data and Predictions for the E Plane (Centerplane)

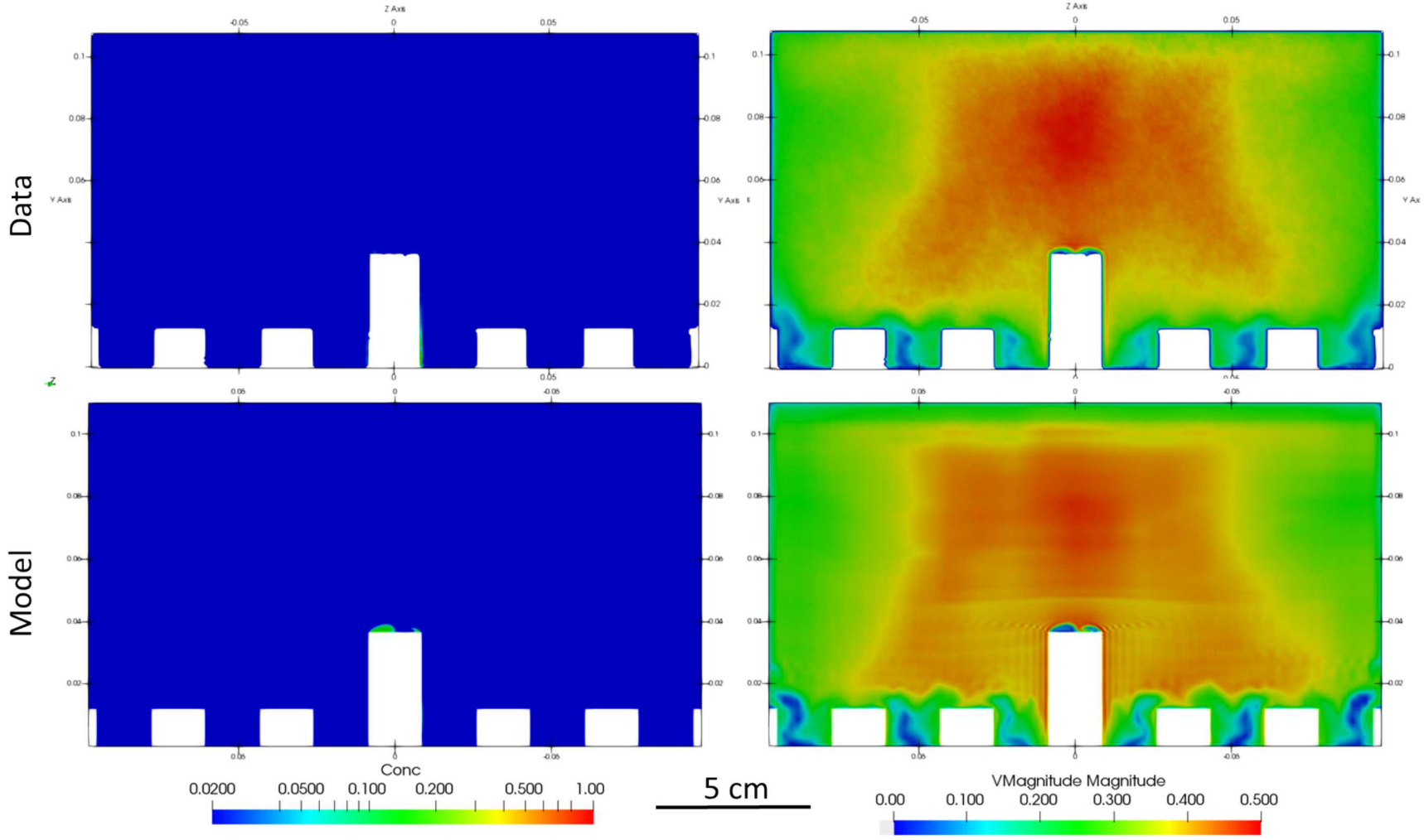

Figure 3-3. Concentration and Velocity Magnitude Data and Predictions for the 3 Plane

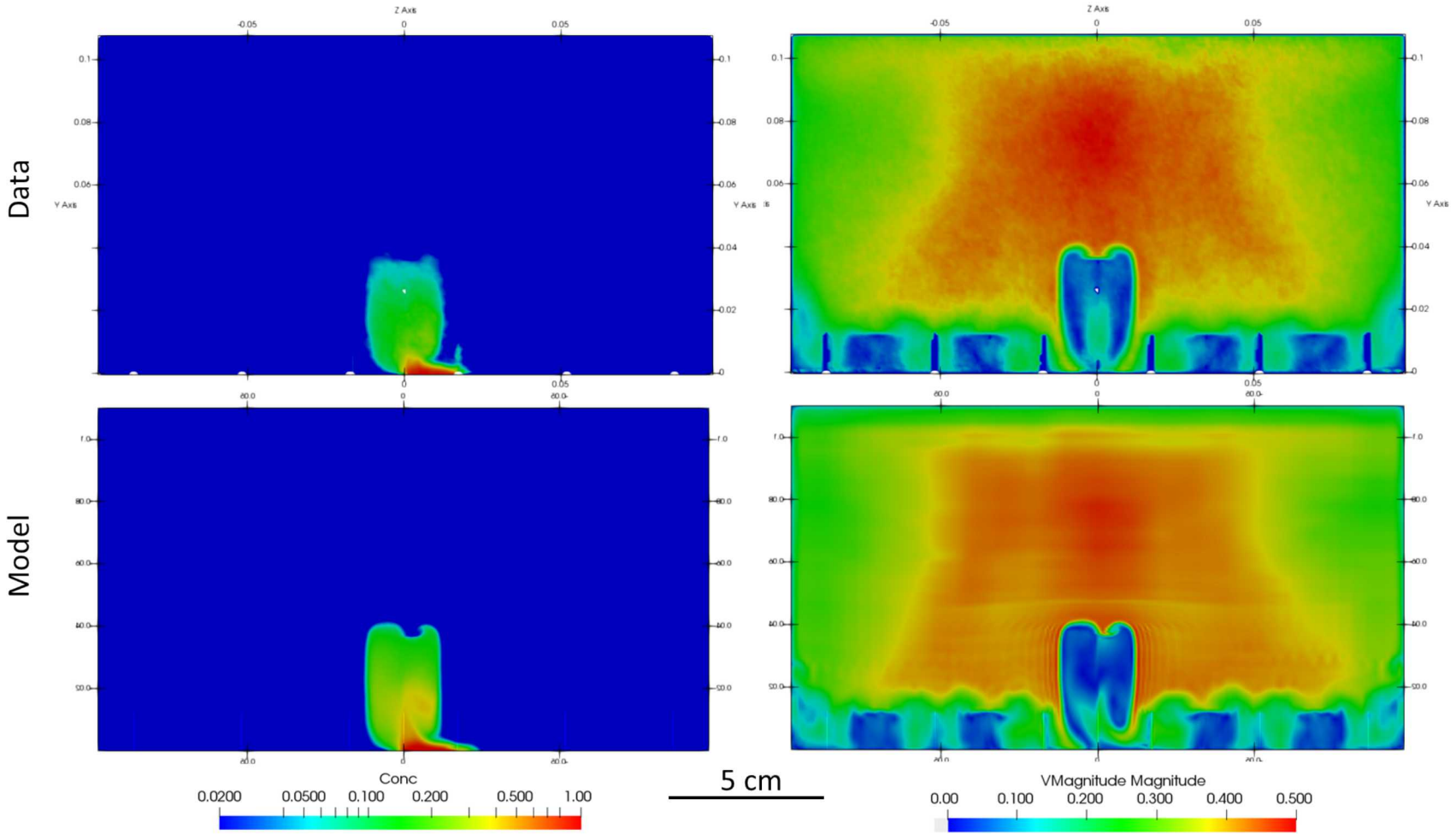

Figure 3-4. Concentration and Velocity Magnitude Data and Predictions for the 3-4 Plane

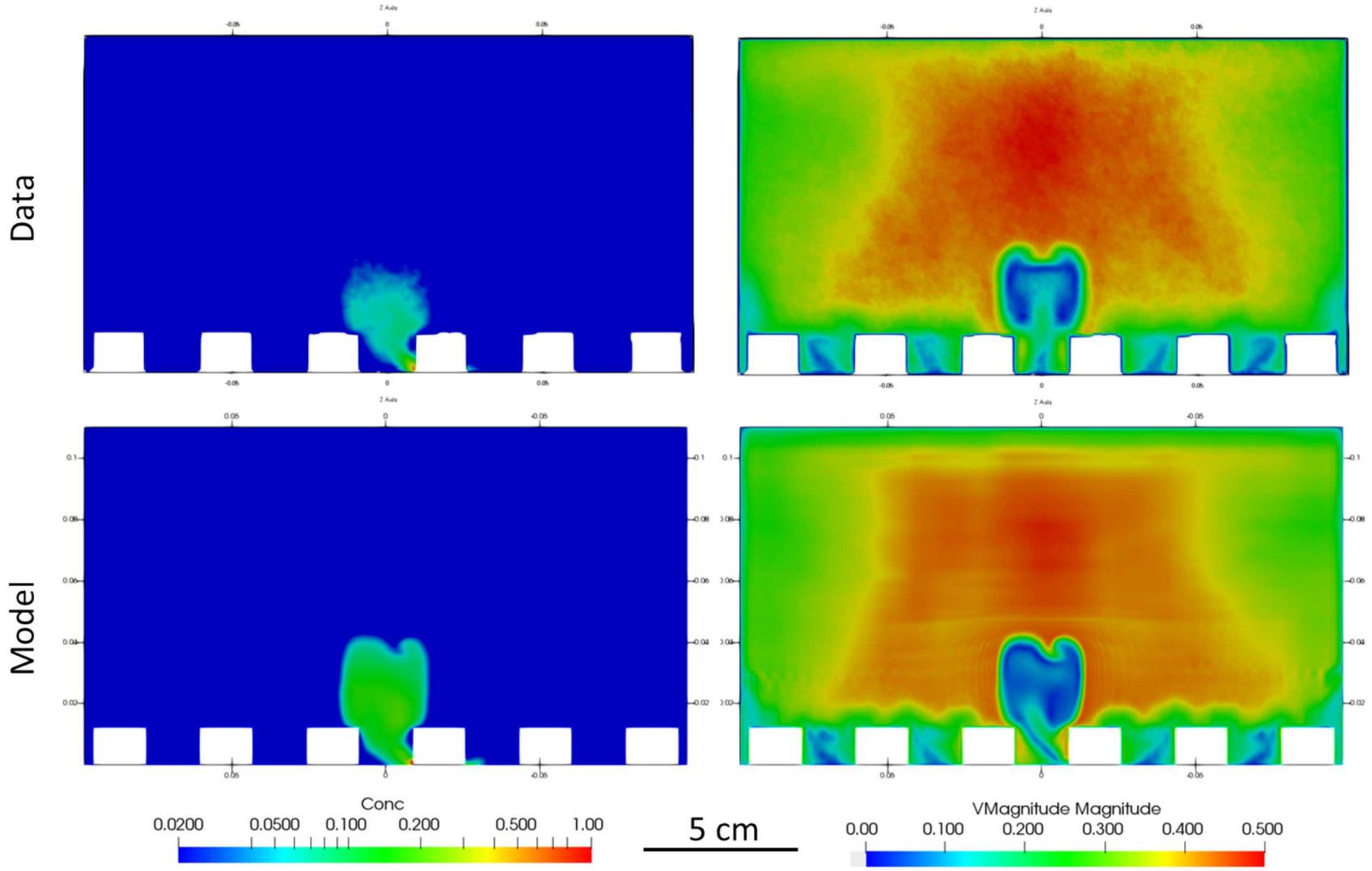

Figure 3-5. Concentration and Velocity Magnitude Data and Predictions for the 4 Plane

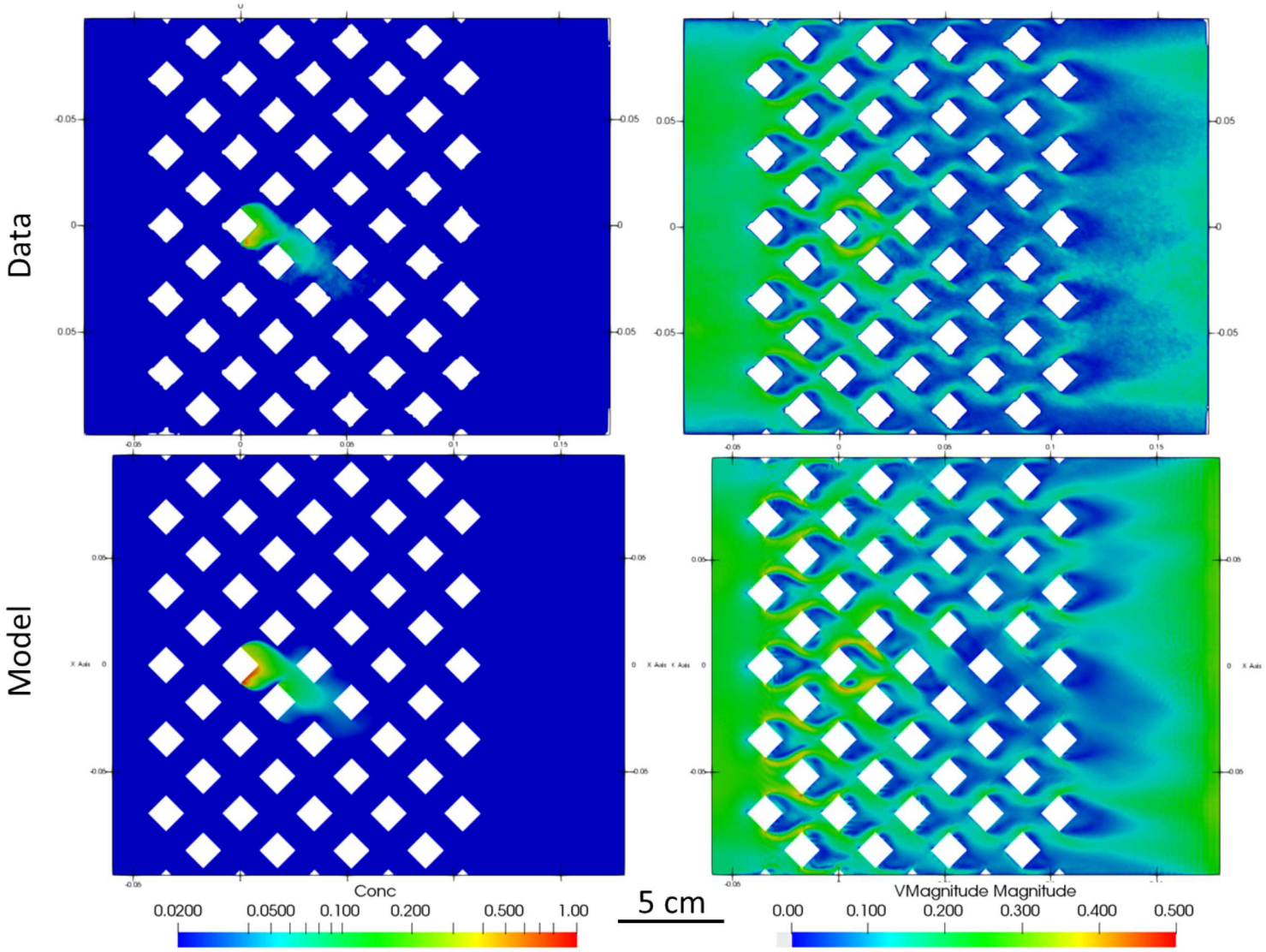

Figure 3-6. Concentration and Velocity Magnitude Data and Predictions for the 1/6 Plane

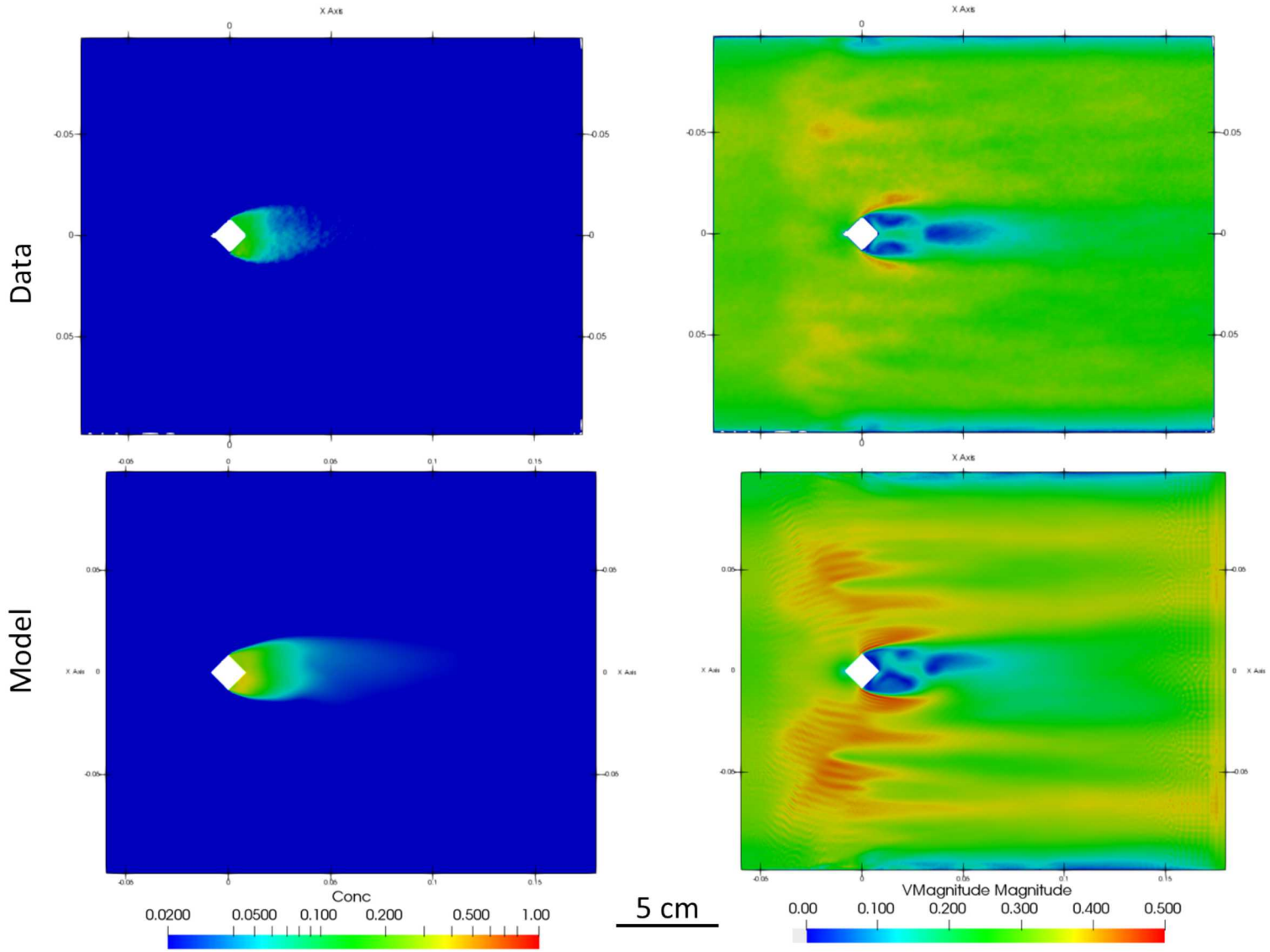

Figure 3-7. Concentration and Velocity Magnitude Data and Predictions for the 3/6 Plane

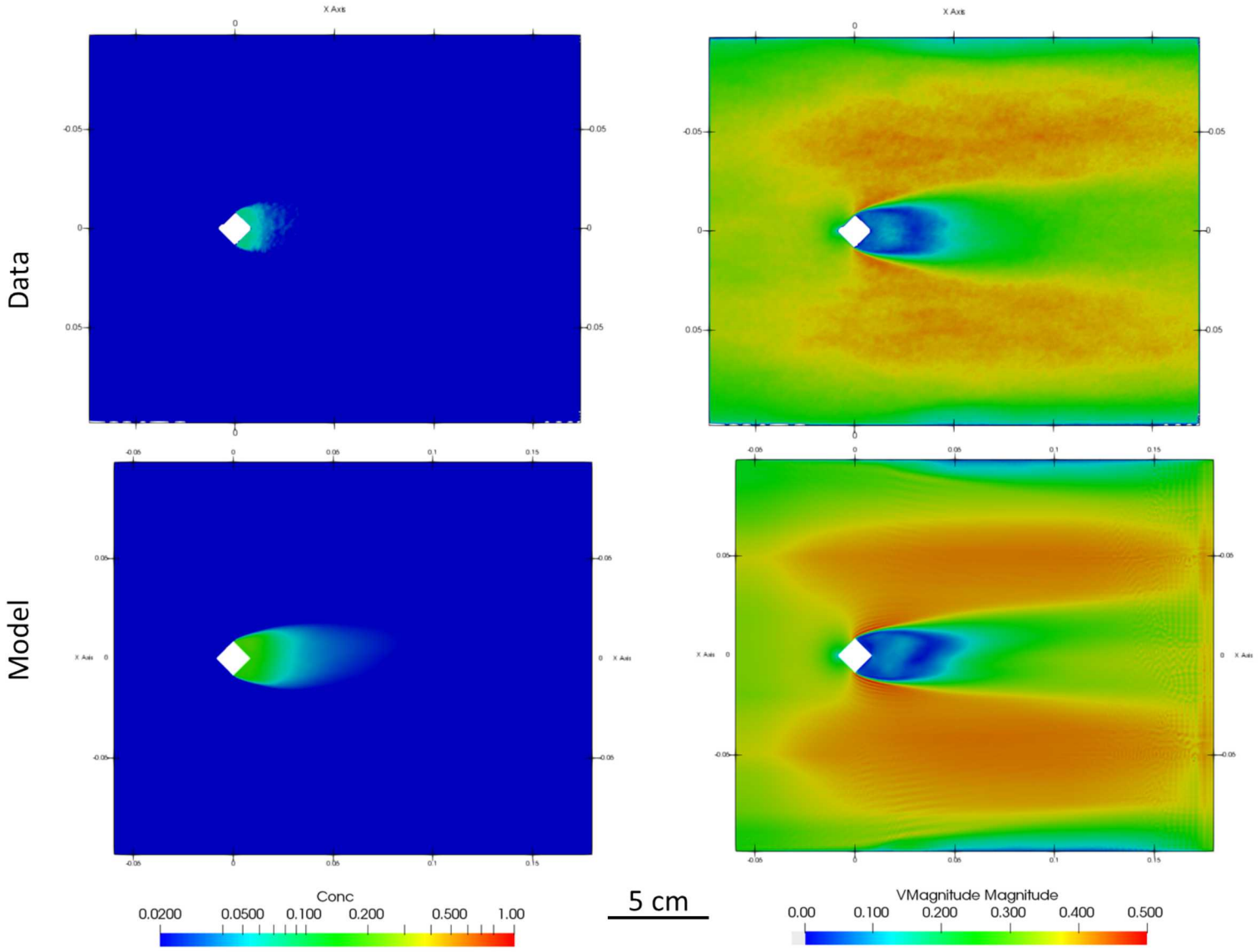

Figure 3-8. Concentration and Velocity Magnitude Data and Predictions for the 5/6 H Plane

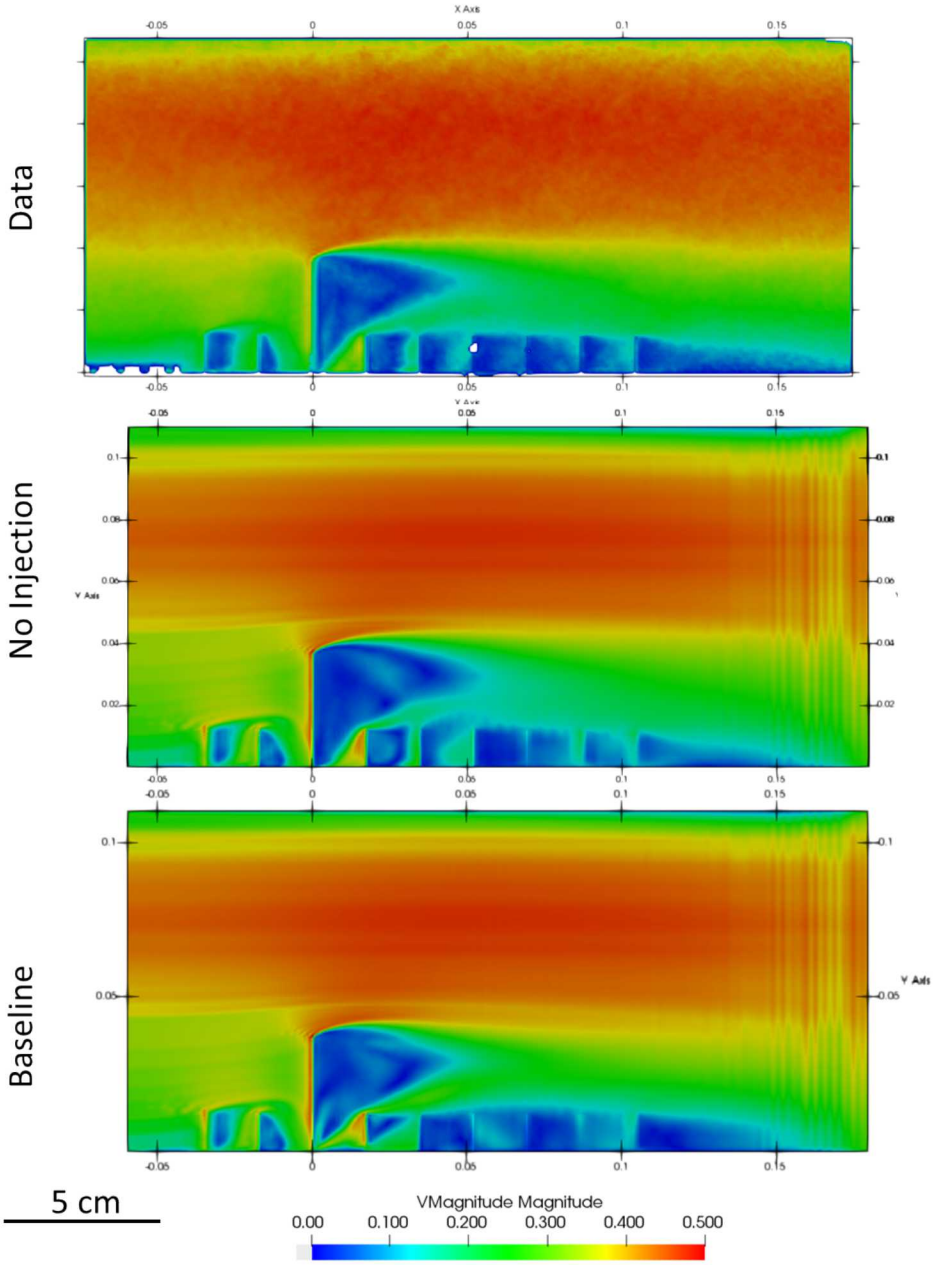

Figure 3-9. Velocity Magnitude Data and Predictions for the EF Plane

The velocity magnitude for the tests came from an experiment without an active contaminant inflow. It is possible with the simulation tool to replicate that condition. Velocity magnitudes compare better with the experimental results when the inflow conditions more closely match the conditions of the dataset. Figure 3-9 and the next few plots show selected results of a scenario where the injector is replaced with a wall in the simulation (No Injection case). In Figure 3-9, the data compare slightly better to the No Injection simulation case, with the most significant differences between the tall building and the next building downwind. Note, not all the plots for each scenario are shown in the body of the report, additional plots can be found in Appendix B Additional Plots.

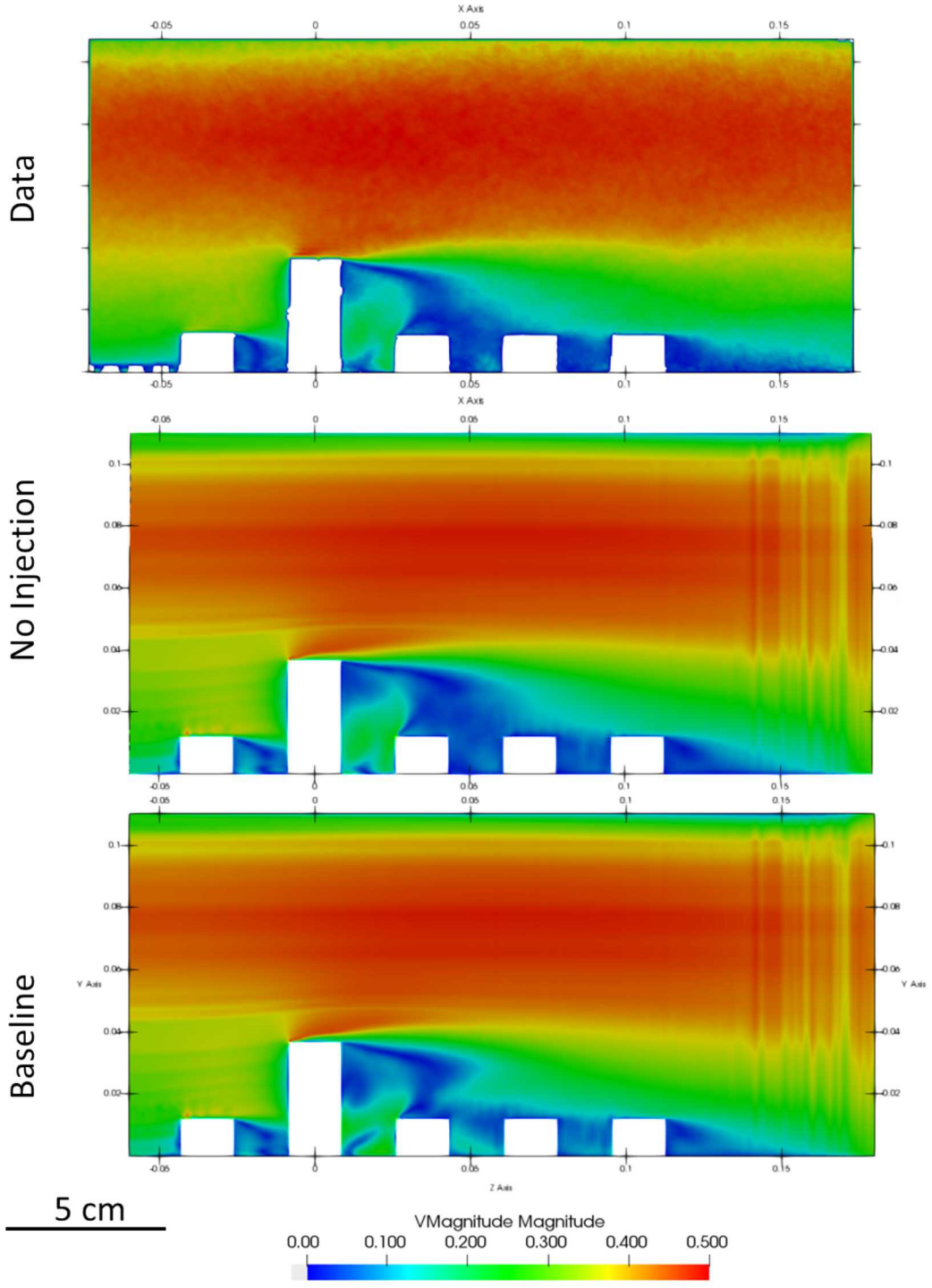

Figure 3-10. Velocity Magnitude Data and Predictions for the E Plane

Figure 3-10 shows more pronounced similarities between the data and the No Injection case, particularly in the wake of the tall building. Both the magnitude and the shape of the contours are much more similar to the data in the No Injection model.

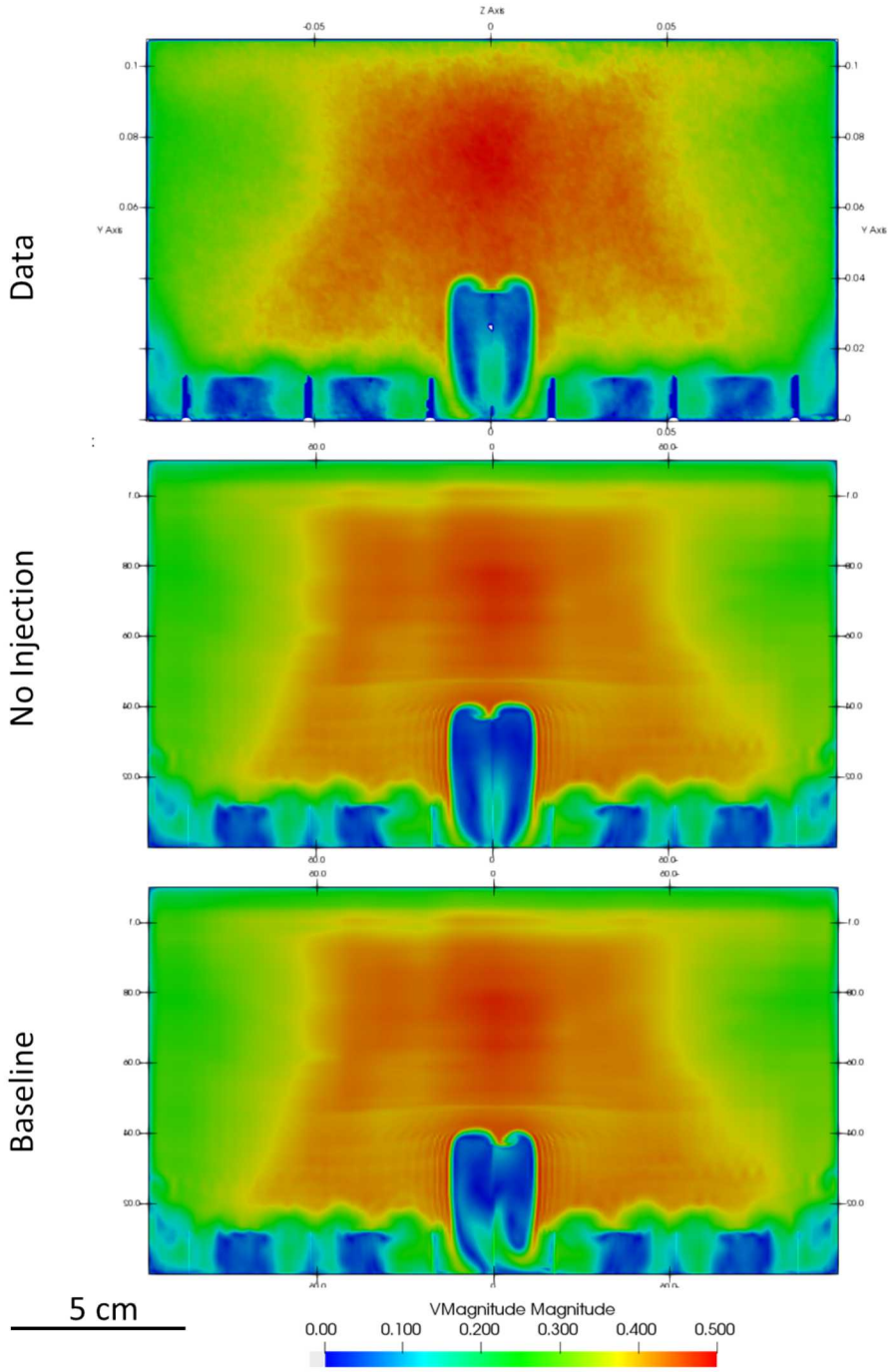

Figure 3-11. Velocity Magnitude Data and Predictions for the 3-4 Plane

Figure 3-11 shows that the No Injection case at the 3-4 plane is also improved compared to the data versus the Baseline case. The asymmetries near the centerplane are reduced. Figure 3-12 likewise shows that the No Injection velocities are more similar to the data, even at the 5/6 height. Asymmetry is reduced in the No Injection case.

The overall improved comparison for the No Injection scenario velocity magnitudes compared to the data versus the Baseline case suggests the assumption that the velocity from the plugged injector case being similar to that of the injected scenario might not be adequate. Testing was done in campaigns, and this test campaign did not include a velocity measurement with the injection flow on. More analysis of this will be made in the Discussion section.

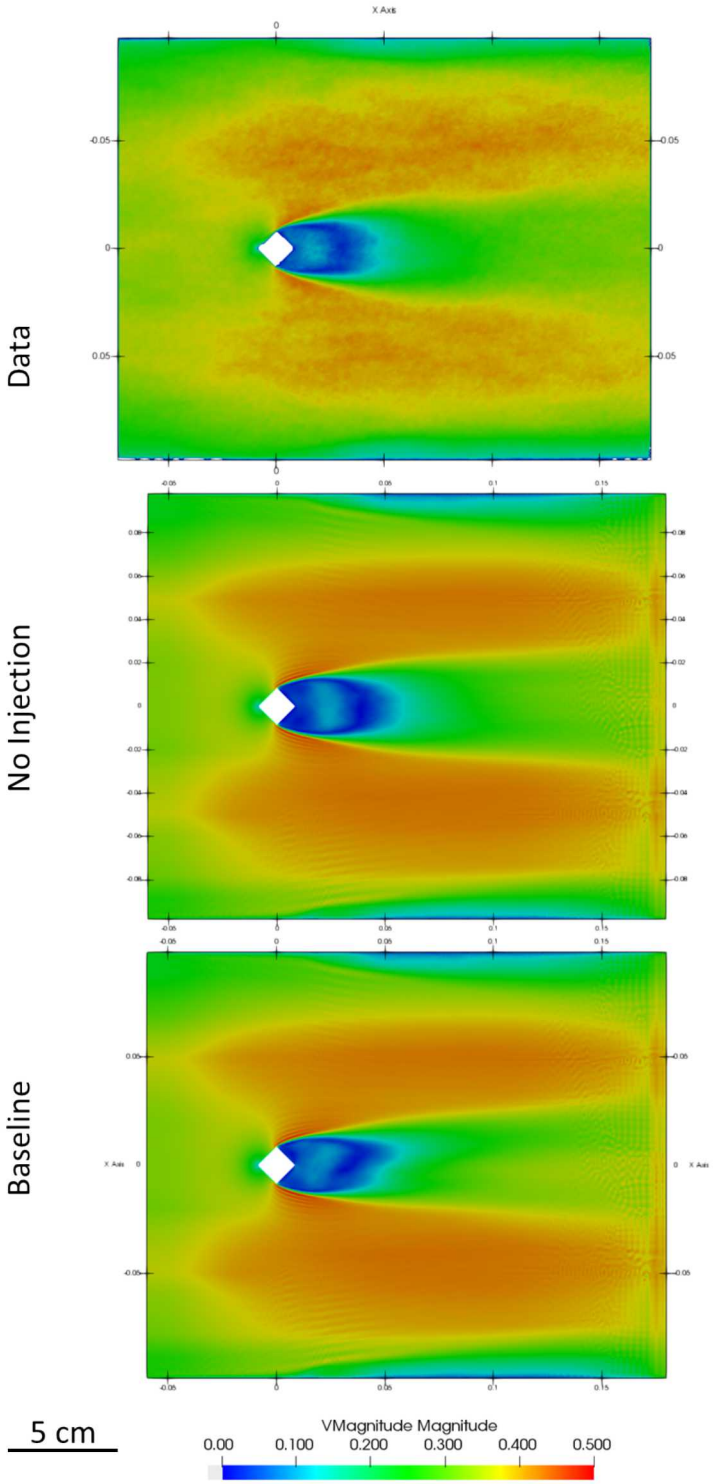

Figure 3-12. Velocity Magnitude Data and Predictions for the 5/6H Plane

3.1.2. Simulation Dynamic Output

The simulation results yield dynamic information that is not present in the time-averaged test results. These are not considered candidate validation simulation results because there are no corresponding test results. However, the simulation results can provide insight into the flow behavior, both predicted and experimental during instantaneous events. The vorticity and q-criterion are both calculated field parameters that can be helpful to identify flow features and to illustrate 3-dimensional behavior. These are best illustrated in video output from the post-processing tools. Selected frames from video output are compiled here to provide additional insight related to the tests that can be gained from the simulation output.

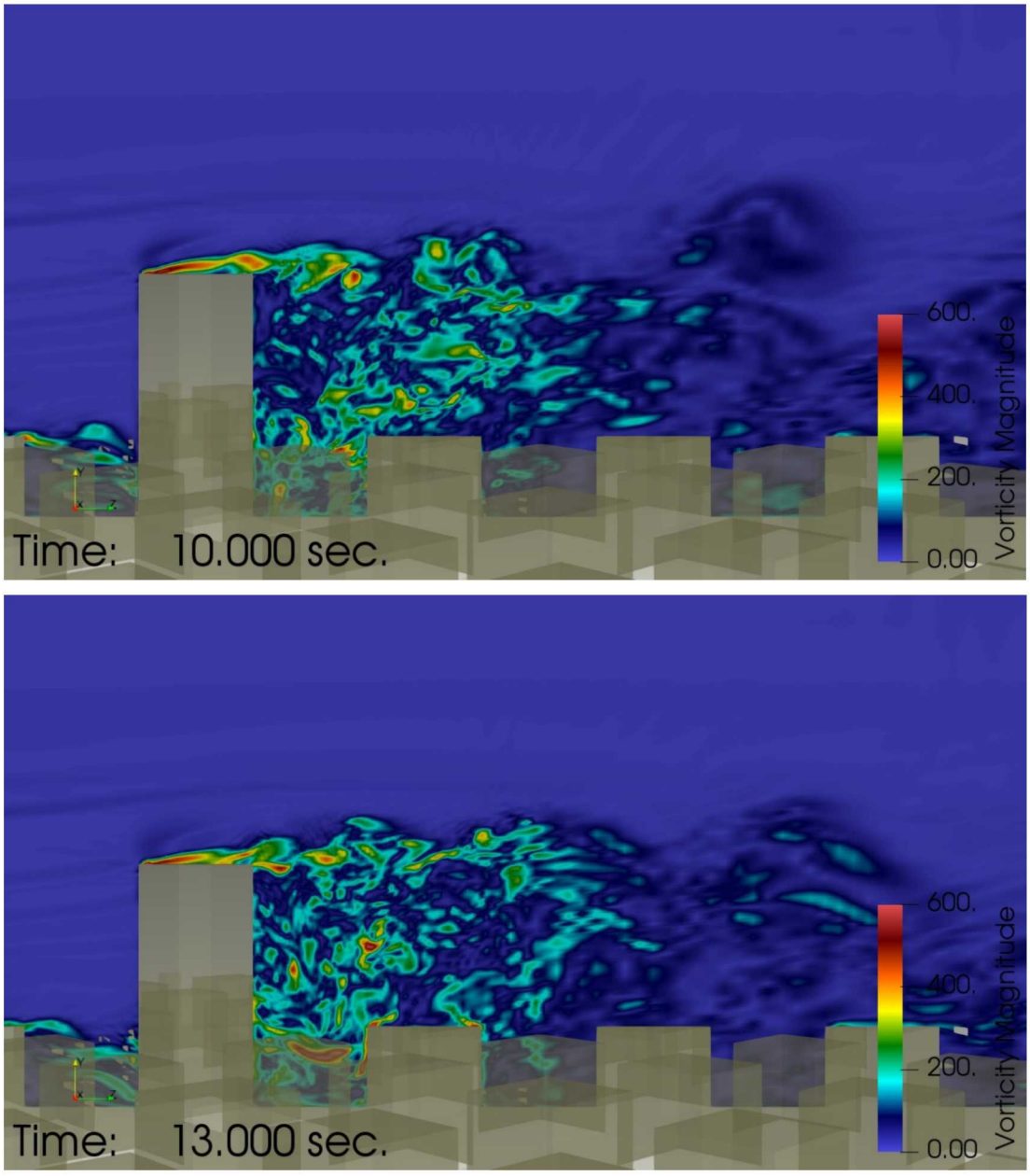

Figure 3-13. Vorticity Magnitude at the E Plane at Two Times

Figure 3-13 shows vorticity plotted at the centerplane. The streaks upstream of the tall structure are due to the inlet profile prescription method, a piece-wise vertical interpolation. The most significant note from these is that the wake region of the buildings produces significant vorticity and is very dynamic. It is also interesting to note the streaks from the inflow that correspond to interpolation lines.

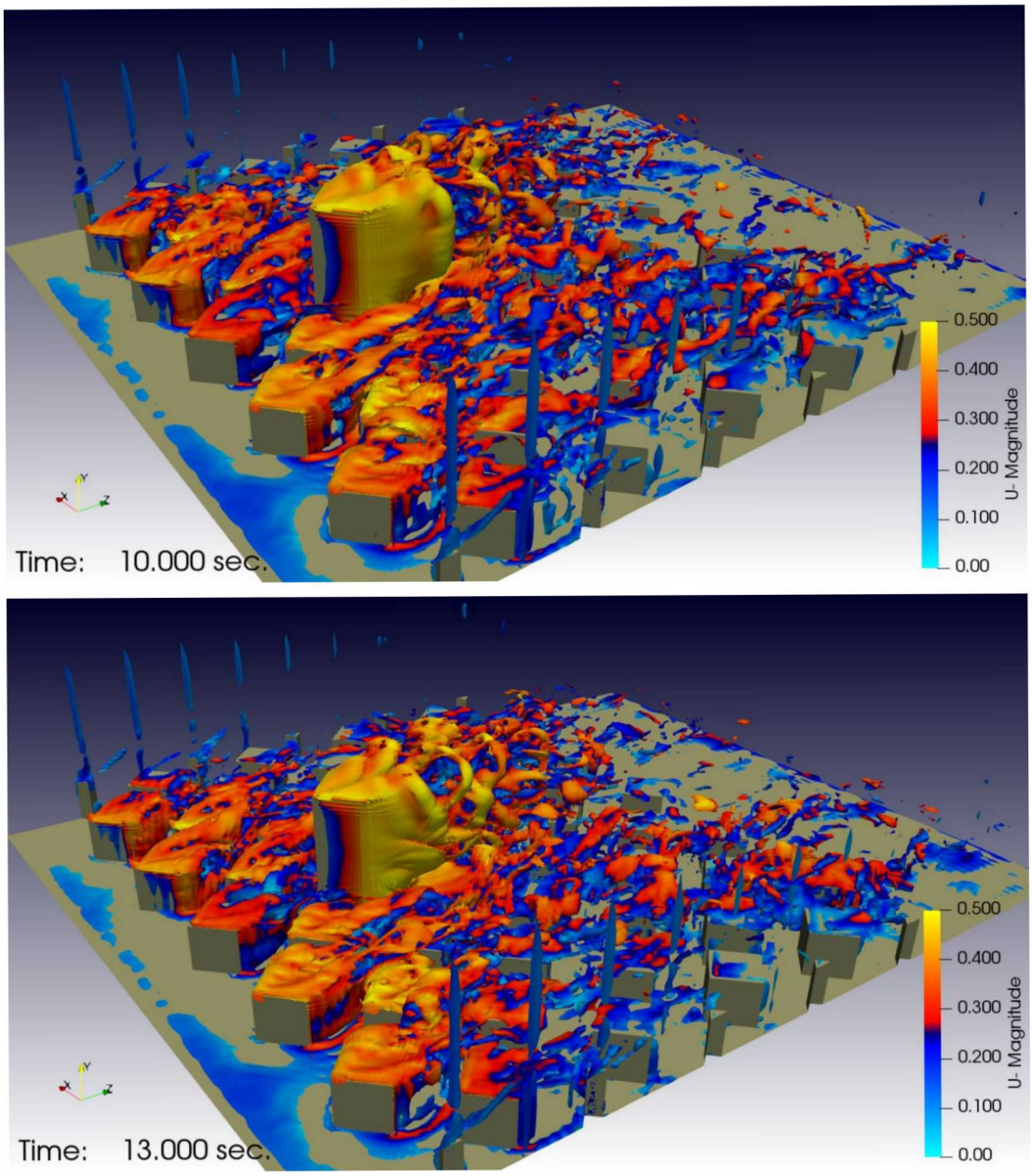

Figure 3-14. Vorticity Magnitude Isocontours at 150 1/s Colored by Velocity Magnitude at Two Times

Figure 3-14 shows vorticity magnitude iso-contours, which are helpful for understanding where the most significant turbulent mixing may occur. Different from the 90 degree scenarios, there is no ground horseshoe vortex in front of the cubic structures. Note the vertical lines of vorticity along the side walls. These are artifacts of the mesh that has local distortion. This demonstrates a sensitivity of mesh quality on vorticity, as the predictions should be more continuous through that region.

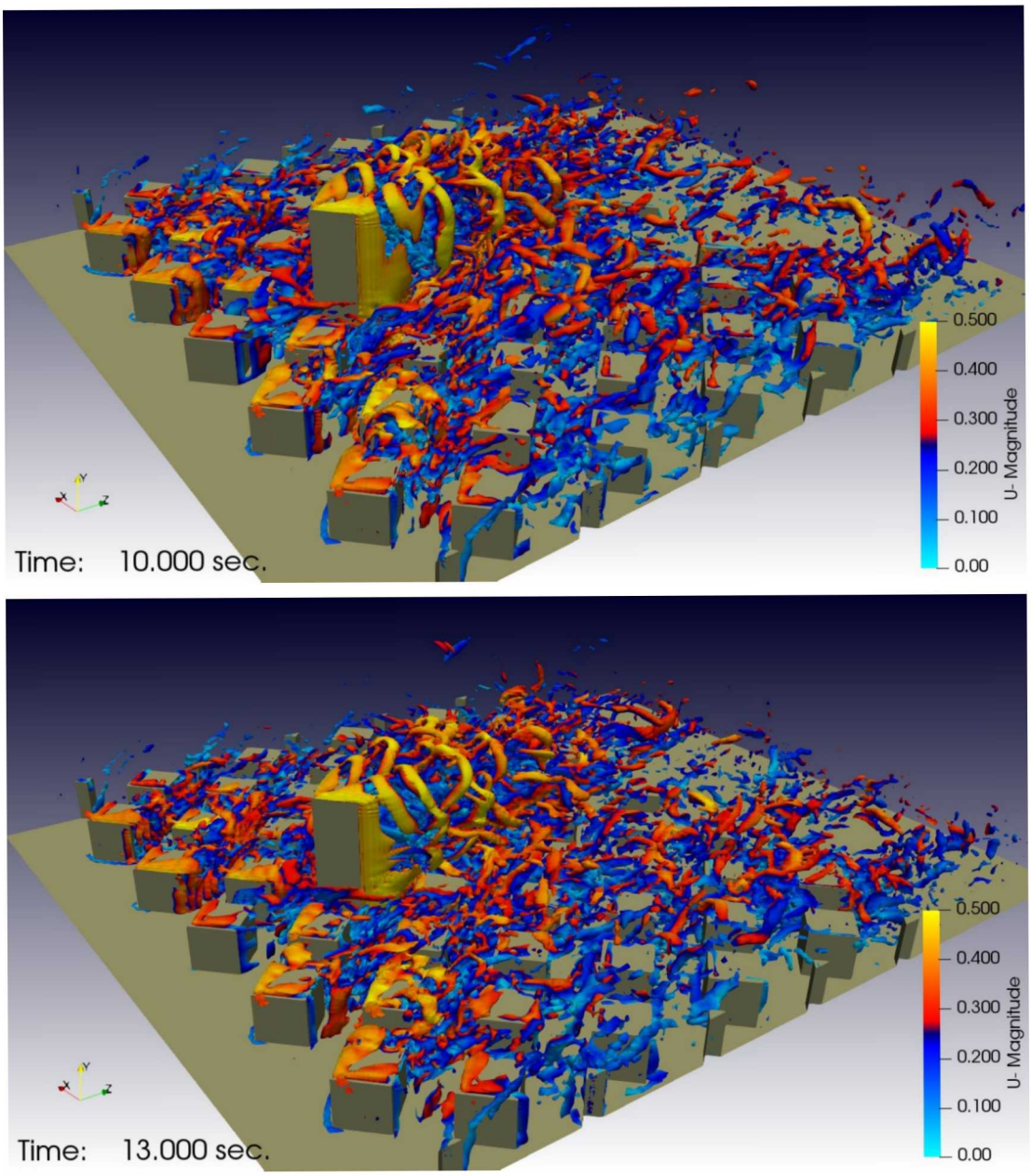

Figure 3-15. Q-Criterion Isocontours at 2000 1/s^2 Colored by Velocity Magnitude at Two Times

Figure 3-15 shows q-criterion magnitude iso-contours, which are also helpful for understanding where the most significant turbulent mixing may occur. Q-criterion is a better way to illustrate vortical structures than the mathematical vorticity values because vorticity cannot differentiate vortical motion from shear. The Q-criterion is missing the vertical volumes along the side walls, suggesting these are shear related anomalies.

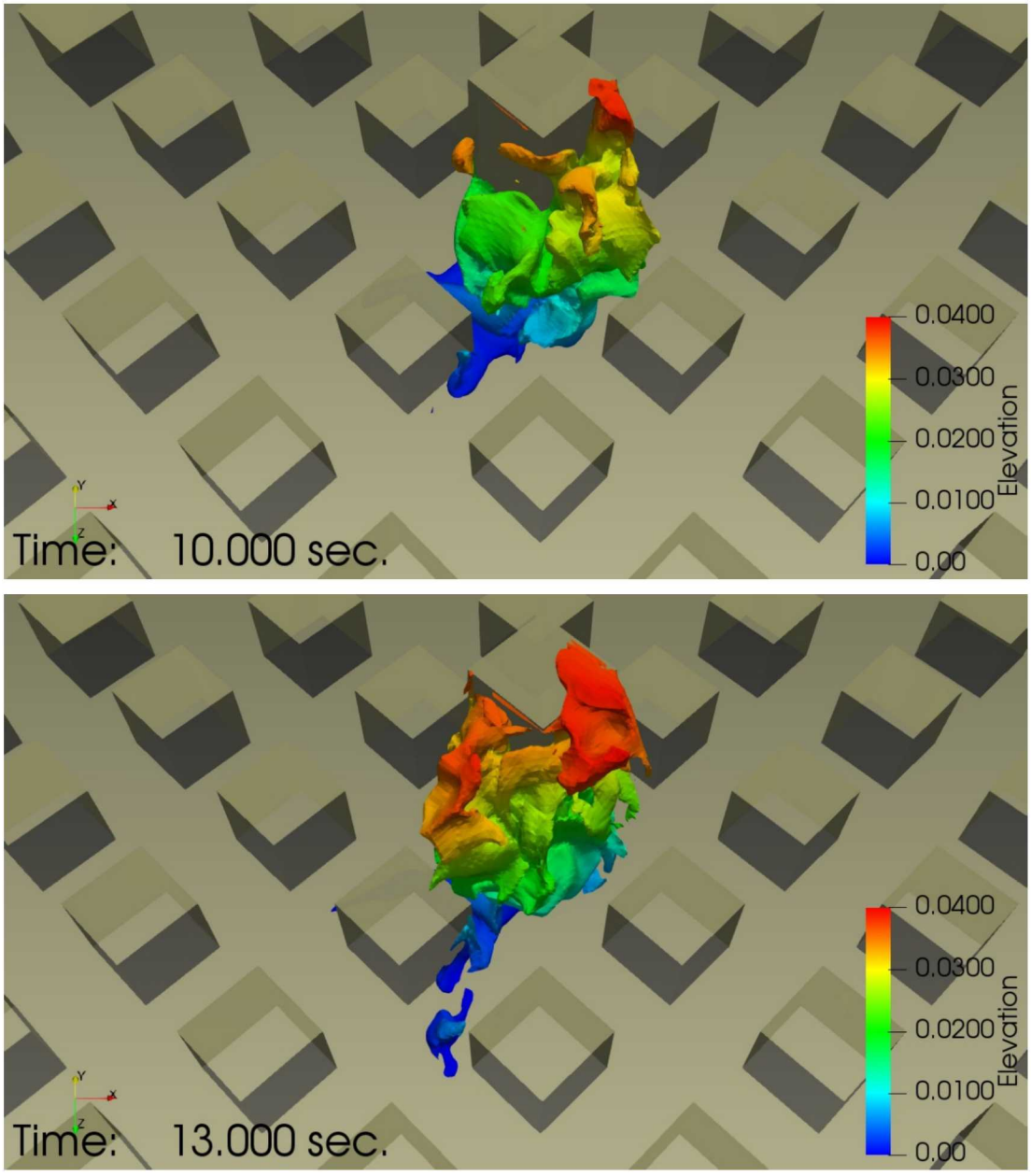

Figure 3-16. Concentration Isocontours at 0.2 Mass Fraction

Figure 3-16 shows iso-contours of species concentration at 0.2 mass fraction colored by elevation contours. The instantaneous mass fraction values varied significantly, and was smoothed substantially by time-averaging. The contours climb the tall building and are fairly symmetric despite the release being to one side of the centerline. The contours extend closer to ground level near the release downwind of the release, the other main differentiating factor in the results plots.

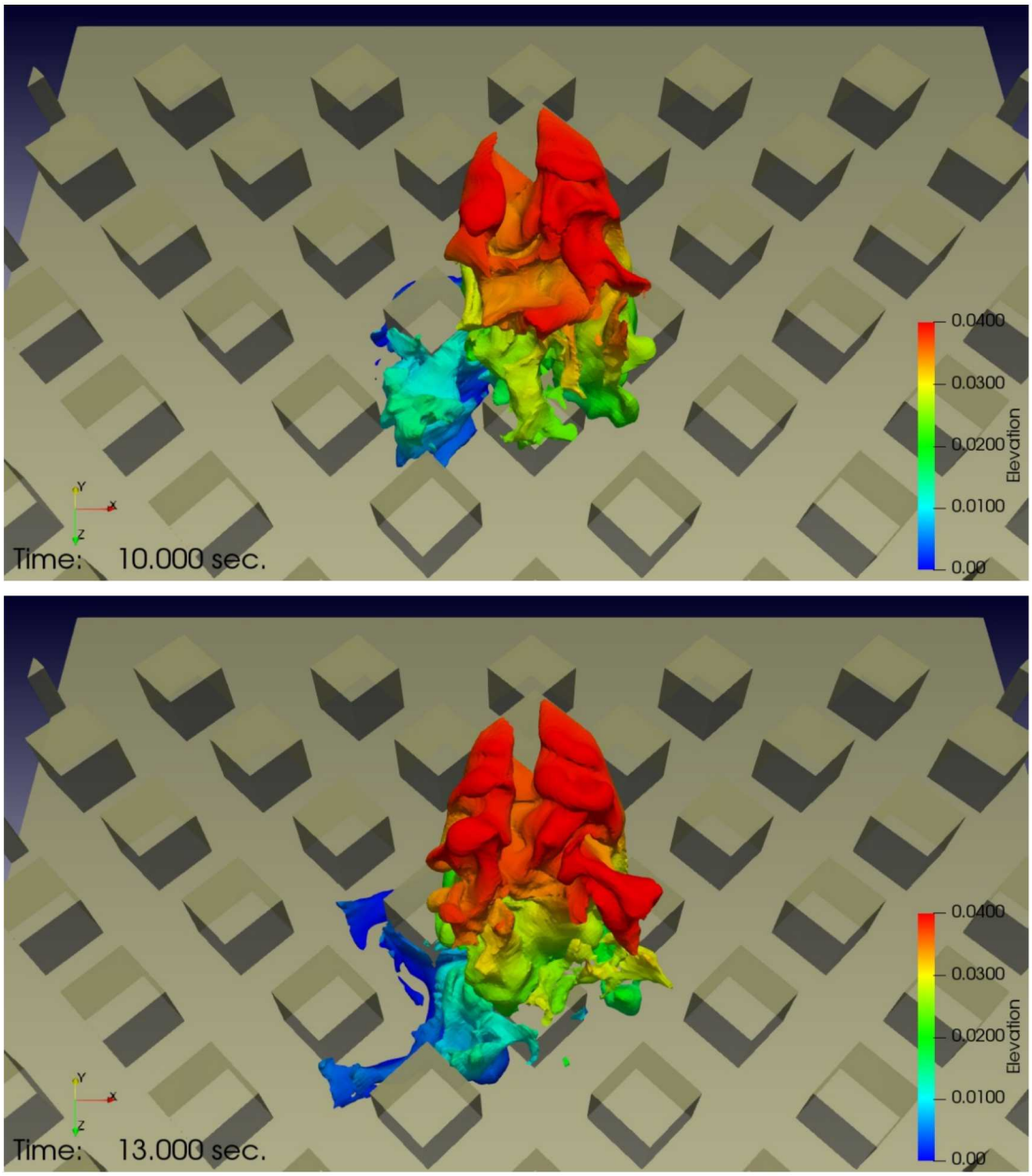

Figure 3-17. Concentration Icontours at 0.05 Mass Fraction

Figure 3-17 shows iso-contours for a smaller mass fraction of 0.05 similarly plotted with color contours of elevation. Similar to Figure 3-16, there is general symmetry at higher elevations. But in contrast, there is significant ground level dispersion to the side of the structure where the release originates at lower elevations.

3.1.3. 3D Comparisons

The data and simulation are compared using the data interpolated onto the simulation results. The methods section suggests a reasonable similarity in the results regardless of the source/destination mesh sequence used. A clip of the experimental concentration of 0.025 is used to omit from the comparisons any concentration data below the experimental detection threshold. This left an

irregularly shaped domain as illustrated in Figure 3-18 over which prediction and experimental results are compared. The inflow plane is evident in the red colored surface, and the location of some of the building structures can be seen where rectangular or flat surfaces exist in the iso-contour plot.

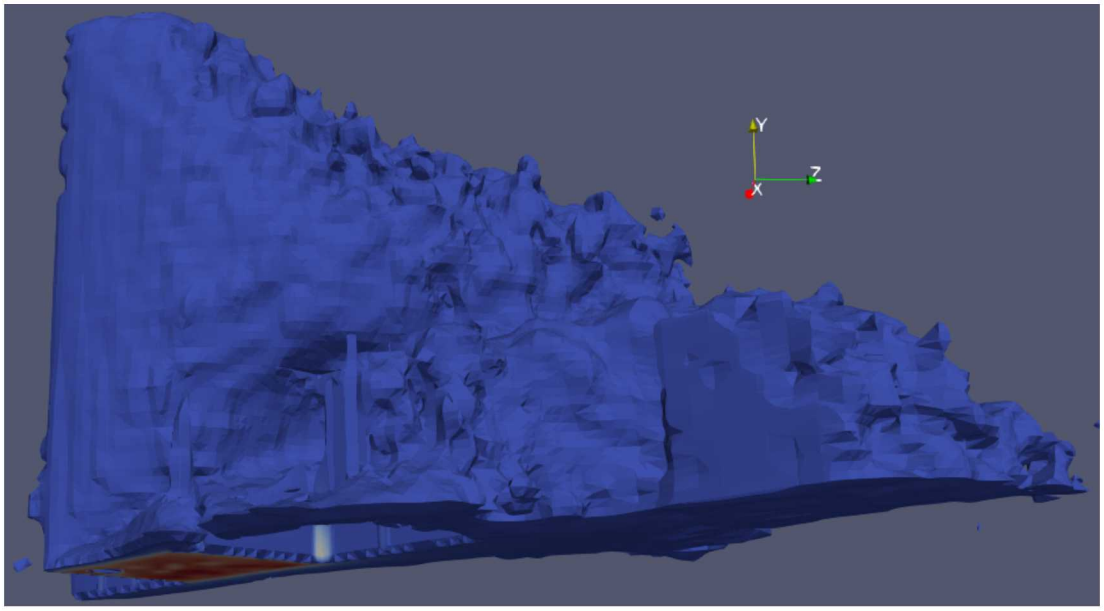

Figure 3-18. An Isocontour of Experimental Concentration at 0.025 Mass Fraction Colored by Concentration Magnitude

The baseline scenario comparisons using the experimental results interpolated onto the model mesh are found in Figure 3-19through Figure 3-21.

Figure 3-19 shows the concentration results. This differs slightly from the plot in the methods section because the points are colored by the distance from the release point (0,0,0) to aid in interpreting the location for each data point. Slight differences are also seen in the magnitude of the measures of comparison based on slightly different sampling of the data (197,062 data/simulation pairs). The R^2 suggests good linearity between the data and simulation, however, the slope suggests the simulation significantly over-predicts the experimental concentrations by almost a factor of 2.

Similar velocity magnitude comparisons are found in Figure 3-20. Unlike the concentration results, the velocity magnitude exhibits a good slope very close to 1.0 suggesting similarity between model and data. The R^2, however, is only 0.569, suggesting a poorer linearity between the predicted and experimental results. There is a tear-drop shape in the results that can be seen in the red points suggesting a bias with increasing experimental velocity magnitudes and simulation results that do not increase similarly at a large distance from the release. Here efforts to distinguish the distance based on elevation (y-direction) or z-direction (streamwise) might be more helpful because it is not clear which direction is the main contributing factor. Such an analysis is left to future work.

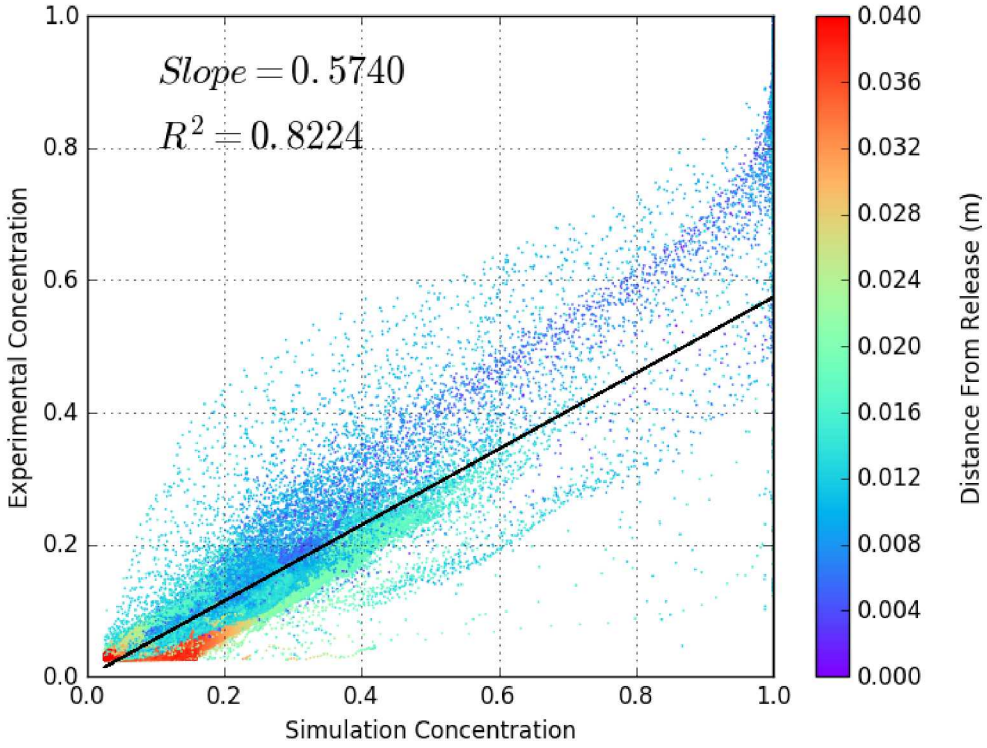

Figure 3-19. 3D Comparison of the Concentration for a 0.025 Concentration Clip

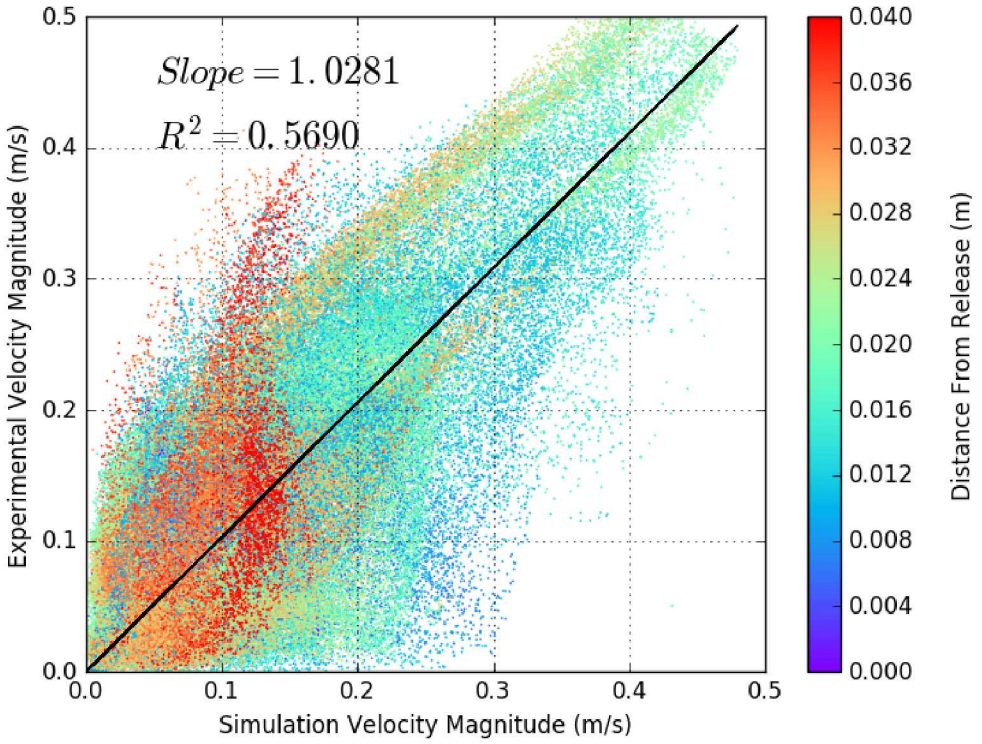

Figure 3-20. 3D Comparison of the Velocity Magnitude for a 0.025 Concentration Clip

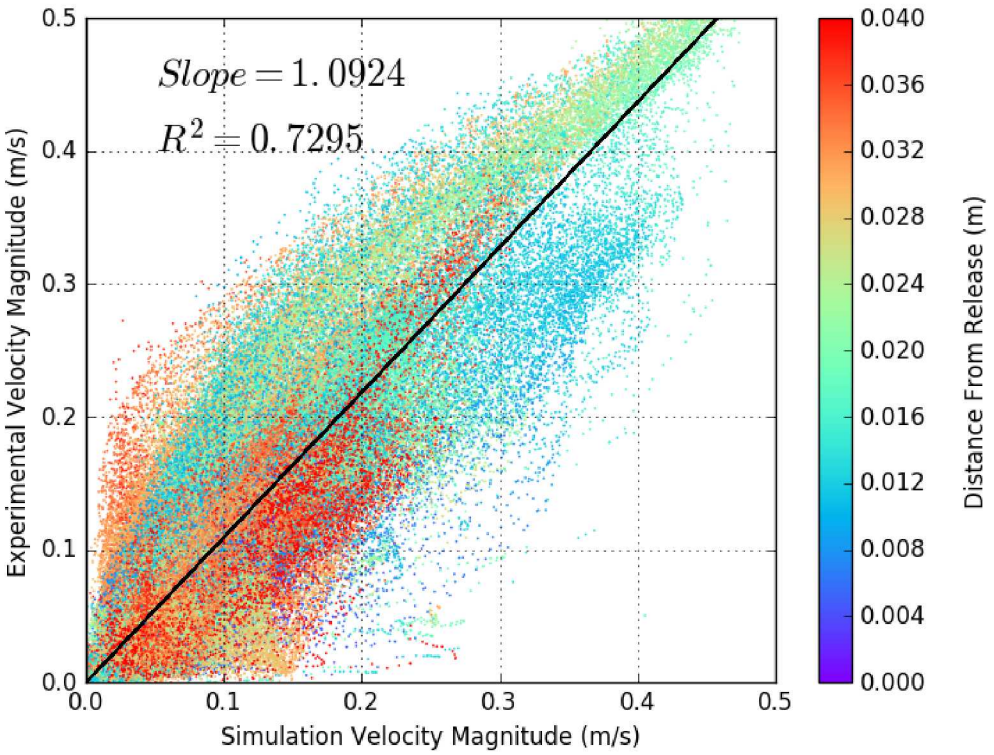

Figure 3-21. 3D Comparison for the No-Injection Simulation Case of the Velocity Magnitude for a 0.025 Concentration Clip

Figure 3-21 shows the results of velocity magnitude comparison to the no-injection case. The slope is good, and the R^2 is substantially improved over the results from the injection case to 0.73. The non-conformal 'tear drop' shape is gone, with a more linear shape of the red cloud of points along the fit line. Additional component comparison plots similar to these are found in Appendix B Additional Plots.

Table 3-1. 3D Comparison Output Metrics

Parameter	Conc.	Vel Mag.	Vel Mag. Corrected	Ideal
FB	-0.632	0.105	0.150	0
NMSE	0.386	0.192	0.129	0
MG	0.509	1.07	1.140	0
VG	1.79	1.67	1.410	0
FAC2	0.483	0.732	0.805	1
NAD	0.323	0.200	0.165	0
LND	0.456	0.355	0.309	0
LLR	0.652	0.463	0.399	0

Comparison metrics are found in Table 3-1 following the methods of HC-2012 and using the new metrics we have introduced. The concentration generally did not compare well with the data, and

what appears to be a bias would seem to be the culprit. The velocity magnitude of the baseline case did not compare particularly well either, but the corrected simulation scenario that better matches the conditions of the experiments show a general improvement. Comparisons are still not as good as found for the 90 degree scenario (Brown et al, 2019).

3.2. Line Comparisons

Besides planar and 3D comparisons, lines are used over which to compare experimental data and model results. Lines are traditionally used for comparisons, primarily because 1D data are usually taken linearly, and are thought to constitute the largest fraction of historical datasets. Locations were selected aligning with the cartesian coordinate directions. The directions are herein called Vertical (y), Streamwise (z), and Spanwise (x) and are shown in Figure 3-22. The final two directions will have results presented from three heights, 1/6 H, 1/2 H, and 5/6 H.

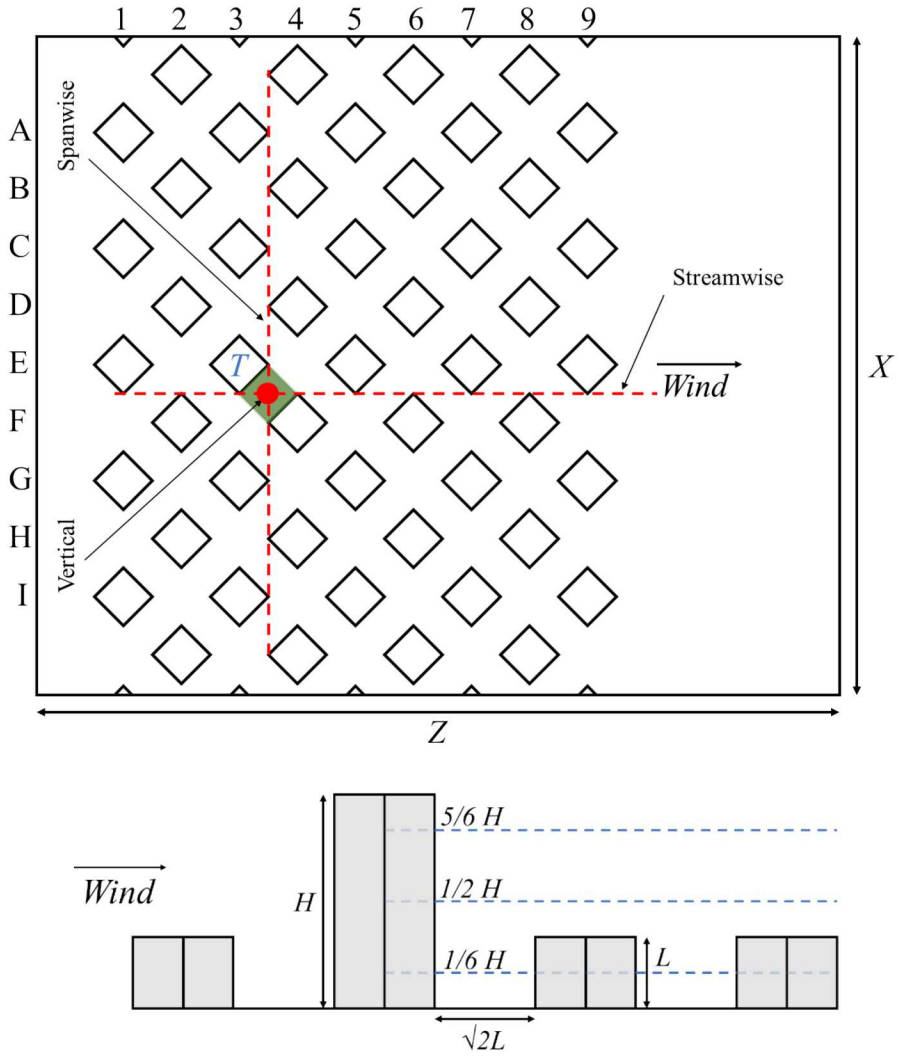

Figure 3-22. Top View (Top) of the Test Section with Row/Column Nomenclature and Standard Measurement Planes and Line Locations Illustrated by the Dashed Lines and Circles Representing an Orthogonal Line. Side View (Bottom) Showing Relative Building Heights and Investigation Line Heights.

The number of simulations run for the grid convergence and parameter studies was seventeen. An example of the number of simulation outputs is shown in Figure 3-23 with experimental data. One result indicated as 'Time' was a check of the effect of the time step, the results of which were not included in the test matrix for the report. Here the experimental uncertainty was propagated for each of the system response quantities and represented as uncertainty bands (error bars). Typically the simulation results are quite consistent except for the $k-\epsilon$ turbulence model results and the Coarse mesh results. The free-stream results show excellent agreement between simulation and experiment. Near the injection site (small values of y), the simulation predictions on concentration match very well but are higher around $1<\frac{y}{L}<3$. The velocity in this area shows even better agreement across the entire vertical line. Similar plots to Figure 3-23 for the other two line directions and three heights are shown in Appendix B Additional Plots.

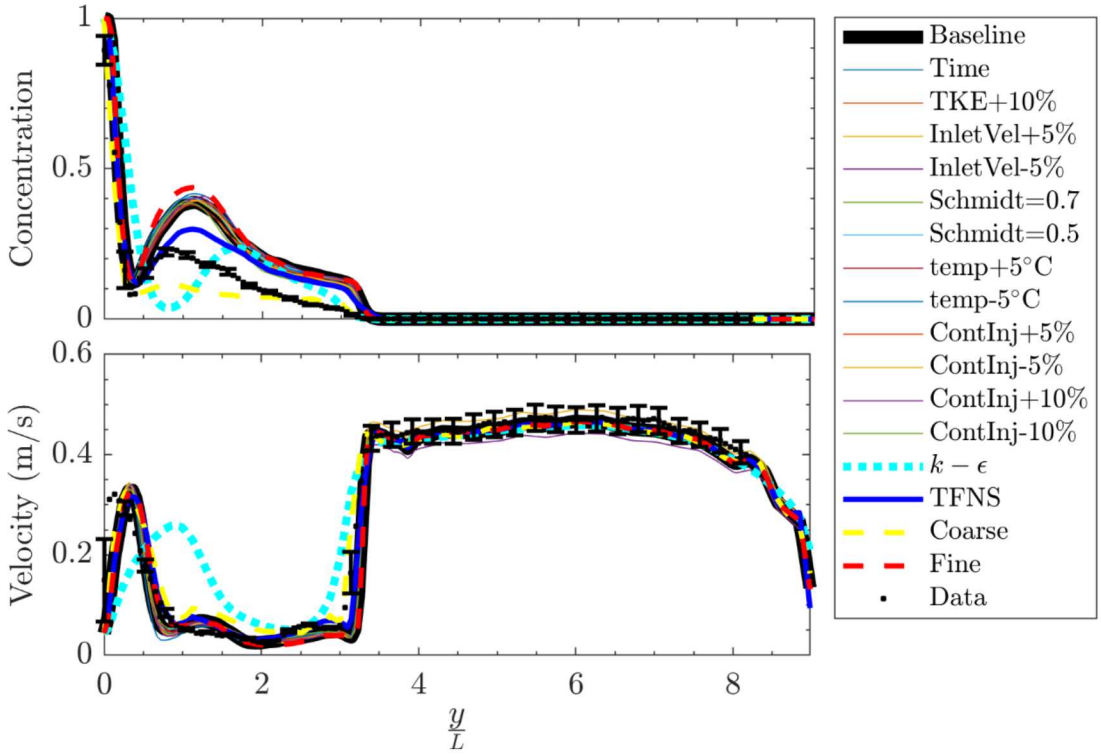

Figure 3-23. All Concentration (Top) and Velocity Magnitude (Bottom) Simulation Results with Experimental Data for the Vertical Line

3.2.1. Grid Refinement Results

The grid convergence study was intended to estimate the uncertainty of the simulation prediction from the mesh resolution, often thought to be one of the largest contributors to error in CFD. While these studies are commonly applied to RANS models with reasonable success, they are not straightforward for LES models. LES models have length-scale filtering where eddies larger than the element size are resolved and those smaller are modeled. As the mesh is resolved, there are compounding effects that require specialized efforts to circumvent through techniques such as maintaining a constant filter length as the mesh is refined (Bunge et al., 2005).

The initial results in this work reveal that the compounding effects lead to ambiguous results. Figure 3-24 shows concentration and velocity magnitude results on three meshes as well as the extrapolated results along the streamwise line at 1/6 H following the methods in the ASME V&V-20 standard (ASME, 2009). It is one of the most ambiguous examples in this study. The Medium and Fine meshes are similar, but the step from Coarse to Medium is typically quite large. This is likely due to the large refinement step of 3x from Coarse to Medium and the much smaller step of 1.33x from Medium to Fine. The grid convergence methods, including the extrapolation, consider the values of the refinement steps in their analysis. The Extrapolated values deviate by moderate amounts from the Fine curve and tend to predict greater noise than is reasonable. The extrapolation also tends toward nonphysical concentrations over unity.

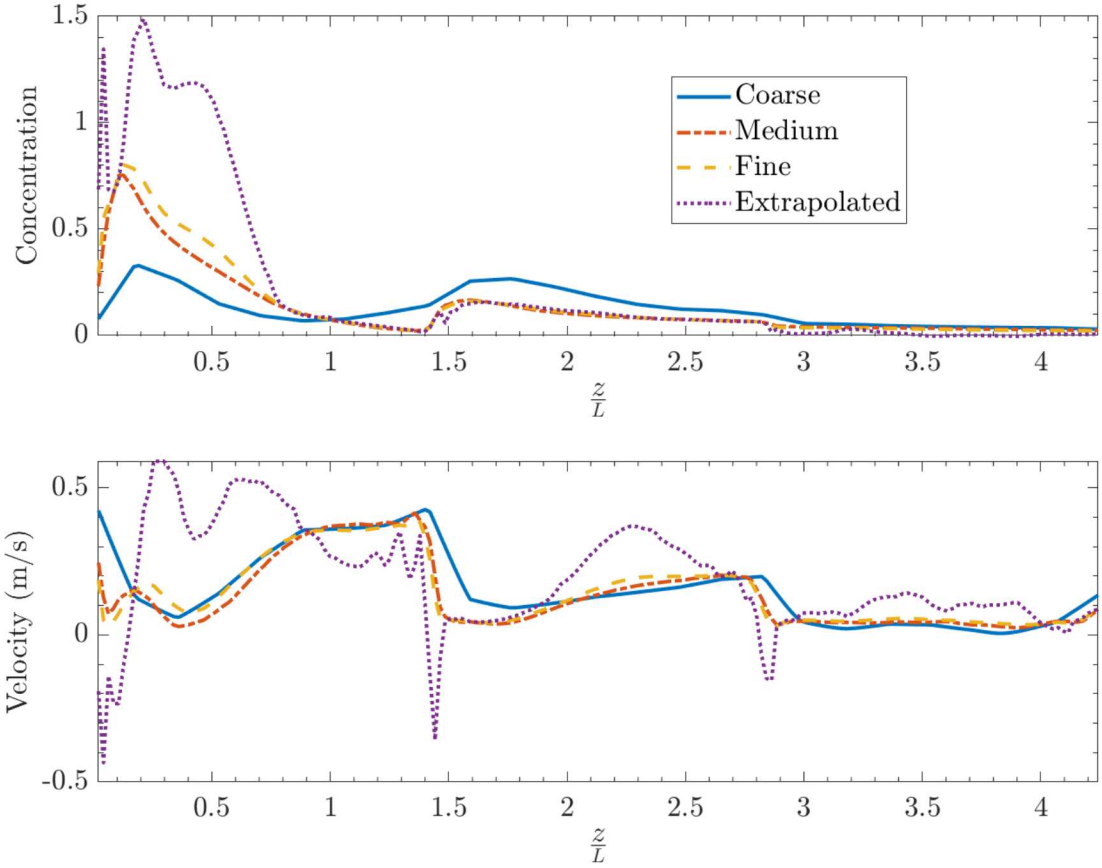

Figure 3-24. Concentration (Top) and Velocity Magnitude (Bottom) Results on Three Meshes with Extrapolated Values for the Streamwise Line at 1/6 H

Examining results with the varying levels of mesh refinement can still aid in credibility assessment as we can qualitatively compare results. The concentration and velocity magnitude results are shown with the three levels of grid refinement. Figure 3-25 shows the results on the vertical line with elevated concentration and reduced velocity near the ground level (small values of y). Note that the tall building has a height of $3L$ and the results exhibit transition to free-stream flow behavior at this elevation. While there is a moderate difference between the Coarse and Medium results, the Medium and Fine results are very similar. The Coarse mesh misses the concentration increase near $\frac{y}{L} = 0.5$ that is captured in the other two meshes. Ideally for the assessment the results should have monotonic convergence with trends moving in a single direction as the mesh is refined compared

with oscillatory convergence where the trends change direction. On the vertical line, this is generally the case but not always. The fact that these are complex turbulent flows challenges this assessment.

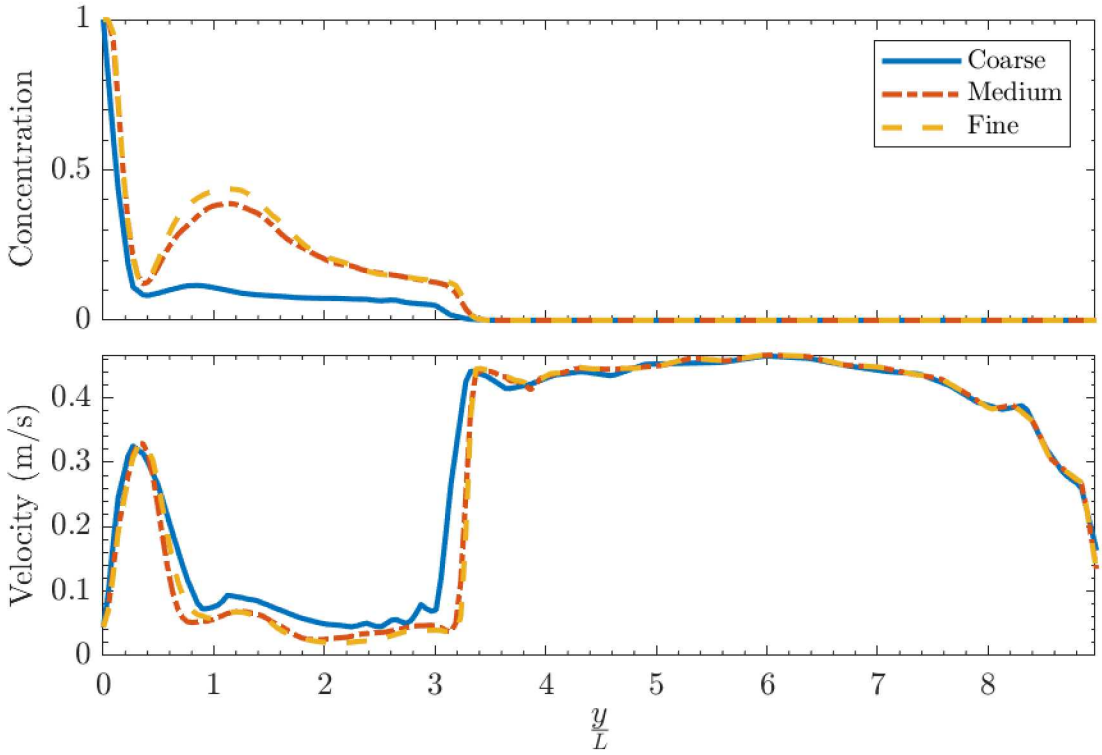

Figure 3-25. Concentration (Top) and Velocity Magnitude (Bottom) Results on Three Meshes for the Vertical Line

The streamwise results are shown at three heights. Figure 3-26 shows the results on the streamwise line at a height of 1/6 H. The results show multiple increases and decreases in both concentration and velocity magnitude that relate to the complex wake regions of the buildings. Similar to before, the Medium and Fine results are much more similar than the Coarse and Medium, and monotonic convergence is generally observed.

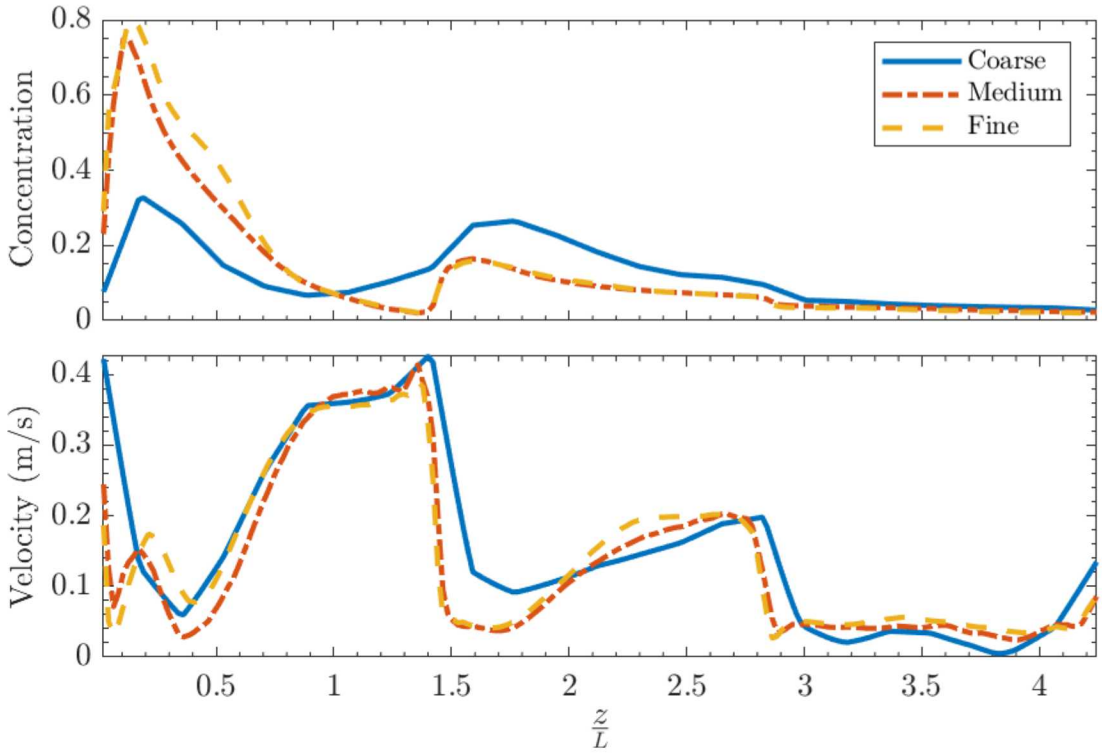

Figure 3-26. Concentration (Top) and Velocity Magnitude (Bottom) Results on Three Meshes for the Streamwise Line at 1/6 H

Streamwise results at 1/2 H are shown in Figure 3-27 and are above the smaller buildings and consequently have little evidence of building wake structure. The concentrations are lower as expected with increasing distance from ground level. The velocity magnitude captures the lower velocity wake region from the tall building that recovers to much of the free-stream value of ~0.45 m/s. The concentration trend with refinement is strictly monotonic but the velocity magnitude is generally oscillatory. The small differences between the two finer meshes builds confidence in the simulation predictions.

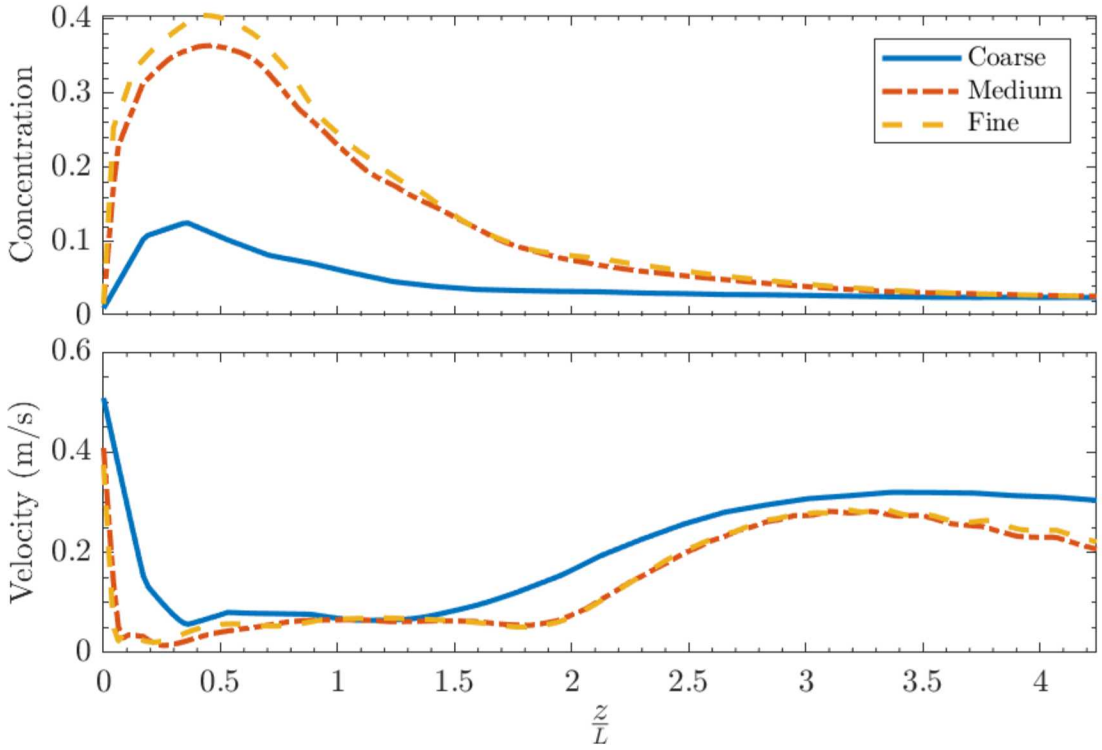

Figure 3-27. Concentration (Top) and Velocity Magnitude (Bottom) Results on Three Meshes for the Streamwise Line at 1/2 H

Streamwise results at 5/6 H are shown in Figure 3-28 and show similar behavior to those at 1/2 H except that the concentration results show greater agreement on the Medium and Fine meshes.

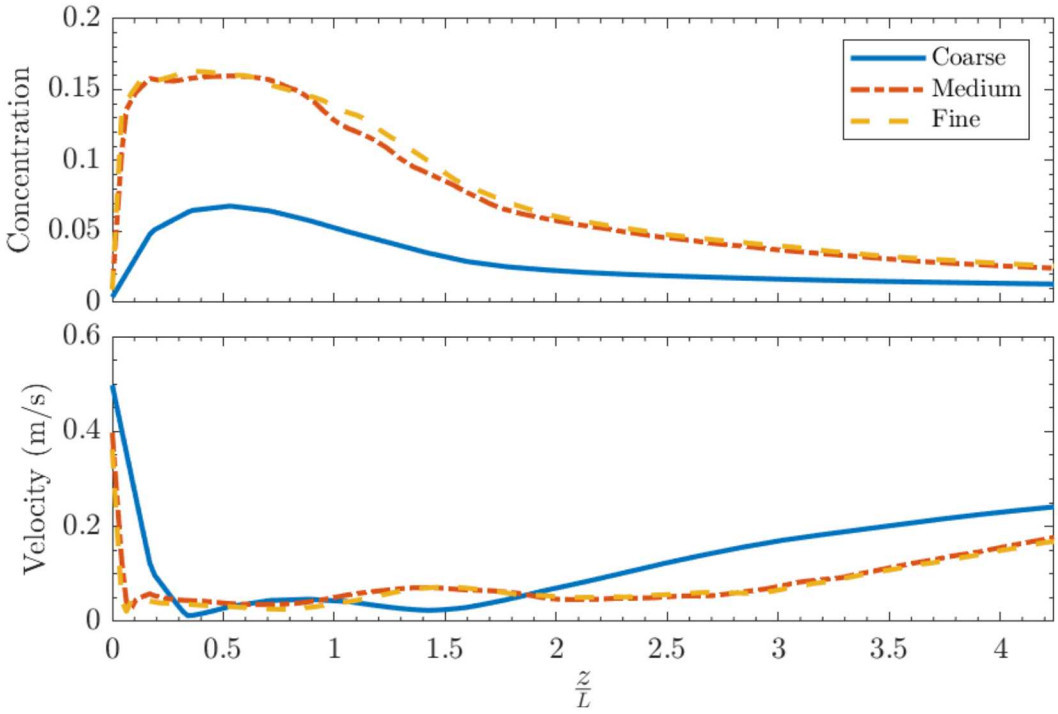

Figure 3-28. Concentration (Top) and Velocity (Bottom) Results on Three Meshes for the Streamwise line at 5/6 H

Spanwise results show greater complexity with sampling adjacent to many buildings that impose a series of wake regions. This is most pronounced at the 1/6 H line as shown in the velocity magnitude plot of Figure 3-29. Even with the complexity, the Medium and Fine results are generally consistent. The concentration shows elevated values near $x = 0$ and zero elsewhere. The behavior is mixed monotonic and oscillatory.

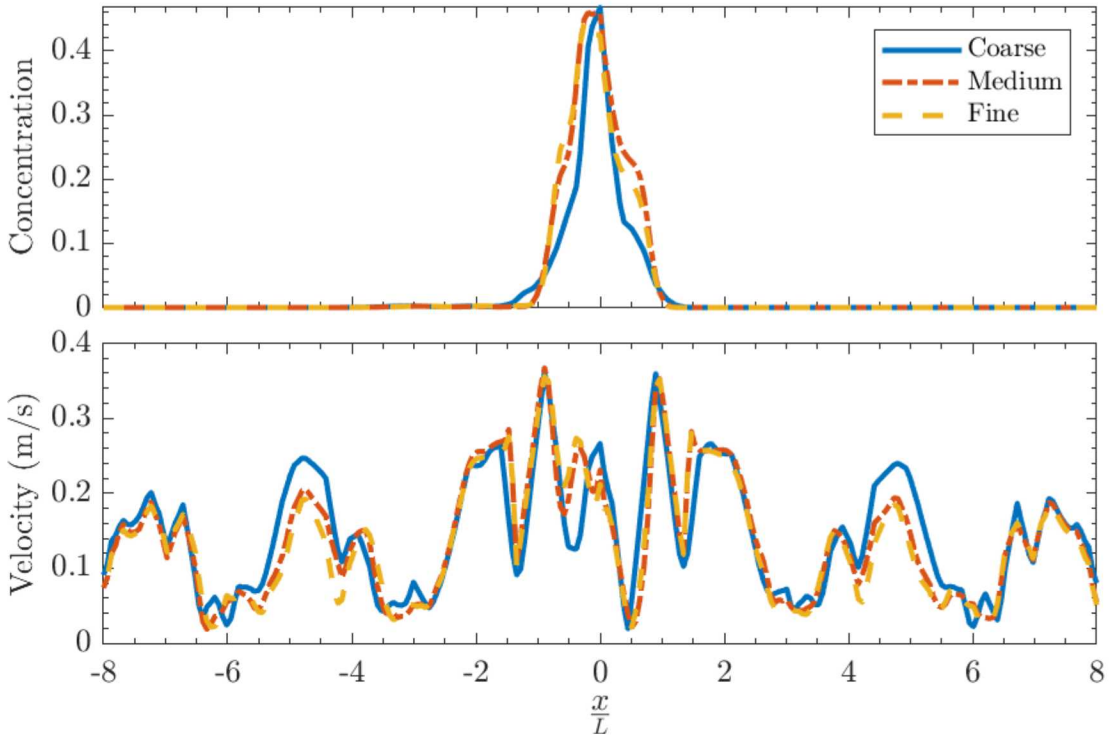

Figure 3-29. Concentration (Top) and Velocity (Bottom) Results on Three Meshes for the Spanwise Line at 1/6 H

Spanwise results at 1/2 H are shown in Figure 3-30 and show contaminant dispersion farther from the injection site as the maximum decreases and the area widens. The non-symmetry from the 45° rotation of the geometry is apparent as the concentration is higher for negative values of x, but this is only captured in the two higher resolution cases. The wake from the tall building is apparent in the low velocities near $x = 0$ and is only moderately affecting the areas above the small buildings.

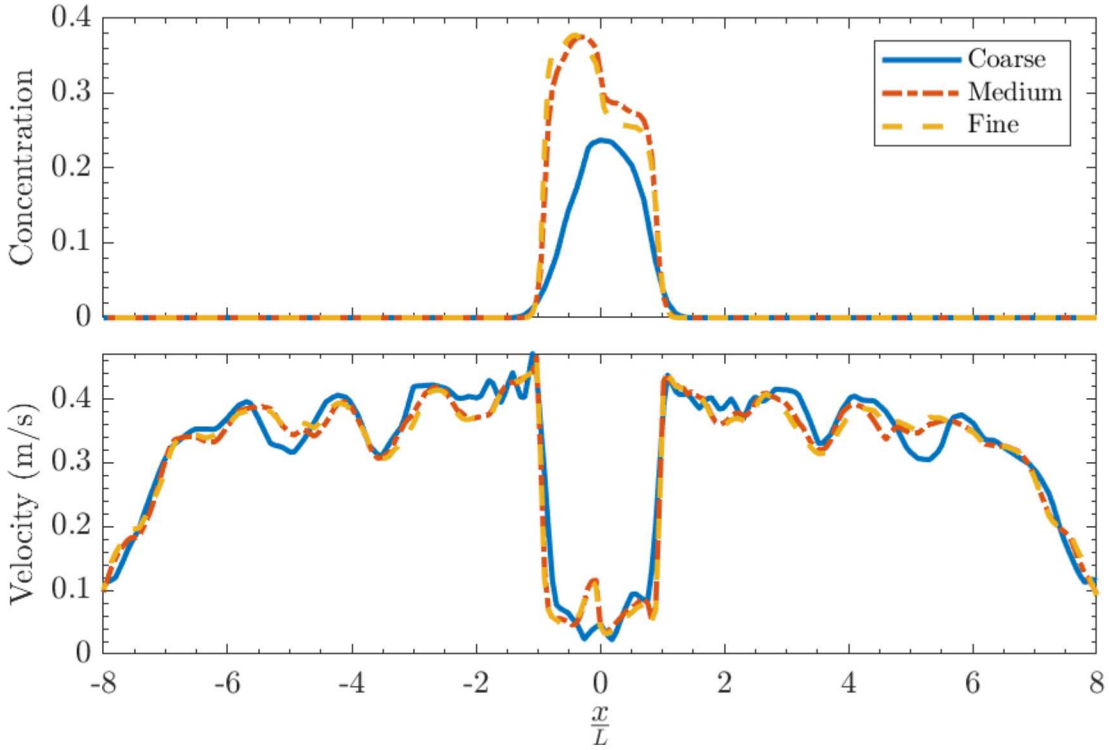

Figure 3-30. Concentration (Top) and Velocity (Bottom) Results on Three Meshes for the Spanwise Line at 1/2 H

Spanwise results at 5/6 H in Figure 3-31 show similar trends but the peak concentrations are now found for positive x as the wake region non-symmetrically drives the contaminant. The velocity magnitude results show little influence from the small building. The Coarse velocity predictions have an oscillatory behavior in space most pronounced in the wake-freestream transition area that does not occur for the other meshes.

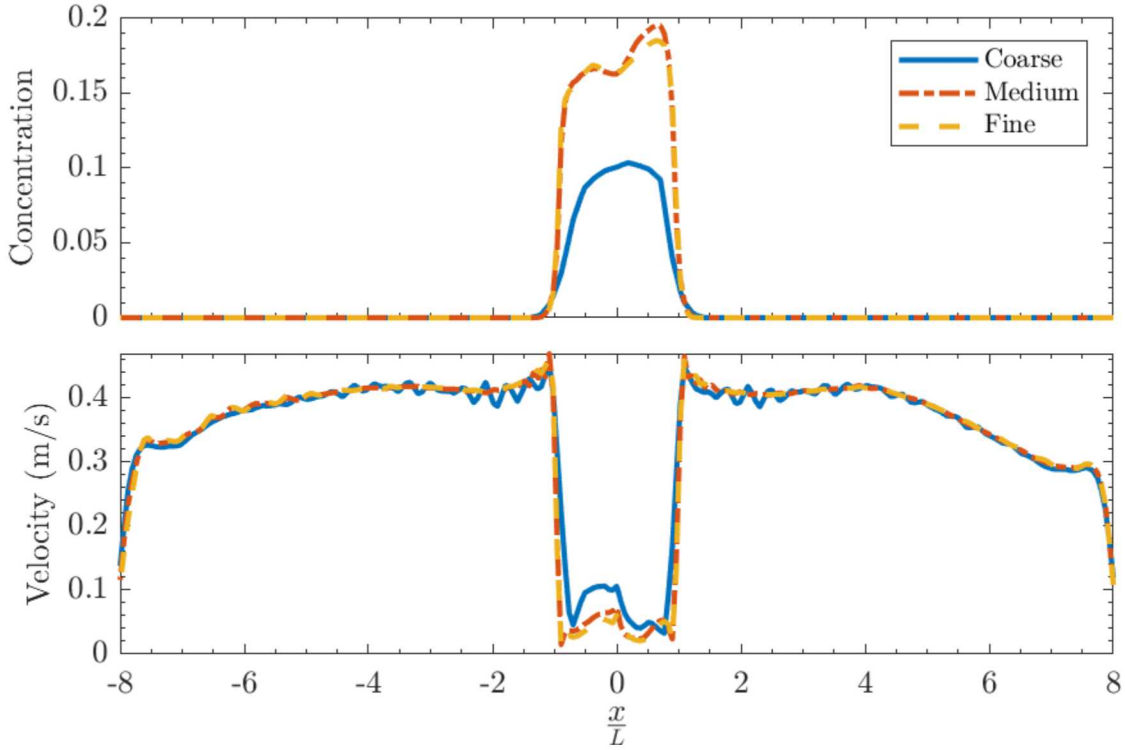

Figure 3-31. Concentration (Top) and Velocity (Bottom) Results on Three Meshes for the Spanwise Line at 5/6 H

3.2.2. Input Parameter Study Results

An input parameter study was conducted with five parameters varied independently. The local sensitivities were assessed using the methods from the ASME V&V-20 standard described previously (ASME, 2009). Because the grid convergence uncertainties from V&V-20 do not directly apply to LES simulations, only the input parameter uncertainties were used to assess simulation uncertainty.

A high-level view of the impact on input parameter uncertainty on the predicted concentration and velocity results can be obtained from analyzing importance factors. The importance factors for a set of conditions adds to unity, so relative comparisons can be made on a normalized scale. This information can guide efficient efforts to reduce simulation uncertainty by identifying the relative impact of each of the input parameter uncertainties. Figure 3-32 shows importance factors spatially averaged over all seven lines for both concentration and velocity. For concentration, the most impactful parameter is inlet velocity followed closely by turbulent kinetic energy (TKE), injection velocity, temperature. The Schmidt number has a small contribution. For velocity, the inlet velocity is most impactful followed up TKE and temperature while again injection velocity has a similarly small contribution. As expected, the Schmidt number has no influence on velocity.

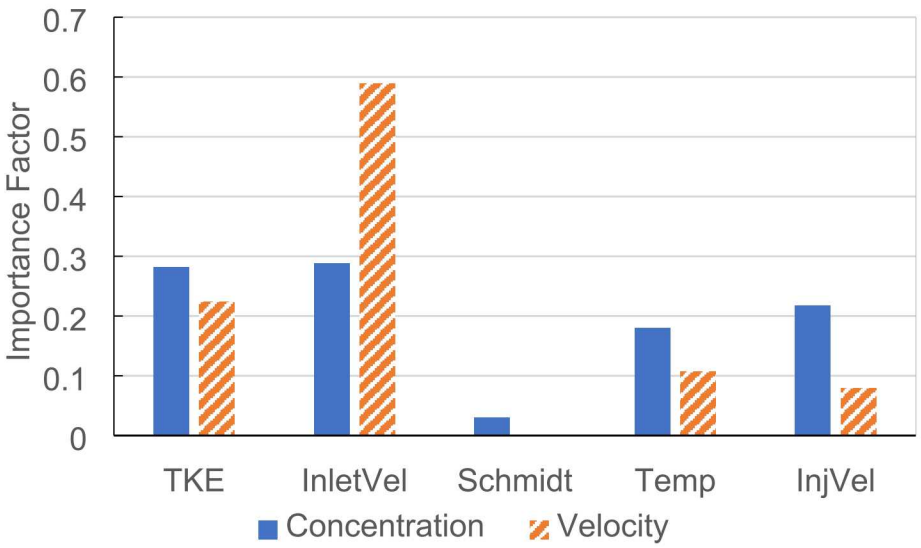

Figure 3-32. Importance Factor Results Spatially Averaged Over All Seven Line

The impact of contaminant transport is likely to negatively affect humans where exposure is higher, closer to ground level and, to a lesser degree, at building surfaces such as windows and air intakes on rooftops. It is desirable to decrease simulation prediction uncertainty at these locations especially. The importance factors spatially averaged over both 1/6 H lines are shown in Figure 3-33. Three factors for concentration are similarly dominant; injection velocity, inlet velocity, and TKE. Injection velocity is most important for concentration at the low height, a switch when considering all heights. Interestingly injection velocity is only slightly more important for velocity at the low height. Inlet velocity is much less important here, likely due to the complex influence of the building array on the boundary flow that is partially insulated from the inlet. TKE is measurably more important for velocity in this region. If simulation uncertainty should be decreased for improved predictive accuracy at the ground level, efforts to improve knowledge of inlet velocity, TKE, and injection velocity would be the most impactful.

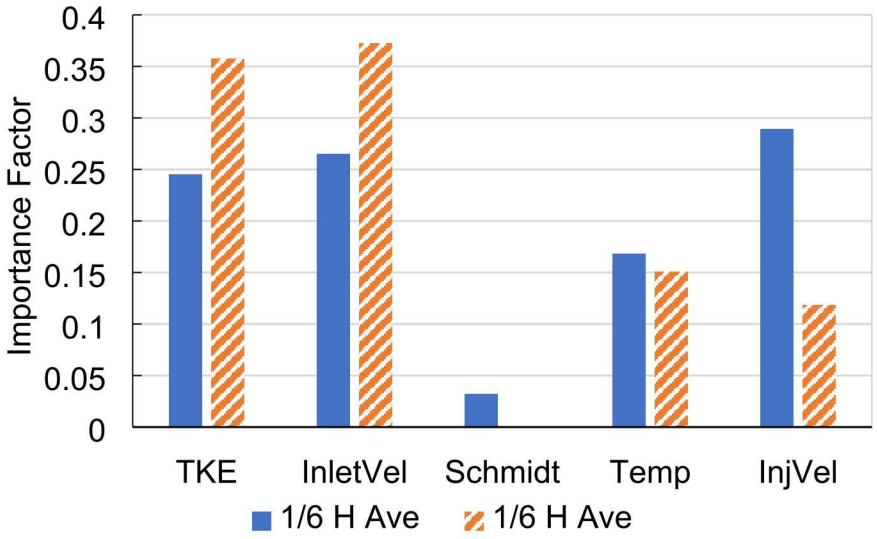

Figure 3-33. Importance Factor Results Spatially Averaged Over the Two 1/6 H Height Lines

Height's impact on importance factors shows a combination of increasing, decreasing, and mixed trends as shown in Figure 3-34 for concentration and Figure 3-35 for velocity. The two observable trends from concentration are a decreasing influence on inlet velocity and an increasing influence on injection velocity with decreasing height. Interestingly the only obvious trend for velocity is an increasing influence from TKE with decreasing height.

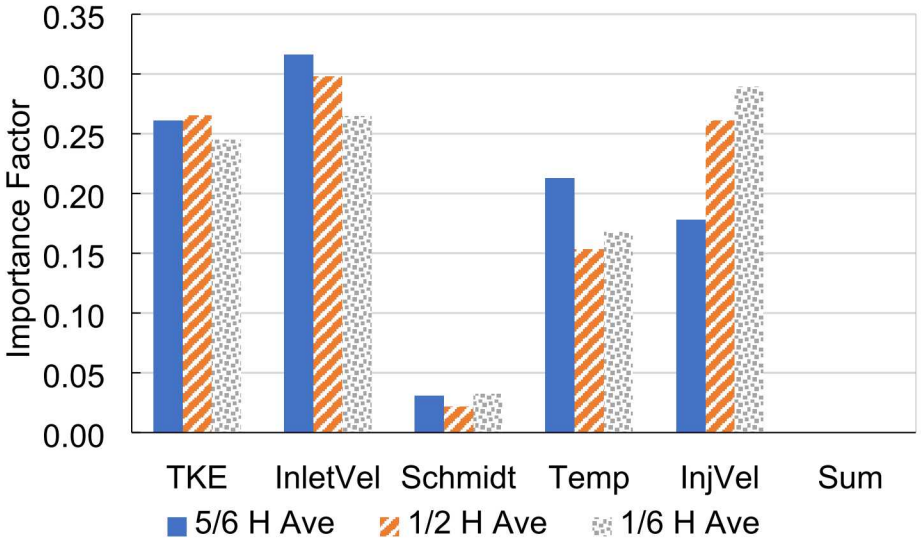

Figure 3-34. Concentration Importance Factor Results for all Three Heights

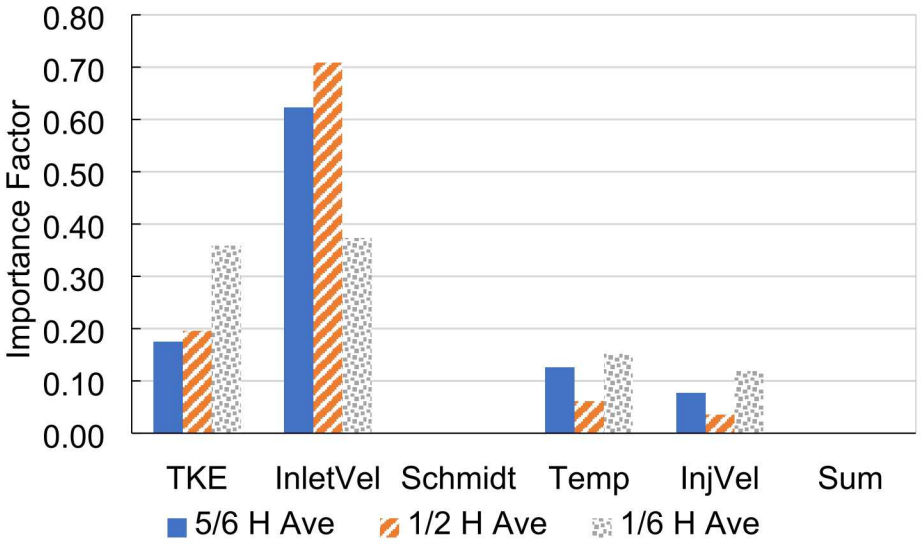

Figure 3-35. Velocity Importance Factor Results for all Three Heights

The following plots show independent parameter contributions and the root-sum-square of the parameter sensitivities on the concentration and velocity magnitude predictions along the seven lines investigated previously. Note that the parameter sensitivity results are both positive and negative

while the root-sum-square uncertainty is always positive. Keeping the sign on local sensitivities allows greater insight into the simulation behavior.

The local sensitivities on the vertical line are shown in Figure 3-36. The concentration has a large negative sensitivity to inlet velocity immediately adjacent to the injection site meaning, as expected, that the local concentration near the injection site decreases with increasing inlet velocity (bulk flow). The next largest parameter is a positive sensitivity with injection velocity. These only have local influence as the concentration is practically zero above the tall building height ($y > 3L$). In this area the Schmidt number has very low influence on the concentration predictions. The velocity magnitude has a strong positive sensitivity to inlet velocity just above the injection site with a mix of similar magnitudes in the remaining tall building wake region. The free-stream is positively sensitive to inlet velocity and insensitive to other parameters as expected. Turbulent kinetic energy (TKE) has a slight sensitivity near the top wall (large y). Through many of these results, the concentration and velocity have small relative sensitivities to concentration and velocity magnitude. This will be thoroughly shown when the root-sum-square parameter uncertainties are represented as uncertainty on the responses.

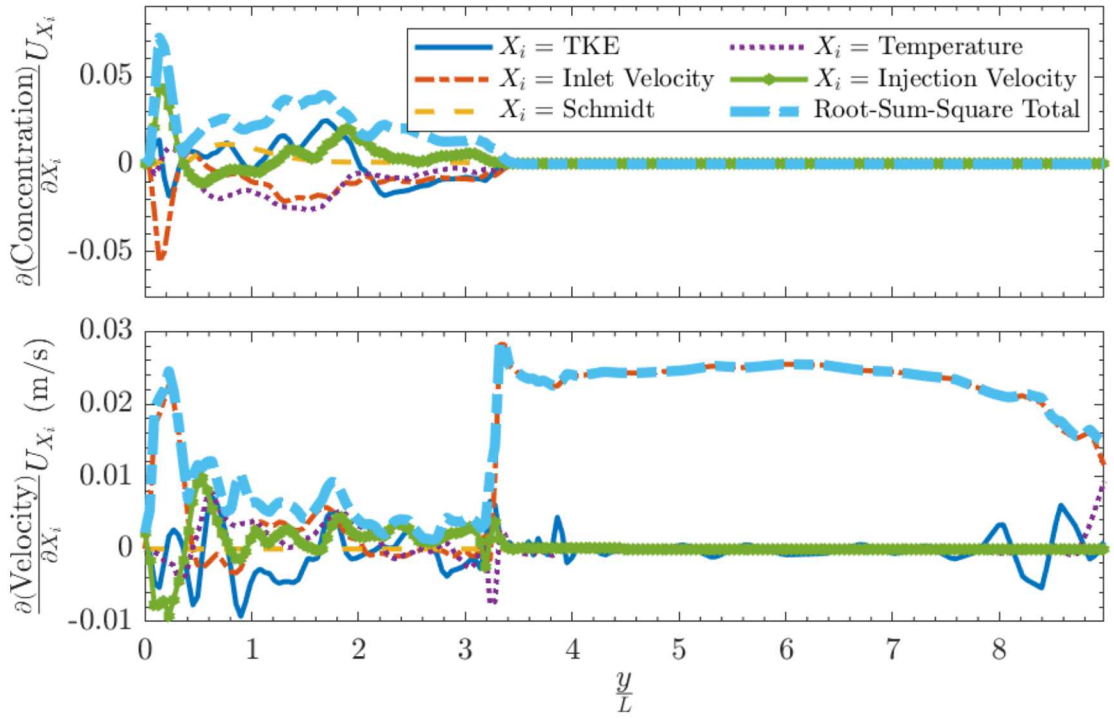

Figure 3-36. Input Parameter Sensitivities for Concentration (Top) and Velocity (Bottom) for the Vertical Line

The sensitivities along the streamwise line at 1/6 H are shown in Figure 3-37 and show several interesting trends with many parameters contributing similarly. In general the results are noisy, likely due to the complex flow structure adjacent to the small buildings at a 45° angle. Near the injection site, the temperature and injection velocity have a decreasing influence on concentration while the Schmidt number and TKE have a positive influence. Farther downstream from the injection site the sensitivities reduce and many change sign. The velocity magnitude is most heavily impacted by the inlet velocity and TKE, depending on the downstream distance.

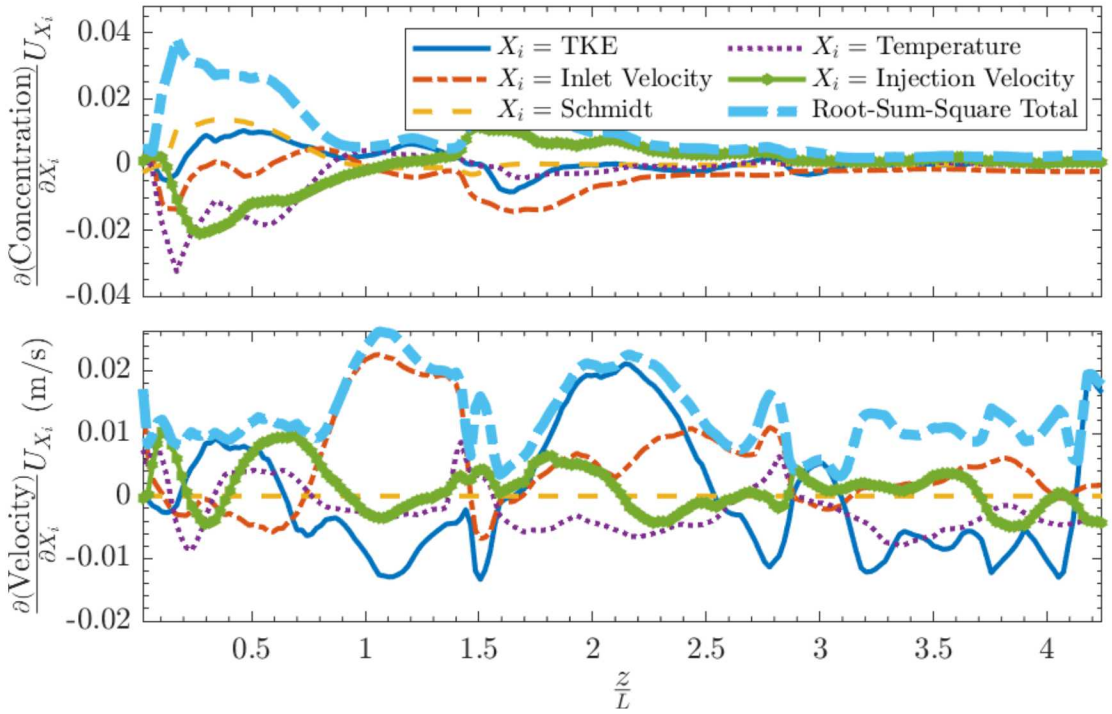

Figure 3-37. Input Parameter Sensitivities for Concentration (Top) and Velocity (Bottom) for the Streamwise Line at 1/6 H

Results for the streamwise line at 1/2 H is shown in Figure 3-38. The results tend to be less noisy, likely since the flow is more orderly in the area just above the small buildings. There are several parameters that have similar impacts on the results except the Schmidt number that has little impact on concentration and no observable impact on velocity magnitude. All concentration sensitivities decrease with downstream distance.

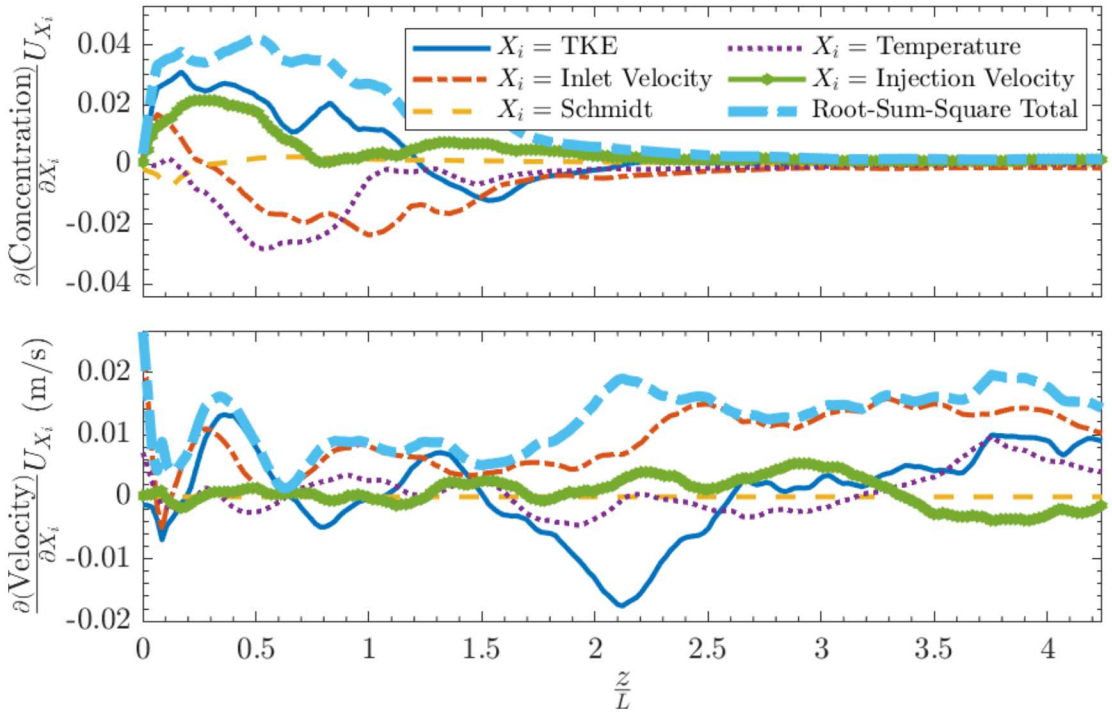

Figure 3-38. Input Parameter Sensitivities for Concentration (Top) and Velocity (Bottom) for the Streamwise Line at 1/2 H

The final streamwise sensitivities are shown in Figure 3-41 at the 5/6 H height. Turbulent kinetic energy has a strong negative influence on concentration followed by inlet velocity. The influence of the Schmidt number decreases with increasing height (from Figure 3-37 through Figure 3-41). The velocity magnitude has low sensitivities expect for TKE, inlet velocity, and injection velocity that are each sizeable at different locations.

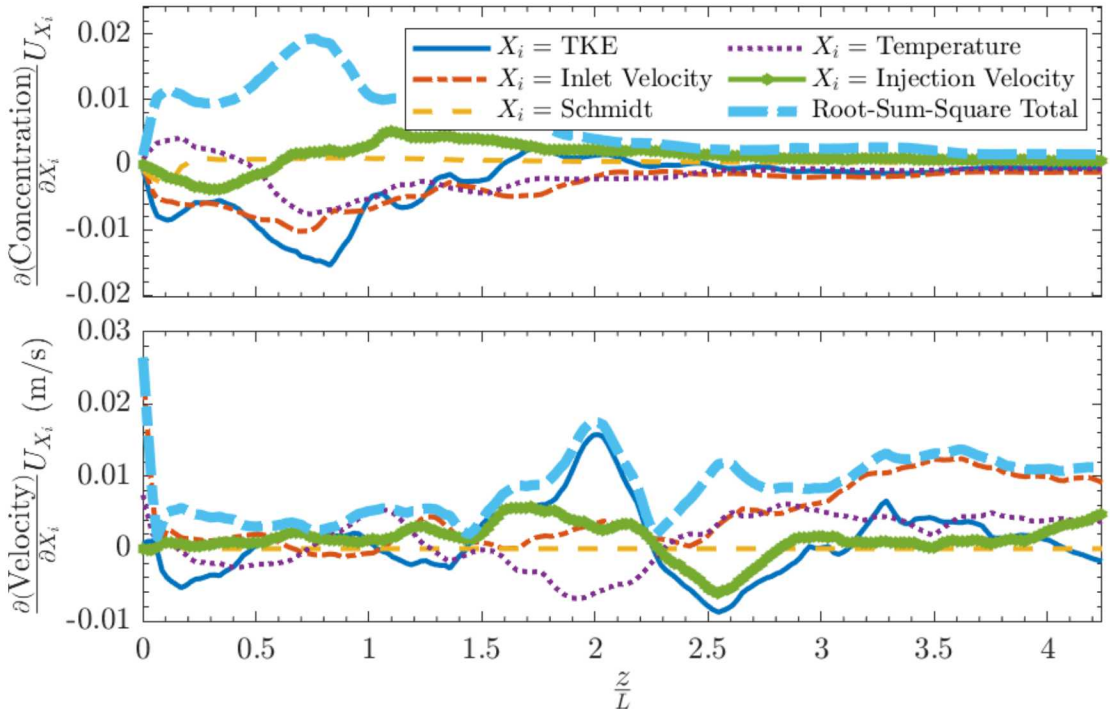

Figure 3-39. Input Parameter Sensitivities for Concentration (Top) and Velocity (Bottom) for the Streamwise Line at 5/6 H

The first spanwise sensitivity results are shown in Figure 3-40 for the 1/6 H height. The concentration only has sensitivity near the injection site that is in the wake of the large building (approximately $-1 < \frac{x}{L} < 1$). Concentration is largely dependent on TKE, inlet velocity, and injection velocity as before with little dependency on Schmidt number and temperature. The velocity magnitude sensitivities are very noisy from the flow structures with the same top three parameter influencing concentration except that temperature has a slightly higher influence.

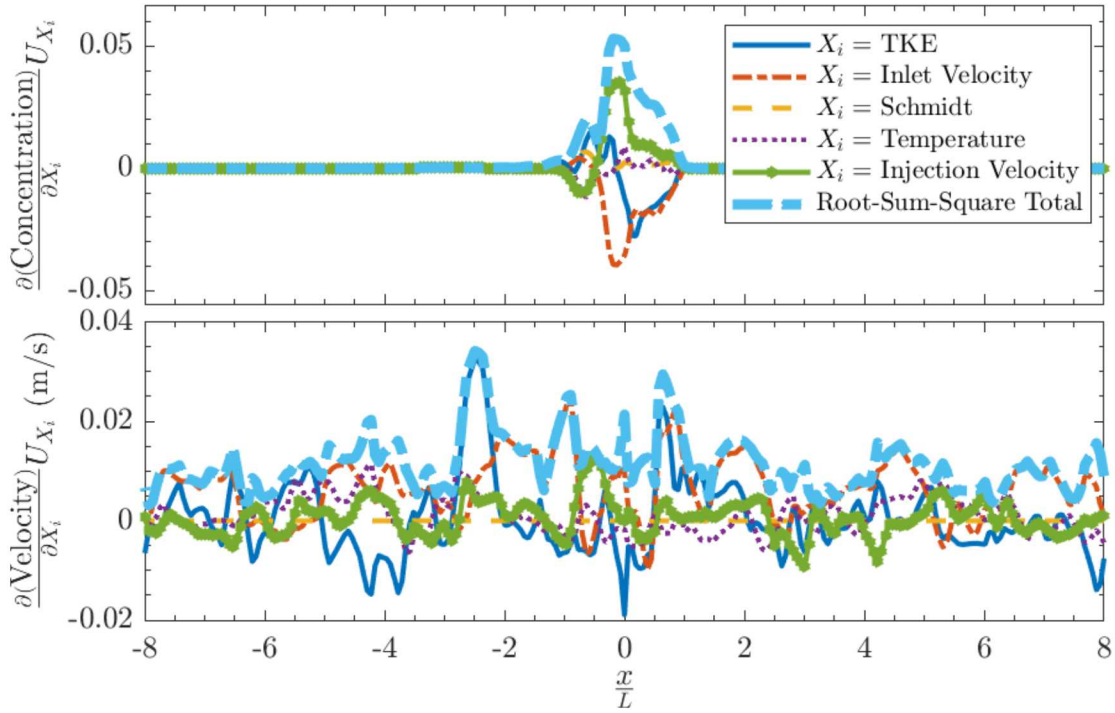

Figure 3-40. Input Parameter Sensitivities for Concentration (Top) and Velocity (Bottom) for the Spanwise Line at 1/6 H

The noise levels reduce with increasing height to 1/2 H as shown in Figure 3-41. The concentration shows some impact with decreases from increasing temperature. This line is sufficiently above the small building height so the inlet velocity has the largest influence on velocity magnitude that is positive. Again the Schmidt number has little impact on concentration and none on velocity.

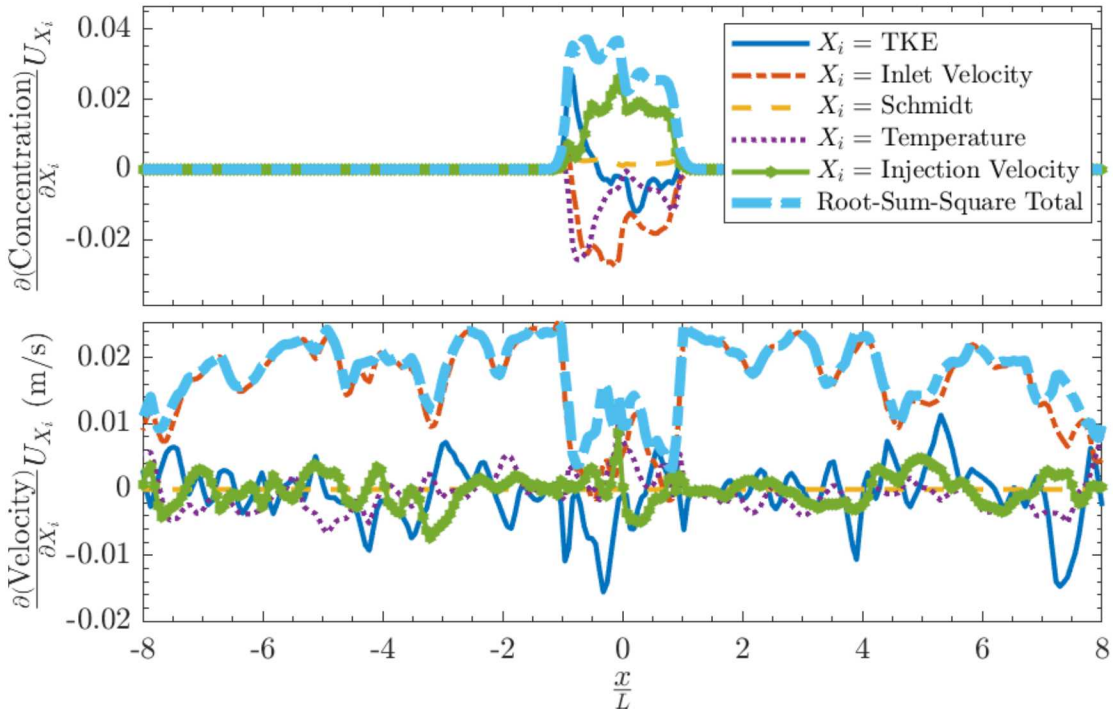

Figure 3-41. Input Parameter Sensitivities for Concentration (Top) and Velocity (Bottom) for the Spanwise Line at 1/2 H

Finally the sensitivities at the 5/6 H height are shown in Figure 3-42 with similar trends and even less noise. Concentration still has a measurable sensitivity to temperature as the fourth highest impactful parameter. Overall, the three most influential parameters are TKE, inlet velocity, and injection velocity with similar magnitudes. The fourth is temperature and the Schmidt number is clearly the lowest.

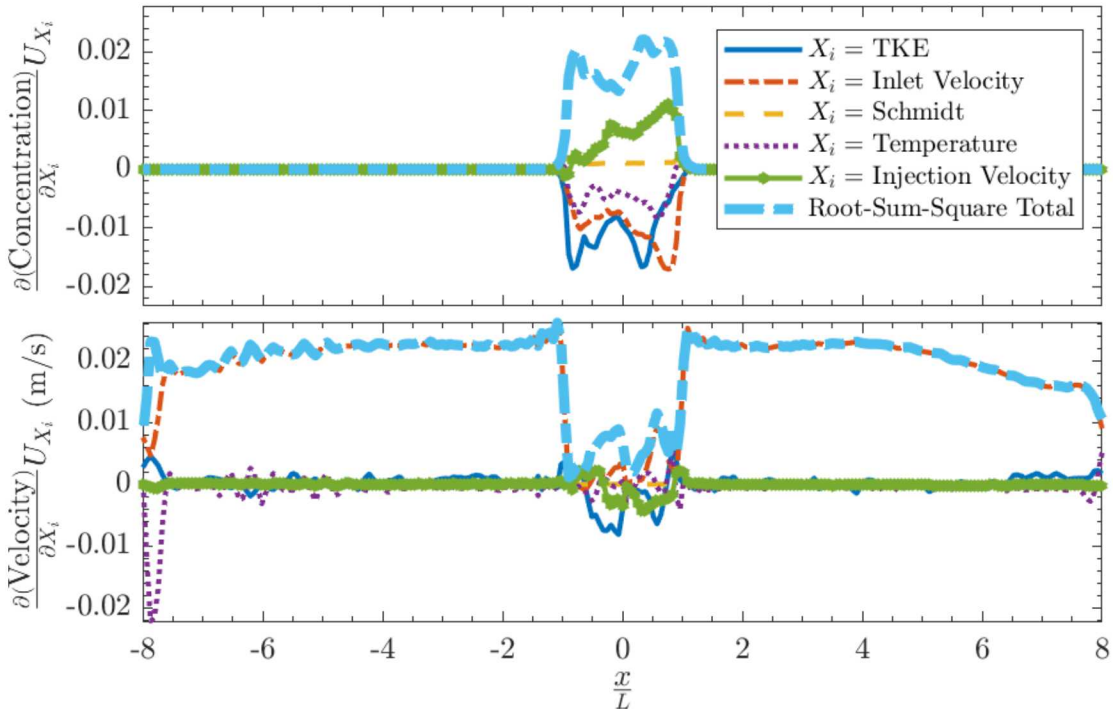

Figure 3-42. Input Parameter Sensitivities for Concentration (Top) and Velocity (Bottom) for the Spanwise Line at 5/6 H

3.2.3. Complete Line Results

The final results include line plots of the baseline LES simulations with a comparison to experimental data that were acquired for the same conditions. The LES results have parameter uncertainty represented in a cloud and the experimental results have traditional uncertainty bands (error bars). Note that LES results are shown on the medium mesh that was used for the parameter study. Also shown are TFNS and k-ϵ simulation results for relative accuracy comparisons. The first results are shown in Figure 3-43 for the vertical line. The LES and TFNS concentration predictions have excellent agreement immediately adjacent to the injection site then tend to moderately overpredict. The difference is greater than the uncertainty coverage of both LES and experiment, suggesting that the uncertainty estimates are not conservative or that model form error remains. It is very possible that the simulation uncertainty is underpredicted because it does not include the adequacy of the mesh from solution verification activities due to the lack of best practices for LES. Compared with concentration, the velocity magnitude results have better agreement. The only appreciable differences are near the injection site. As will be shown, this is largely due to difference in the experiment having a no-injection condition when the velocity was measured that affected the velocity near the injection site. Away from this location, the velocity has excellent predictive accuracy through most of the domain height.

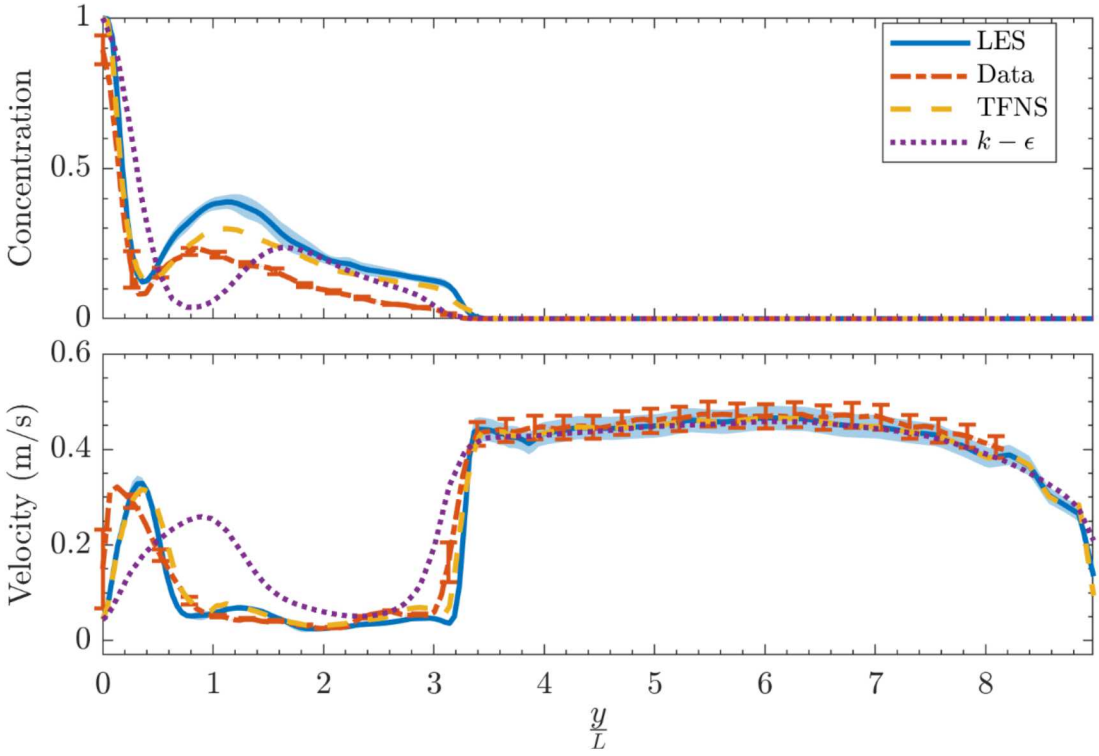

Figure 3-43. Baseline LES Results Compared with Experimental Data as well as TFNS and $k-\epsilon$ Predictions for the Vertical Line

The first streamwise results are at 1/6 H and shown in Figure 3-44. The concentration agreement is much improved with the LES and TFNS predictions having similar accuracy while the $k-\epsilon$ results are much less accurate. A common theme that was observed is the greater similarity between LES and TFNS results than to the $k-\epsilon$ results. The velocity predictions are more challenging near the street level and some differences are observed. The features are aligned in space but the simulations tend to predict sharper velocity gradients than were measured. The experimental data have a local peak beyond z/L of 3.5 that is not predicted.

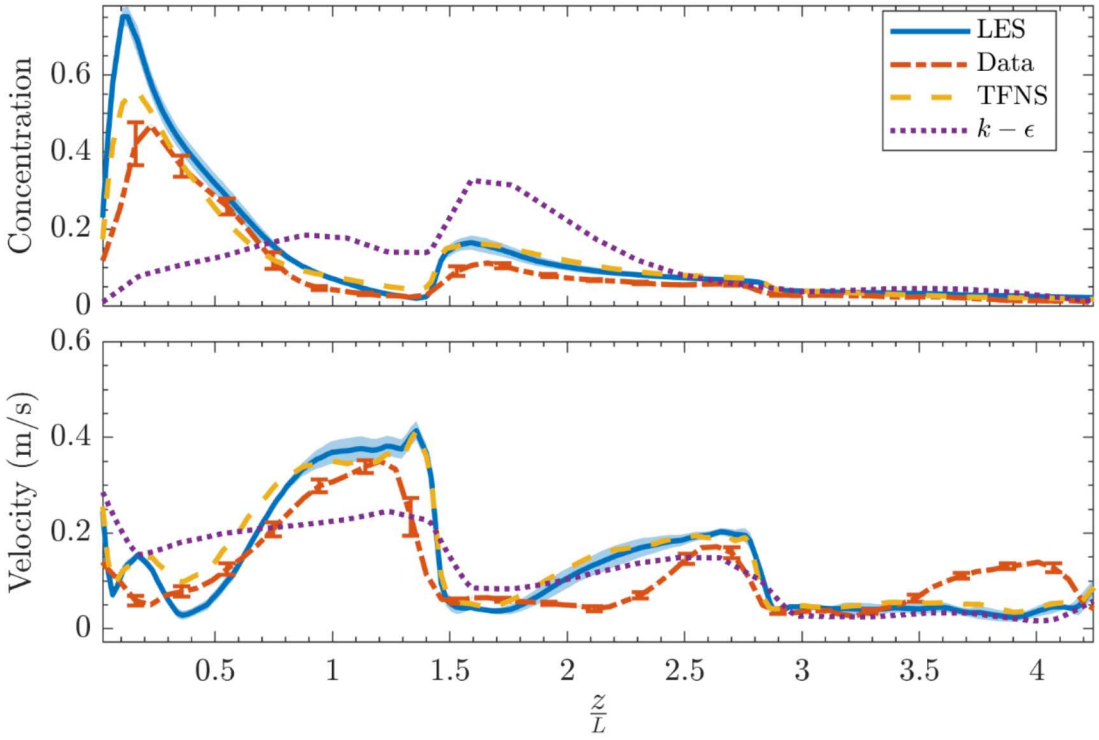

Figure 3-44. Baseline LES Results Compared with Experimental Data as well as TFNS and $k-\epsilon$ Predictions for the Streamwise Line at 1/6 H

The streamwise results at 1/2 H are shown in Figure 3-45. While the trends for all the predictions are similar, the concentration predictions of the $k-\epsilon$ simulation is most accurate near the injection location followed by TFNS and LES. This is repeated at the 5/6 H height as well and is different from what was expected at the latter two simulations have greater ability to model dynamic flows that have large separation zones such as this. Conversely, the LES and TFNS predictions are much more accurate for velocity with excellent agreement through the first half of the downstream length and a somewhat higher predictions downstream.

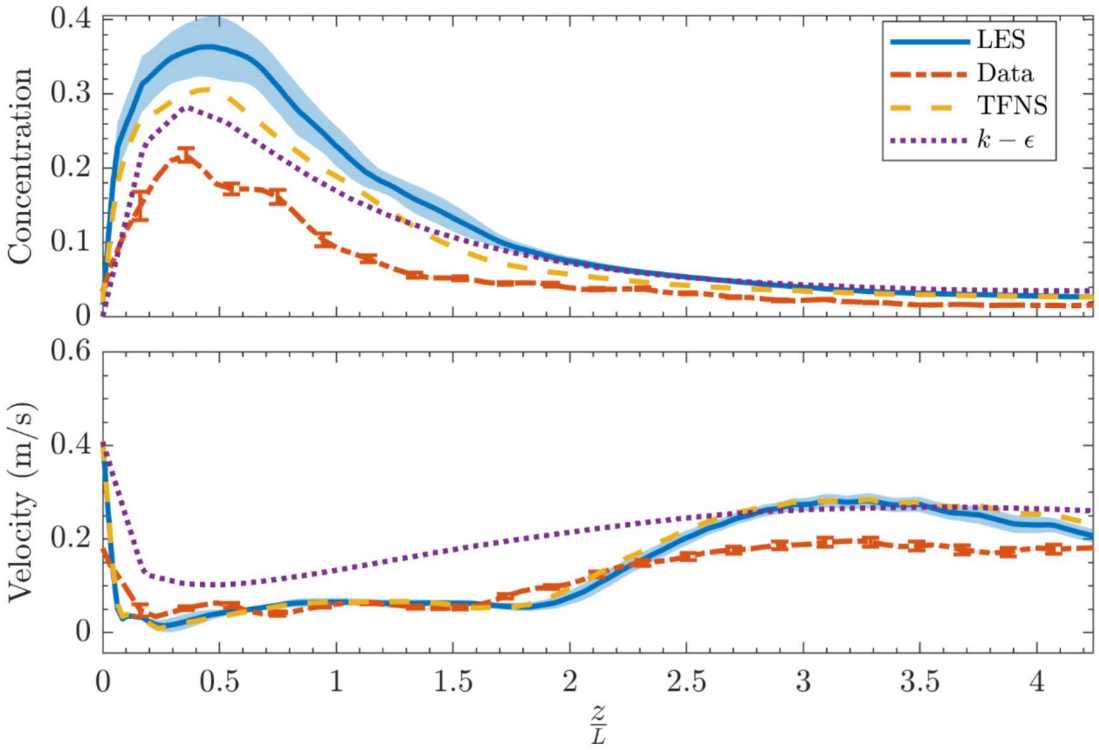

Figure 3-45. Baseline LES Results Compared with Experimental Data as well as TFNS and $k-\epsilon$ Predictions for the Streamwise Line at 1/2 H

The highest streamwise results at 5/6 H are shown in Figure 3-46 and also show high concentration predictions and excellent velocity predictions. The concentration parameter uncertainty is relatively large near injection and decreases downstream.

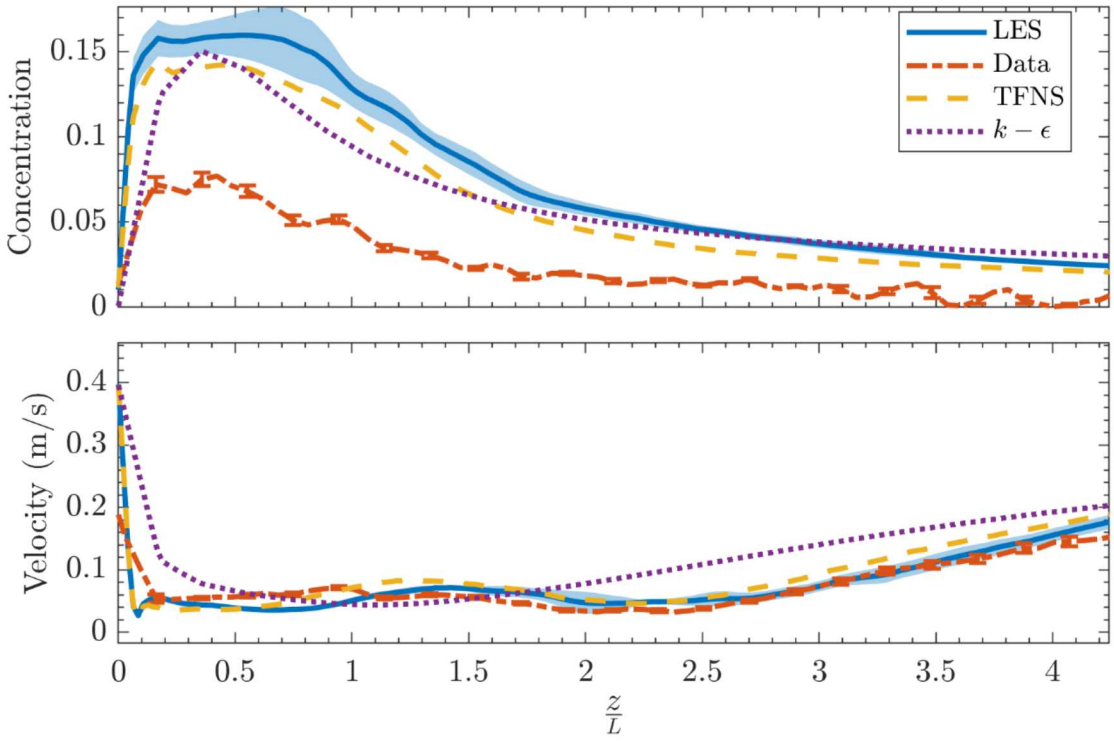

Figure 3-46. Baseline LES Results Compared with Experimental Data as well as TFNS and $k-\epsilon$ Predictions for the Streamwise Line at 5/6 H

The spanwise comparisons near the street level at 1/6 H are shown in Figure 3-47. In this direction, the concentration peak prediction is closer to that from the experiment but with a shift in the $-x$ direction. Here the LES and TFNS predictions are more accurate except in the very narrow band near $x = 0$ that was investigated in the streamwise plots. This orthogonal sampling shows the value in the large number of interrogation lines and resulting figures in this work because the apparent greater accuracy of the $k - \epsilon$ results in previous figures is shown to only be a very localized event. Similar to before, the velocity results near the street level are very noisy but good agreement is still found. The trends are similar and aligned in space with the simulations predicting slightly higher velocities. The experimental velocity minima tend to be near zero, possibly due to lower accuracy near the noise floor of the measurements.

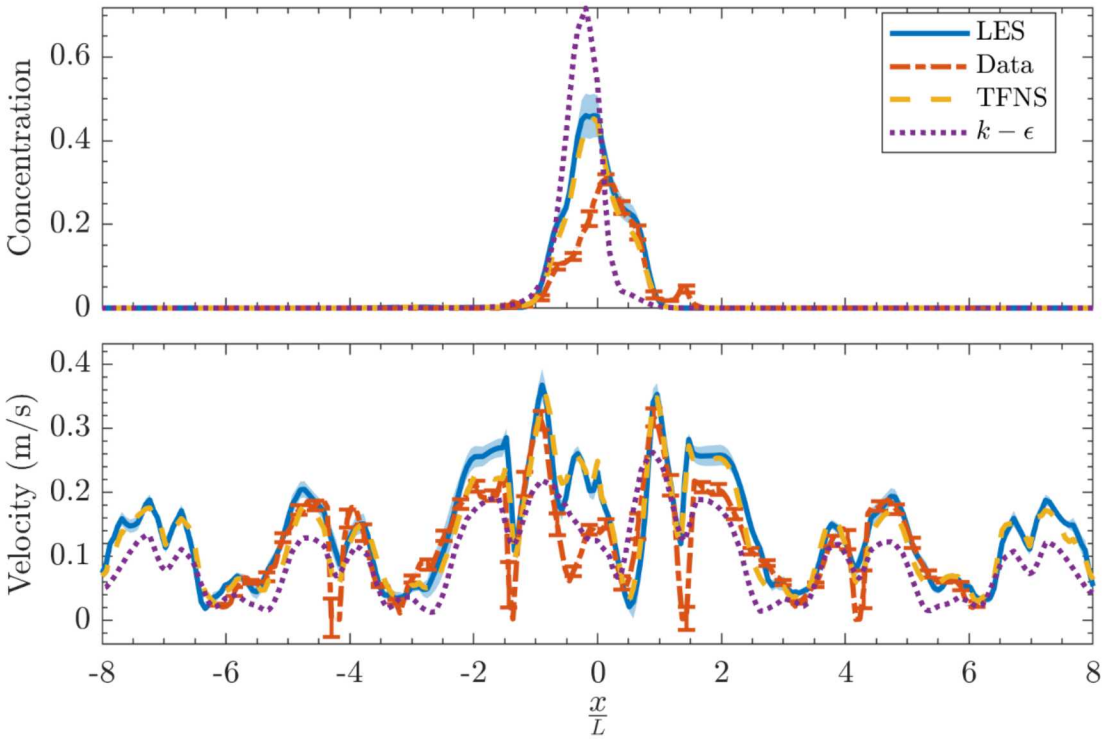

Figure 3-47. Baseline LES Results Compared with Experimental Data as well as TFNS and $k - \epsilon$ Predictions for the Spanwise Line at 1/6 H

The spanwise results at 1/2 H are shown in Figure 3-48. The concentration predictions are similar and about a factor of two higher than in the experiments. The predictions tend to peak towards negative values of x while the measurements peak to positive values. The velocities have very good agreement, even in the challenging area of the tall building wake. Interestingly, the $k-\epsilon$ results capture the symmetric behavior in the wake itself. Similar to before, the simulations predict greater velocity gradients but there is little difference when the uncertainties are considered.

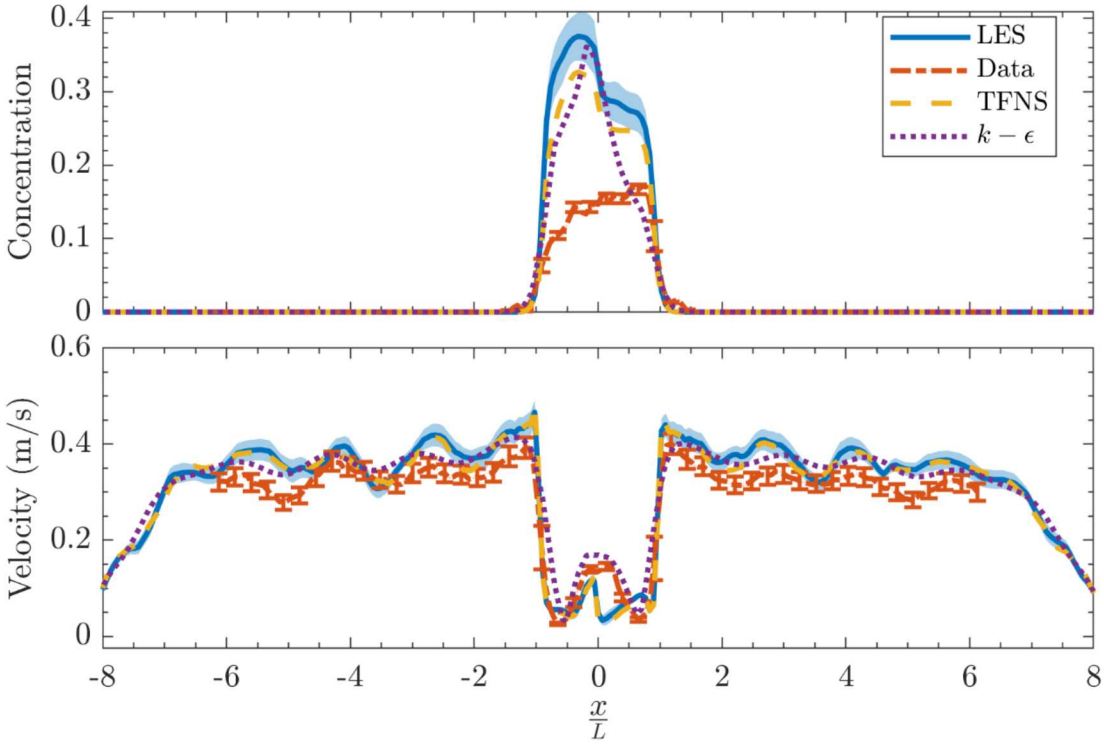

Figure 3-48. Baseline LES Results Compared with Experimental Data as well as TFNS and $k-\epsilon$ Predictions for the Spanwise Line at 1/2 H

Finally the high 5/6 H results for the spanwise line are shown in Figure 3-49. The concentration predictions are elevated by about a factor of three and show non-symmetry that is not in the data. The peak concentration prediction switched sides due to the non-symmetric wake that was shown in the contour plots. The concentration magnitudes are more accurately predicted closer to the injection location (smaller values of H) suggesting that there is a difference in contaminant transport properties, though the insensitive nature of the predictions to Schmidt number suggest this is not likely to be the cause. The velocity predictions are excellent and almost exclusively have overlapping uncertainty with the experiments.

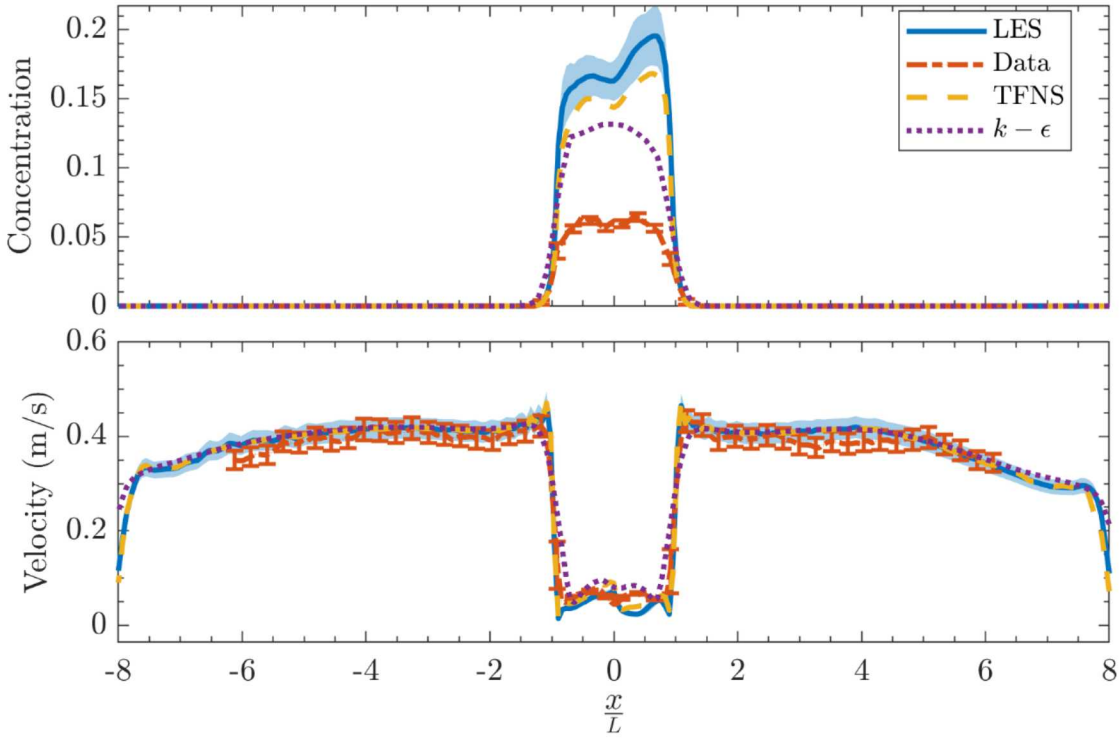

Figure 3-49. Baseline LES Results Compared with Experimental Data as well as TFNS and $k-\epsilon$ Predictions for the Spanwise Line at 5/6 H

3.2.4. No Injection Velocity Results

Oberkampf and Roy discuss best practices for validation studies with the need for open, two way communication between experimental and modeling teams so that information is appropriately shared and understood (Oberkampf and Roy, 2010). This project contains a good lesson for others that wish to do validation studies. There was a miscommunication on the boundary conditions at the injection site where the injection port was plugged when velocity measurements were obtained and the modeling team was not informed. The baseline LES velocity results presented previously included injection. The following line comparisons show improved simulation accuracy for velocity components when boundary conditions were matched.

Velocity components in all three of the principle directions are compared, spanwise velocity u, vertical velocity v, and streamwise velocity w. The baseline LES results do not include parameter uncertainty propagation while the experimental results include their component velocity uncertainties. Figure 3-50 shows the velocity component results for the vertical line that show general improvement for the LES-No Injection case, especially near the injection site. The injection

locally impacts the wake region that traverses the vertical sampling line up to $y = 3L$ but has no noticeable effect in the free-stream.

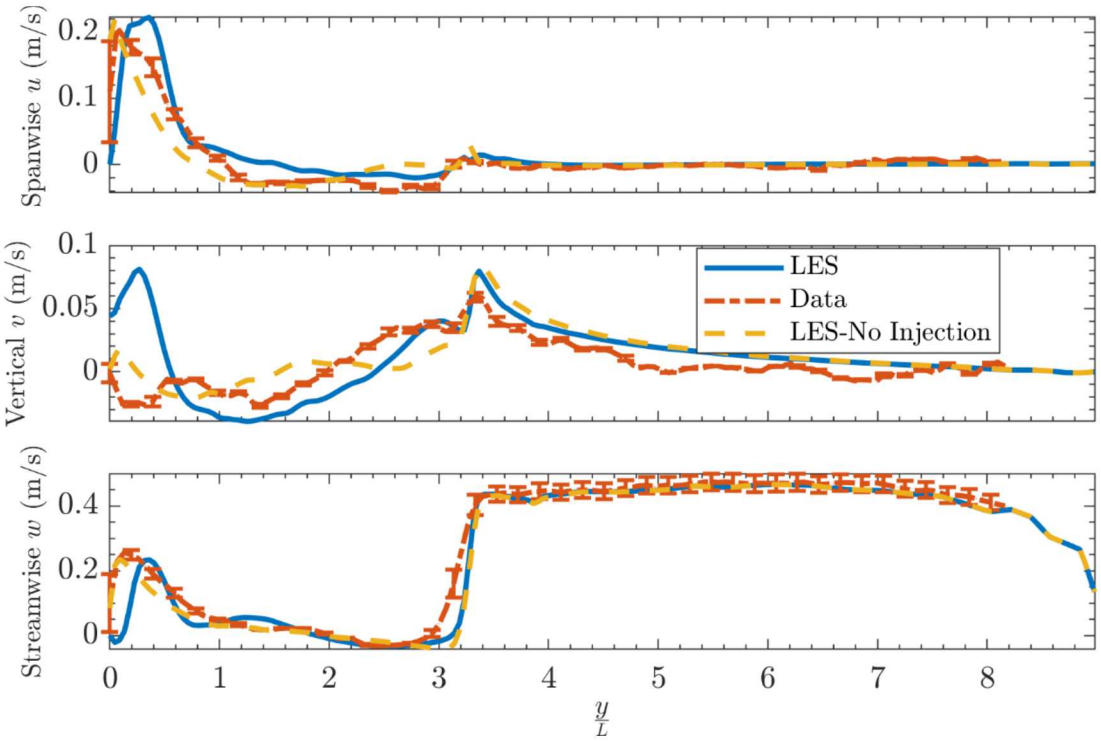

Figure 3-50. Velocity Components for the Baseline LES and No Injection LES Results Compared with Experimental Data for the Vertical Line

The No Injection results show much greater improvement in the remaining results, especially near the injection site and downstream near the ground level. The results in the streamwise direction at 1/6 H are shown in Figure 3-51. The vertical velocity v shows much better agreement with a significant improvement immediately downstream of the injection site. The other velocity components show measurable improvement throughout the sampling line.

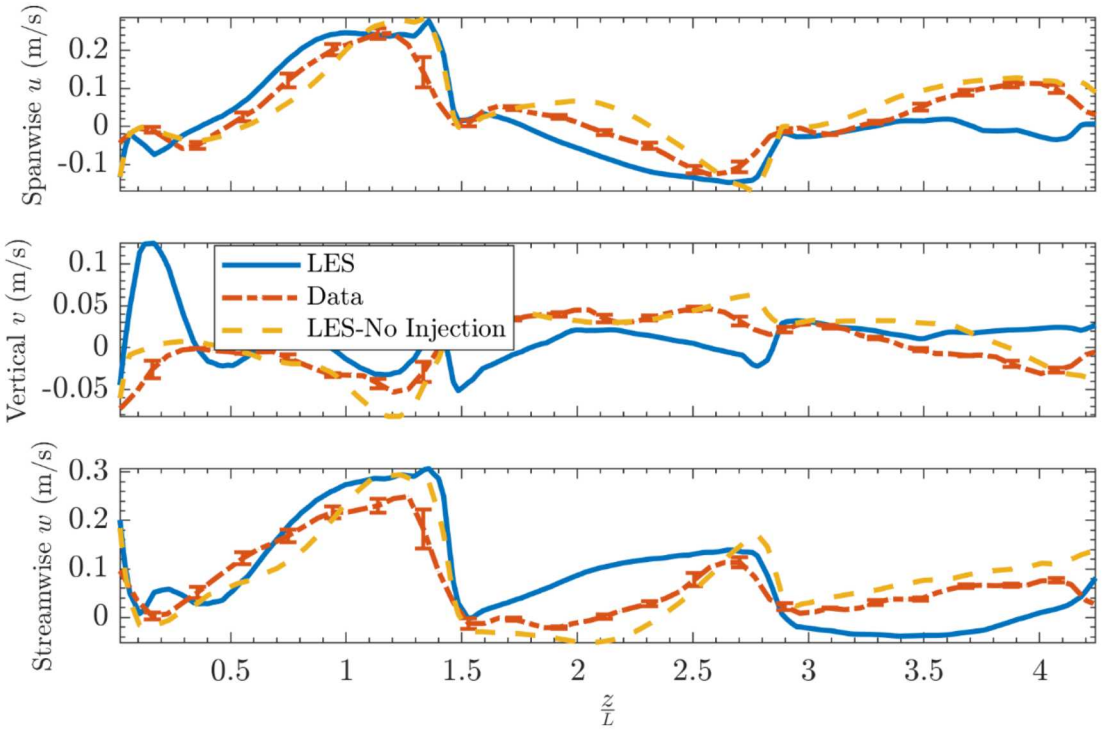

Figure 3-51. Velocity Components for the Baseline LES and No Injection LES Results Compared with Experimental Data for the Streamwise Line at 1/6 H

General accuracy improvement is seen in Figure 3-52 for the streamwise line at 1/2 H. This is especially true for the streamwise and spanwise velocity components where the data trends are captured much better by the No Injection LES results. It is interesting to note that the accuracy improvements carry far downstream of the injection site.

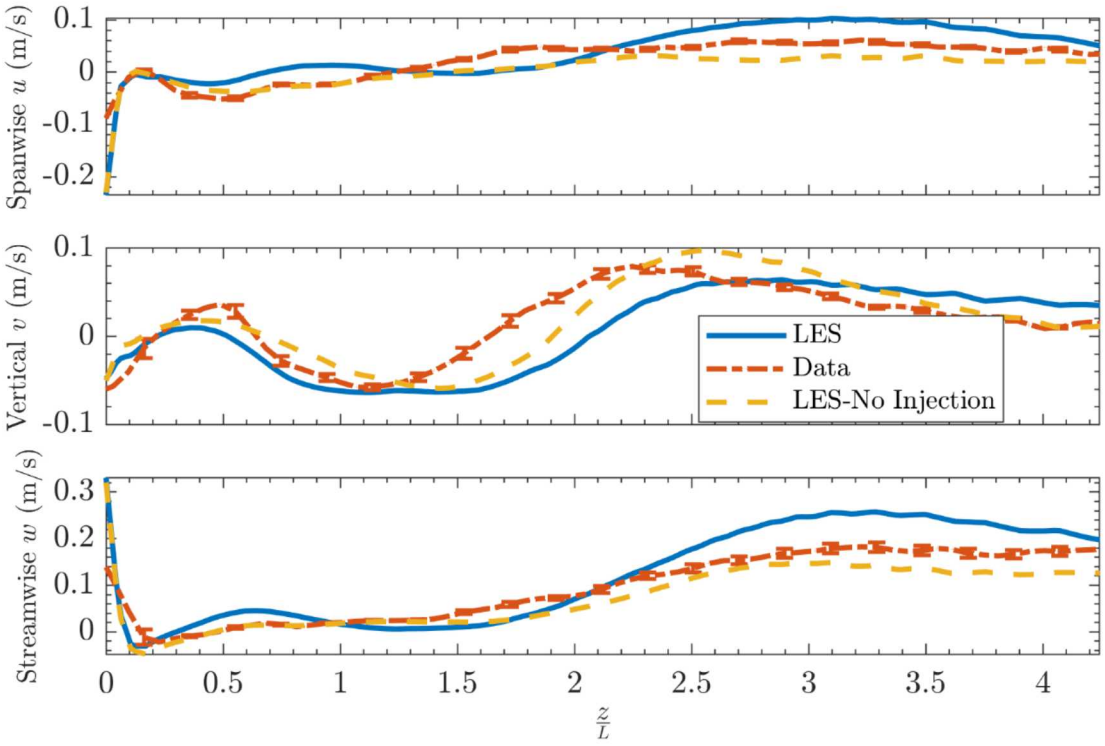

Figure 3-52. Velocity Components for the Baseline LES and No Injection LES Results Compared with Experimental Data for the Streamwise Line at 1/2 H

The No Injection results show a mix of greater and lesser accuracy for the streamwise line at 5/6 H as shown in Figure 3-53. This is likely due to the increasing vertical space for higher lines where the influence of no injection is expected to be lower.

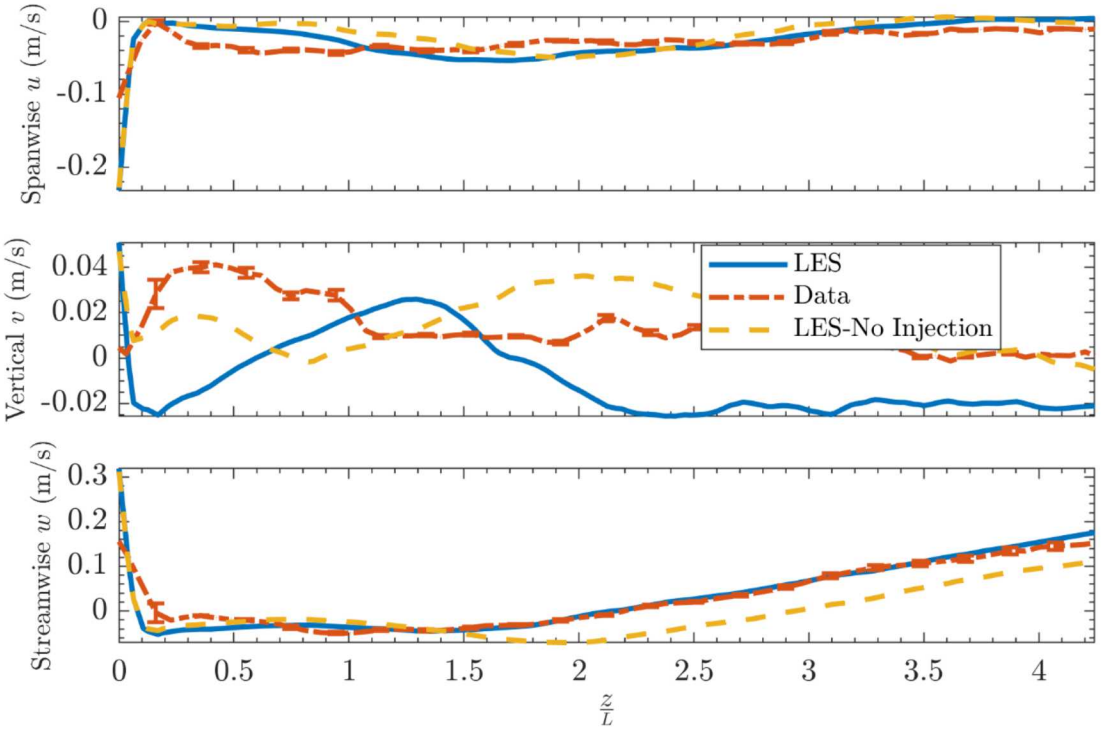

Figure 3-53. Velocity Components for the Baseline LES and No Injection LES Results Compared with Experimental Data for the Streamwise Line at 5/6 H

The near-ground spanwise results at 1/6 H show much greater accuracy in the area near the injection location that spans $-1 < \frac{x}{L} < 1$ as shown in Figure 3-54. Outside of this region, both LES results are practically identical. As expected, the vertical velocity is overly predicted in the baseline LES results as the momentum contribution of the injection velocity increases the local velocity by a difference near the injection velocity magnitude of 0.044 m/s. With the complex wake region structure, the baseline LES results also have an overpredicted velocity in the streamwise and spanwise directions.

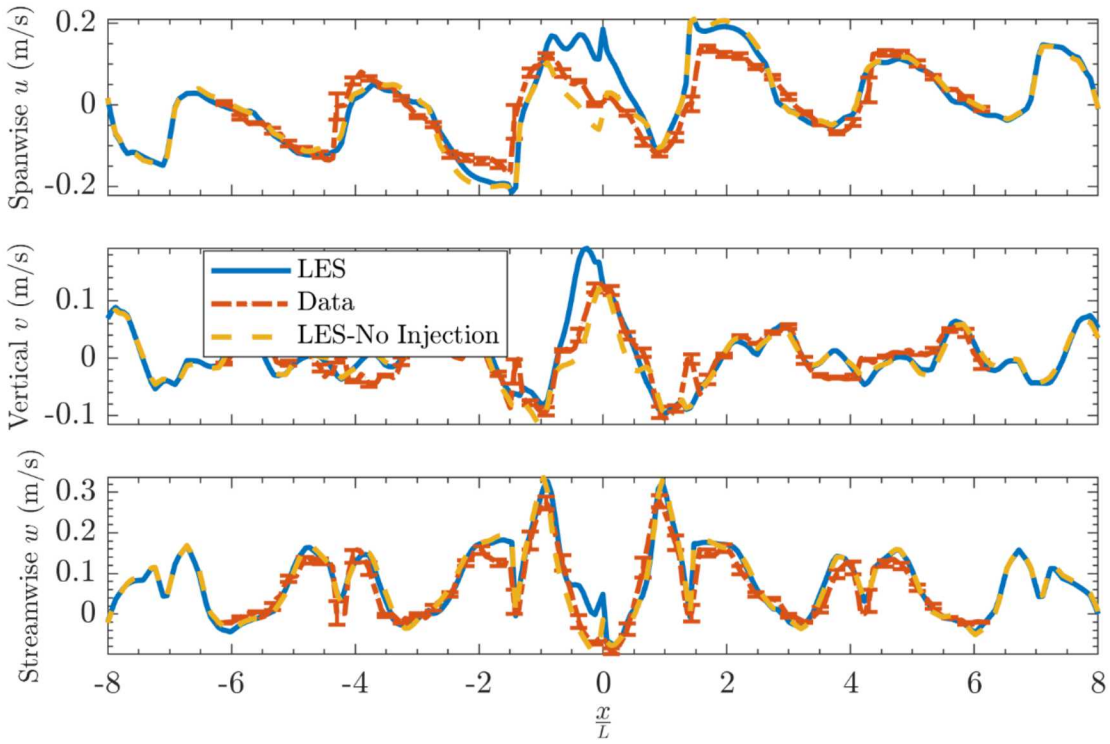

Figure 3-54. Velocity Components for the Baseline LES and No Injection LES Results Compared with Experimental Data for the Spanwise Line at 1/6 H

Excellent agreement is observed for the No Injection results near the injection site for the spanwise line at 1/2 H as shown in Figure 3-55. There is little deviation outside of the experimental uncertainty suggesting that the uncertainty bands have likely captured the errors in this region. Outside of this region, the two LES simulation results are very similar as before with some deviations between simulation results and experimental data.

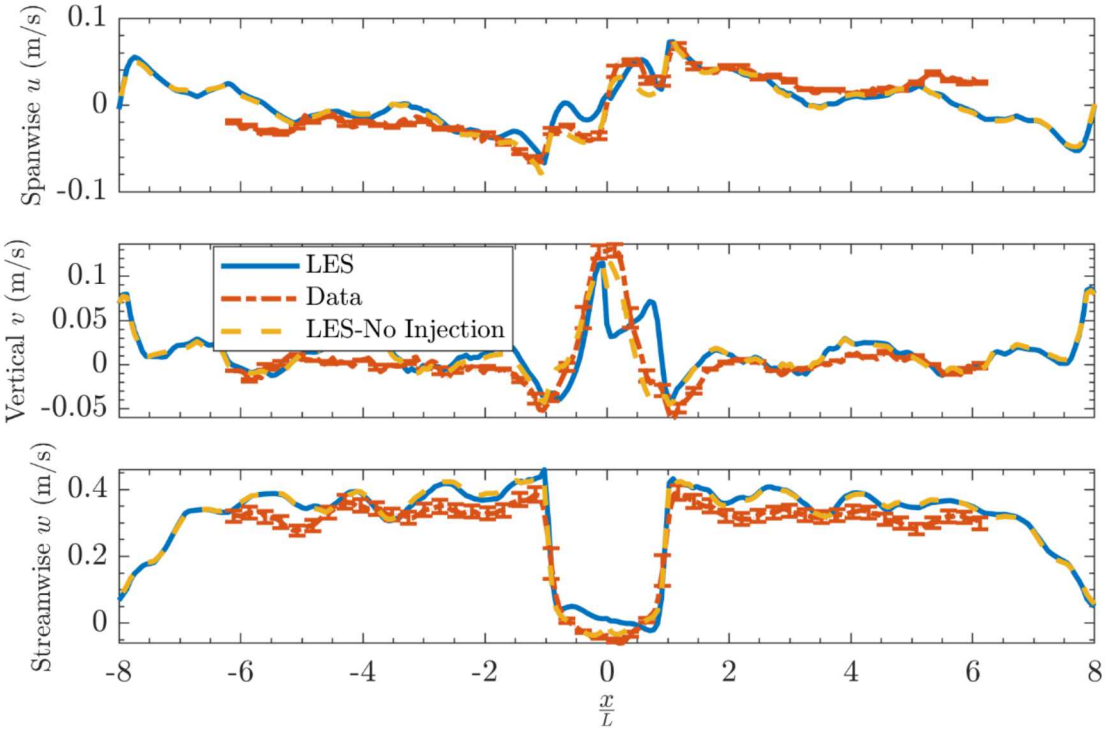

Figure 3-55. Velocity Components for the Baseline LES and No Injection LES Results Compared with Experimental Data for the Spanwise Line at 1/2 H

The No Injection results show improved accuracy, even at the higher 5/6 H line in the spanwise direction as shown in Figure 3-56. As before, the improvements are generally localized near the injection site. The vertical velocity component shows a much better trend in this area as the corrected boundary conditions propagate far into the domain in the tall building wake region.

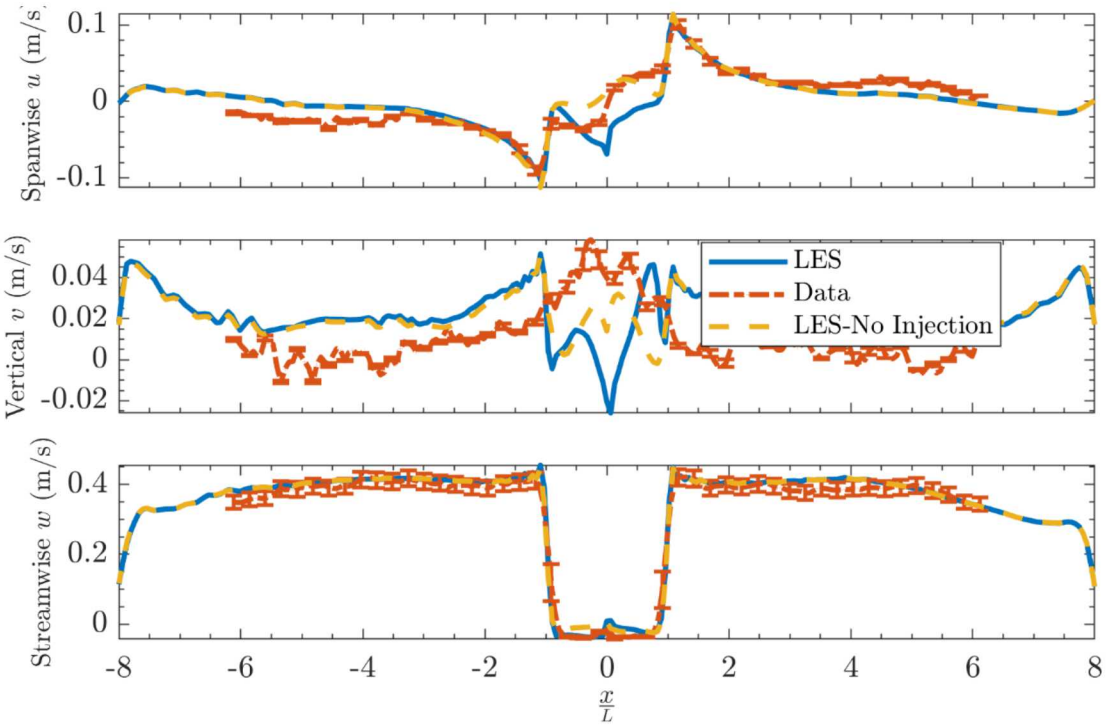

Figure 3-56. Velocity Components for the Baseline LES and No Injection LES Results Compared with Experimental Data for the Spanwise Line at 5/6 H

The No Injection velocity results above show improved velocity predictions in the area near the injection site that suggest greater prediction accuracy than shown in previous results with slightly inconsistent boundary conditions between the experiment and simulations. The simulations are expected to perform well when careful attention is paid to the application of boundary and initial conditions.

3.3. Point Comparisons

The plane and line comparisons do not represent the full richness of the output from the comparisons. Points in space were selected at which to track the dynamic species concentration and velocities. These points are the familiar 1/6H, 1/2H, 5/6H elevation locations at the 3-4 plane (in the z-direction) and at the E-F plane (in the x-direction). This locates the points directly above the center of the injector. Table 3-2 adds to what has already been presented at these locations in the line and plan output by showing the temporal mean and standard deviation from the simulations. Temporal mean is calculated consistently as was the data. Mean component velocities were determined, and then a mean vector magnitude constructed from the mean vector components (as opposed to mean magnitude at each timestep then averaged). The standard deviation is based on the mean magnitude from every timestep, and is smaller than if derived by taking the magnitude of a standard deviation vector from the components. The concentration is a simple mean of the temporal data. Fluctuation magnitudes are relatively high, with the standard deviation typically between a half and a third of the magnitude of the mean.

Table 3-2. Line Intersection Flow Statistics (Mean, μ, and Standard Deviation, σ) at the Three Selected Heights Based on 5-20 Second Predictions

Cases	Variable	5/6H		1/2H		1/6H	
		μ	σ	μ	σ	μ	σ
Baseline LES	V-mag (m/s	0.0564	0.0277	0.0935	0.0373	0.221	0.102
	Concentration	0.157	0.0669	0.326	0.134	0.193	0.0830
Data	V-mag (m/s)	0.0568		0.0396		0.179	
	Concentration	0.0557		0.170		0.154	

These results may differ slightly from the results in the prior section. These were extracted based on the closest node to the point of interest. Prior data were interpolated to the exact location of comparison. Spatial differences may be as much as half the characteristic length of a computational node.

This page left blank

4. DISCUSSION

4.1. Planar and 3D Comparisons

The richness of the dataset produced by the MRV/MRC technique allows for very detailed comparisons between the experiments and simulations. Simulations normally have high fidelity, and significant components of the simulation predictions are typically omitted from validation comparison exercises. This report omits significant amounts of both model and experimental results, and elects to focus on some characteristic of selected planes, lines, and points in the domain.

The planar comparisons are not particularly strong for validation compared to quantitative comparison methods, but give a helpful picture of the general similarity between model and experiment. Figure 3-1 through Figure 3-12 in general show good agreement between the data and model contours. It is through these figures that a general concept of the flow is obtained. As the contaminant enters the domain, it is dispersed by bulk flow. The pollutant is swept vertically upward and against the lee-ward side of the tall building. The low wake velocities do not necessarily correlate to high concentrations downstream of the large structure, as the pollutant disperses with increasing height. The vertical velocity caused by the presence of the tall building appears to be the driving force for the significant vertical dispersion of the contaminant. The tall building acts as a barrier to the full stream flow and prevents the contaminant plume from being immediately swept downwind. The highest concentration is most notably present closest to the injection site and within the street canyon, closer to the tall building.

The plots that show the simulation dynamics illustrate the turbulent nature of the baseline prediction. The instantaneous clips and planar output of vorticity and q-criterion suggest significant turbulent structure to the flow in the wakes of the buildings. Iso-contours of the concentration suggest a significant variation in the instantaneous position of the plume. Comparisons are performed to the average results. Average results may include significant frequency of zero concentration because of the fluctuations. This is probably a pronounced effect near the fringes of the concentration iso-contours at low concentration levels.

The 3D comparison analysis was enlightening. The predicted concentrations were generally lower than the data while the linearity was good, suggesting a calibration issue with the tests or an injection issue with the model or tests. We have examined the fit by applying a uniform bias to the experimental results to produce an improved linear (slope = 1.0) fit to the simulations. This greatly improves the quality of the concentration comparison. These results are not shown here. The velocity comparisons were lacking between the baseline scenario and the data. Part of the cause of this was known, and these results illustrate the effect of a boundary condition error on the magnitude of the validation accuracy. Together with the simulation results for the no-injection case that better represent the conditions at which the velocity data were taken, a magnitude of effect and qualitative observations suggest how such an error influences the quantitative accuracy. The 'tear-drop' shape when found in comparison results in the future will be suggestive of a systemic error in the data comparison as was the case in this activity. Comparisons that have been examined thus far have more typically produced a cloud of point comparisons centered around the ideal line with a slope of 1 and intercept of 0. The degree to which they deviate from this suggests a localized deviation or an offset of some kind, either an alignment offset, a faulty boundary condition, or localized variations caused by regional differences between model and data.

The magnitude comparisons provide further discussion regarding the accuracy of the model compared to the data. The concentration results were not particularly accurate, with LND of 0.456 and FAC2 of 0.483. These improve greatly if the bias is eliminated from the comparison by linearly adjusting the scale. We purposefully avoid showing these results because the study was originally intended to be a blind validation comparison in which case the adjustment thwarts the basis for showing a true measure of success. In this respect, this activity failed as a validation study, and this serves as a cautionary narrative. Future comparisons should endeavor to more carefully check the adequacy of the inputs and calibrations to help mitigate this issue.

The velocity baseline case also did not compare particularly well with the data. This was pre-advised to be a potential issue, as the test team purposefully took the velocity data without an active injection. There is good information in this non-ideal situation for validation. The quantitative outputs suggest the magnitude of impact these parameters have on the quality of comparisons, and help benchmark the difference between a desirable comparison (with correct conditions) and an undesirable comparison (where conditions vary). The magnitude change in the metric parameters sometimes do not show a significant change as the test and model are brought into better agreement.

Many of the metric parameters were taken from HC-2012 and applied out of context for their study. Extending the parameters to the velocity magnitude is probably a reasonable activity, since the metrics seem agnostic to the nature of the source variables. Using the same success thresholds might not be as reasonable. A major difference between velocity and concentration is that the velocity will tend to vary within a narrower range of parameters. Concentrations can change by several orders of magnitude in the far-field. The way the metrics are used to assess the velocity adequacy may be what needs to be adjusted for future comparisons. The present concentration measurement technique is not sufficiently sensitive to measure trace species concentrations, a shortcoming that could use improvement. Because concentration did not vary as much as in HC-2012, it is probably not reasonable to make a 1:1 comparison with their metrics for concentration either. Their metrics were designed for plume transport models that lack the fidelity of CFD. This is part of the reason we find our CFD results to uniformly pass the acceptance criteria for urban scenarios proposed by HC-2012, even when a simple analysis suggests the calibration is off by nearly 50% on concentration or we know that the velocity injection is modeled incorrectly. Because CFD is more computationally intensive and presumably (as a consequence) more accurate, it seems reasonable to suggest the need for development of comparable success metrics for CFD comparisons instead of relying on the prior work that is of questionable contextual similarity. Such development activity will probably require a suite of results and comparisons to achieve a quantitative understanding of when results are good and when they indicate that there are substantive differences between model and data.

4.2. Line Comparisons

Line plots more readily show the quantitative quality of the comparison between model and test data by including additional sources of uncertainty from both simulation and experiment. Figure 3-23 shows the full set of 17 simulation results with experimental data to provide a sense of the information that went into the analysis. The grid convergence study results as shown in Figure 3-24 did not provide a clear estimate of the uncertainty of the prediction from the grid due to the compounding effects of the changing LES model length filter with the grid. On the other hand, the simulation results from three levels of mesh refinement in Figure 3-25 through Figure 3-31 provide a qualitative understanding of how the mesh impacted results. In general there was observed a large difference between Coarse and Medium due to the large relative refinement of 3x. The Medium and

Fine results were much more consistent with the relative refinement of 1.33x and provide a level of confidence that the predictions are not largely sensitive to the mesh at this point.

The results for the input parameter study in section 3.2.2 reveal the influence of the model inputs on the concentration and velocity results. These results both quantify the total parameter uncertainty and identify large contributors to this uncertainty that may be reduced to most effectively reduce total uncertainty. In general, the three most impactful parameters are TKE, inlet velocity, and injection velocity with similar magnitudes of effect. The fourth is temperature and the Schmidt number is clearly the lowest. A more rigorous analysis of the relative importance of these parameters can be performed using Importance Factor methods of AMSE V&V-20, Nonmandatory Appendix B that quantify the fractional contribution of each parameter to the total parameter uncertainty (ASME, 2009). This analysis would require spatial averaging of importance factors but would be a step toward quantifying scalar results that would aid in credibility assessment and guide efforts in reducing input parameter uncertainty.

The complete line results in section 3.2.3 include the baseline LES with parameter uncertainty estimates, experimental data with uncertainty estimates from concentration and velocity directly as well as the influence of spatial uncertainty, and the TFNS and $k-\epsilon$ model results for comparison. The concentration predictions were almost exclusively higher than that measured, with overpredictions often a factor of ~1.5-2x. This nearly systematic difference could be investigated further to identify the error, whether it be experimental or computational or a combination of both, to improve confidence in the predictive capability of concentration. Some possible areas of investigation could be experimental concentration scaling or computational dispersion augmentation. Between the three models tested for concentration, the most accurate appears to be the TFNS followed by $k-\epsilon$ with LES least accurate. This observation is consistent with that from the 90 degree study performed previously and suggests that there could be a systematic error because the higher fidelity LES should have better predictive accuracy that the $k-\epsilon$ RANS model. In contrast to concentration, the velocity predictions are much more accurate with many instances of overlapping uncertainty bands with experimental data. The differences tend to be larger in the complex wake and street canyon areas compared to the free-stream where predictions are nearly perfect. The LES and TFNS velocity results are very similar and show greater accuracy than the $k-\epsilon$ model as expected. In both the concentration and velocity predictions, the parameter uncertainty is relatively small and likely underestimating the simulation uncertainty. Future work may include grid convergence uncertainty with cutting-edge methods, likely increasing the total uncertainty by a noticeable amount.

The No Injection velocity results in section 3.2.4 have a corrected boundary condition and show even greater velocity predictive accuracy than shown previously with the un-corrected simulation results. The velocity components in the vertical, streamwise, and spanwise directions were investigated to observe the lowest level influence of the corrected boundary condition. In general the results show improvement near the injection site as expected with a smaller impact elsewhere. A distinct example of the improvement is shown in the vertical velocity in Figure 3-51 where the peak near $z=0$ is correctly removed. The vertical velocity is also improved in oPoither areas of the domain. The spanwise line results in Figure 3-54 through Figure 3-56 show very noticeable improvements near $x=0$.

4.3. Point Comparisons

A more thorough analysis was done on the point data for the 90° scenario. The point data were analyzed just for the data and the baseline LES case for the three intersection points. Considerably more output from the simulation campaign exists, the analysis of which is left to future work.

Here we report averages and standard deviations from 5-20 seconds of the simulation run on just the baseline case. These are compared to the data. The point data were key to this study because they served as a check on the accuracy of the line data. After producing and plotting the point data, they were verified back against the line data. Differences were identified, which were discovered to be related to a spatial location error for the vertical line. This was corrected, greatly improving the quality of this report. This is a key value associated with the activity of identifying and comparing selected point results.

Another finding from the point results is that the fluctuations as identified by the standard deviation of the predictions tended to be highest for the velocity at the lowest (1/6H) height. The mid-height (1/2H) had the highest standard deviation for the concentration, but the standard deviation was largest relative to the mean at the lowest height. This implies that the variability is highest at the lower levels, but the peak in fluctuation intensity is higher.

Point concentration data suggest what the line and 3D analysis have been suggesting, which is that the concentrations from the data are generally lower than the model predictions. They also suggest that this flow is in a turbulent regime with high fluctuation magnitudes that meets the objective of characterizing the accuracy of simulation tools in a turbulent regime.

4.4. General Discussion

A recurring theme in this report thus far is the generally lower experimental concentration results compared to the simulation results. This offset is likely the main source for error and poor comparison metrics for the various comparison methods. There are likely one of several issues at play. First, the experiments scale the concentration to a calibrated maximum. It is possible that the method used to perform this scaling was off by nearly a factor of 2. Second, there could be an error in the injector. Either the tests did not result in the magnitude of injection reported, or the simulation might mis-represent the injection. The latter is unlikely since the input files were basically copied from the 90 degree scenario and better comparisons were found in that case. Third, there could be a significant issue with the model behavior in this scenario. This would need to be particular to this scenario, as the 90 degree simulations were much better. We are presently inclined to the first issue, but look for concurrence from the testing team. If this is the case, it is appropriate to bulk-scale the concentrations for future comparisons to improve the fit. This was a semi-blind comparison, so we feel obligated to report the issues as they occur instead of adjusting the model before reporting the results.

There was also a recurring theme relating to the velocity comparisons. This MRC/MRV dataset lacks uniformity between the test results for the concentration and velocity. This was reported by the test team prior to comparisons, so the potential issue was not identified in the comparison process. As such, it seemed appropriate to make comparisons to the baseline delivered data, but also illustrate the simulations corrected to the flow measurement conditions. This improved the quality of the comparison between model and data, and also has value in that it provides a scale magnitude of the effect of the change on the outcome of the simulations. An interesting notion that is suggested by the comparisons is that the differences tend to be local near the point of disagreement. The far-field appears less affected. This is probably due to the increased importance

of diffusional processes further downstream. The various methods of comparing velocity magnitude all show good comparisons, suggesting a strong similarity between experiments and simulations. It is not clear what to do about the degree to which they did not compare well, a detail that could be subject of subsequent efforts. Only minimal exposure of the fine mesh simulation was shown in this work. More could be done this way to potentially improve the understanding of the reason for local disagreement.

This is a subsequent activity to the 90 degree work documented previously. This work mostly shows additional maturity. The 3D analysis was not done for the 90 degree work, and is in-progress as a post-report analysis. This is a major improvement, and makes progress towards realizing the potential of the experimental technique in relation to model validation. Additional planar and volume images were extracted detailing more information about the predictions. The line comparisons were generally more detailed. We introduced a more systematic and quantitative method to assess the accuracy bounds and the convergence. The convergence work was hampered by the techniques not being consistent with the model methods and the irregular mesh selection that was consistent with the 90 degree work but less ideal for mesh convergence analysis. There was an increased parametric study relating to the model uncertainty parameters. This is helpful because it identifies the prime factors potentially contributing to model uncertainty. The point comparison was less detailed in this study.

Significant value is found in the 2D and 3D comparisons. The 2D comparisons do not provide quantitative output, but are very helpful at orienting and interpreting the results of the study. The 3D comparisons have a significant potential to provide perhaps the best quantification of model accuracy. This report describes some methods that we had to develop independently of the historical literature to make quantitative assessments of accuracy. There is opportunity to improve on these techniques that will require effort to formulate and test concepts to be able to best tap the potential of these data. The 1D line plot techniques continue to be important abstractions. While they lack the fidelity of the 2D and 3D comparisons, they are more amenable to reporting and representation of the results in print. Uncertainties on a 1D plot can be illustrated in 2D. Doing the same for 2D results requires 3D representation, and so on. How to perform and illustrate the output of a validation study including all the uncertainties as in this case is not a field with mature methods.

It wasn't just the point analysis that was under-represented in this final report. There are a lot of activities with significant value that could have been done with these comparisons that will not be completed for this report. These may be topics of subsequent studies. Specifically, the 3D data were only compared to the baseline scenario. There was no verification that the alignment between data and model were optimal. We have been doing correlation analysis between model and data as a 3D metric of accuracy. Gradient analysis is a component of some of the 3D assessments in progress for the other scenarios. None of these are in this report. The mesh and parameter study results are not brought into the 3D assessment. Line comparisons could do more with variable gradients, vector component assessments, and spatial uncertainties. TFNS model predictions appear to be most accurate of the three models used as observed in the qualitative line comparisons, but quantitative accuracy assessment is more actionable than the more qualitative comparisons presented herein. The program seems to be trending more towards a breadth of scenarios rather than towards depth of analysis. These opportunities may be leveraged at a future time, as the data and simulation results are retained for subsequent analysis.

A point that is never resolved in this work is whether the simulations are valid based on these predictions and comparisons with the data. This is a philosophical question, and can be turned

around to put the onus on the end application to define what constitutes a valid result. Either way, there is a need to have a clearer outcome of a validation study such as this. The validation process involves data and model comparisons, but is not of itself the validation. A validation study should result in a defensible argument regarding the accuracy of a simulation tool. Validation should enable acceptance or rejection of simulations based on the outcome of the study. Despite successful application of some well accepted methods, this work remains philosophically incomplete since the outcome of the effort does not conclude with a statement of validity. This omission is not uncommon in validation efforts, as the final step is often left to inference. The positive side of the argument is to note that this work makes good progress towards a more conclusive ideal by benchmarking the magnitudes and metrics of accuracy for comparison with prior and future studies of similar nature. This remains one of the big questions relating to use of complex engineering simulation tools, and will likely be a topic of research for years to come.

We have exposed in this report some testing and modeling limitations that should be listed, as they may represent productive follow-on work. Inclusion in this list does not necessarily mean that we have a solution or solution method, just that there is opportunity.

- The concentration measurements were unreliable below 0.025, which is not nearly as low as the atmospheric plume community prefers to study.
- As with the 90 degree simulation, we remain uncertain about the adequacy of the 2D inflow condition lacking temporal input for a turbulent flow. We also are concerned with the secondary injection that involved a perforated plate. These can be difficult to model.
- The experimental data near the surfaces were contaminated by the objects, which makes near surface data suspect and comparisons near surfaces questionable. Methods are needed to improve or better manage or mitigate these effects.
- Experiments with current MRIs are scale and fluid limited. This limits the Reynolds number regime and also the application of the results to regimes enabled by the methods. There is value in considering some feasible extrapolations of this work to broaden the applicability of the data.
- Validation and comparison methodologies are lacking in maturity to leverage the full potential of these datasets. Some development activities to enable better processes would be beneficial.
- Plumes often have buoyant components, or involve thermal effects or chemical reactions.
- The notional geometry tested was idealized. What happens when the complexity of a more applied scenario is introduced?
- Not all releases of interest are continuous in nature. The MRC/MRV plume datasets thus far only exist for continuous releases.
- The adequacy of the spatial alignment between the data and simulation was not verified.
- The planes, lines, and points selected for comparison were done so haphazardly given the information potential in the data. A data-driven selection method might be more revealing.
- Simulation results were under-utilized. Some of the analysis methods could be better automated to enable richer comparisons.

- The data include gradient information, which can be harnessed for a more insightful analysis of the comparisons.
- The temporal information provided by the simulation tools augments the understanding of the scenario. While no similar data exist, the knowledge obtained from the simulations can be leveraged for validation methods.
- Spatial accuracy relating to the concentration and velocity information is available in the comparisons. Employing methods to take advantage of this could aid in identification of regions of interest or methods for identifying techniques to define regions for spatial refinement or model assessment.
- The joint accuracy of the velocity and concentration from tests like this has rich potential for validation by including both parameters. This dataset is not the right one exploring this potential opportunity, although the data techniques and simulation tools present a good approach to this activity.

This page left blank

5. CONCLUSIONS

A series of computational simulations has been performed for dispersion of a contaminant in a geometry inspired by atmospheric conditions of interest. The simulations are compared with 3-D water channel flow measurements using the MRV/MRC technique. A parameter study involving turbulence models as well as a variety of convergence and parametric variations is used to assess model uncertainty. The models and experiments compare reasonably well, although this scenario indicates a linear bias between simulated and experimental concentrations. Key to the velocity comparisons was simulating the correct test conditions, which differed from those of the concentration release. The difference helps identify the quantitative magnitude of error associated with boundary condition errors. The MRV/MRC dataset represents an unusually detailed opportunity to assess model and experimental uncertainty for a problem of practical interest. Additional V&V methods work is needed to improve the quality of the comparisons and the utility of the findings from this type of flow.

REFERENCES

Addepalli, B. and Pardyjak, E.R., 2015. A Study of Flow Fields in Step-Down Street Canyons. *Environmental Fluid Mechanics*, *15*(2), pp.439-481.

ASME, 2009. ASME V&V 20-2009: Standard for Verification and Validation in Scientific Computing.

Benson, M.J., Elkins, C.J. and Eaton, J.K., 2011. Measurements of 3D Velocity and Scalar Field for a Film-Cooled Airfoil Trailing Edge. *Experiments in Fluids*, *51*(2), pp.443-455.

Brixey, L.A., Heist, D.K., Richmond-Bryant, J., Bowker, G.E., Perry, S.G. and Wiener, R.W., 2009. The Effect of a Tall Tower on Flow and Dispersion through a Model Urban Neighborhood Part 2. Pollutant Dispersion. *Journal of Environmental Monitoring*, *11*(12), pp.2171-2179.

Brown, A.L. and Dabberdt, W.F., 2003. Modeling Ventilation and Dispersion for Covered Roadways. *Journal of Wind Engineering and Industrial Aerodynamics*, *91*(5), pp.593-608.

Brown, Clemenson, Benson, Elkins, Jones, 3D Analysis of Concentration and Flow using the MRC/MRV 90 Degree Flow Data and CFD Predictions from SIERRA/Fuego, Extended Abstract Accepted to the PRTEC 2019 Meeting, December 13-17, 2019.

Bunge, U., Mockett, F.T., Kok, J.C., van der Ven, H., Knopp, T., and Weinman, K., 2005. A Grid Convergence Study for DES-like Simulations of a Stalled Airfoil.

Carnes, B. and Kennon, S.R., 2016. *Percept User Manual* (No. SAND2016-10177). Sandia National Laboratories (SNL-NM), Albuquerque, NM (United States).

Chang, S., Elkins, C., Alley, M., Eaton, J. and Monismitha, S., 2009. Flow Inside a Coral Colony Measured using Magnetic Resonance Velocimetry. *Limnology and Oceanography*, *54*(5), pp.1819-1827.

Chapra, S.C. and Canale, R.P., 2010. *Numerical Methods for Engineers*. Boston, McGraw-Hill Higher Education.

Elkins, C.J. and Alley, M.T., 2007. Magnetic Resonance Velocimetry: Applications of Magnetic Resonance Imaging in the Measurement of Fluid Motion. *Experiments in Fluids*, 43(6), pp.823-858.

Elkins, C.J., Alley, M.T., Saetran, L. and Eaton, J.K., 2009. Three-Dimensional Magnetic Resonance Velocimetry Measurements of Turbulence Quantities in Complex Flow. *Experiments in Fluids*, 46(2), pp.285-296.

Elkins, C.J., Markl, M., Iyengar, A., Wicker, R. and Eaton, J.K., 2004. Full-Field Velocity and Temperature Measurements using Magnetic Resonance Imaging in Turbulent Complex Internal Flows. International *Journal of Heat and Fluid Flow*, 25(5), pp.702-710.

Elkins, C.J., Markl, M., Pelc, N. and Eaton, J.K., 2003. 4D Magnetic Resonance Velocimetry for Mean Velocity Measurements in Complex Turbulent Flows. *Experiments in Fluids*, 34(4), pp.494-503.

Franzese, P. and Huq, P., 2011. Urban Dispersion Modelling and Experiments in the Daytime and Nighttime Atmosphere. *Boundary-Layer Meteorology*, *139*(3), pp.395-409.

Hayati, A.N., Stoll, R., Kim, J.J., Harman, T., Nelson, M.A., Brown, M.J. and Pardyjak, E.R., 2017. Comprehensive Evaluation of Fast-Response, Reynolds-Averaged Navier–Stokes, and Large-Eddy Simulation Methods Against High-Spatial-Resolution Wind-Tunnel Data in Step-Down Street Canyons. *Boundary-Layer Meteorology*, *164*(2), pp.217-247.

Heist, D.K., Brixey, L.A., Richmond-Bryant, J., Bowker, G.E., Perry, S.G. and Wiener, R.W., 2009. The Effect of a Tall Tower on Flow and Dispersion through a Model Urban Neighborhood Part 1. Flow Characteristics. *Journal of Environmental Monitoring*, *11*(12), pp.2163-2170.

Jones, W.P. and Launder, B., 1972. The Prediction of Laminarization with a Two-Equation Model of Turbulence. *International Journal of Heat and Mass Transfer*, *15*(2), pp.301-314.

Kim, W.W., Menon, S., Kim, W.W. and Menon, S., 1997, January. Application of the Localized Dynamic Subgrid-Scale Model to Turbulent Wall-Bounded Flows. In *35th Aerospace Sciences Meeting and Exhibit* (p. 210).

Laskowski, G.M., Kearney, S.P., Evans, G. and Greif, R., 2007. Mixed Convection Heat Transfer to-and-from a Horizontal Cylinder in Cross-Flow with Heating from Below. *International Journal of Heat and Fluid Flow*, *28*(3), pp.454-468

Lateb, M., Meroney, R.N., Yataghene, M., Fellouah, H., Saleh, F. and Boufadel, M.C., 2016. On the Use of Numerical Modelling for Near-Field Pollutant Dispersion in Urban Environments− A Review. *Environmental Pollution*, *208*, pp.271-283.

Launder, B.E. and Spalding, D.B., 1983. The Numerical Computation of Turbulent Flows. In *Numerical Prediction of Flow, Heat Transfer, Turbulence and Combustion* (pp. 96-116).

Meier, W., Barlow, R.S., Chen, Y.L. and Chen, J.Y., 2000. Raman/Rayleigh/LIF Measurements in a Turbulent CH4/H2/N2 Jet Diffusion Flame: Experimental Techniques and Turbulence–Chemistry Interaction. Combustion and Flame, 123(3), pp.326-343.

Oberkampf, W.L. and Roy, C.J., 2010. Verification and Validation in Scientific Computing. Cambridge University Press.

Pascheke, F., Barlow, J.F. and Robins, A., 2008. Wind-Tunnel Modelling of Dispersion from a Scalar Area Source in Urban-Like Roughness. *Boundary-Layer Meteorology*, *126*(1), pp.103-124.

Saathoff, P., Gupta, A., Stathopoulos, T. and Lazure, L., 2009. Contamination of Fresh Air Intakes Due to Downwash from a Rooftop Structure. *Journal of the Air & Waste Management Association*, *59*(3), pp.343-353.

Shen, J., Gao, Z., Ding, W. and Yu, Y., 2017. An Investigation on the Effect of Street Morphology to Ambient Air Quality using Six Real-World Cases. *Atmospheric Environment*, *164*, pp.85-101.

Shim, G., Prasad, D., Elkins, C.J., Eaton, J.K. and Benson, M.J., 2019. 3D MRI Measurements of the Effects of Wind Direction on Flow Characteristics and Contaminant Dispersion in a Model Urban Canopy. *Environmental Fluid Mechanics*, *19*(4), pp.851-878.

Sierra Thermal Fluids Development Team, "Sierra Low Mach Module: Fuego Theory Manual – Version 4.44," Sandia National Laboratories, SAND 2017-3774, (2017a).

Sierra Thermal Fluids Development Team, "Sierra Low Mach Module: Fuego User Manual – Version 4.44," Sandia National Laboratories, SAND 2017-3792, (2017b).

Tieszen, S.R., Domino, S.P. and Black, A.R., 2005. *Validation of a Simple Turbulence Model Suitable for Closure of Temporally-Filtered Navier-Stokes Equations using a Helium Plume* (No. SAND2005-3210). Sandia National Laboratories.

Van Leer, B., 1979. Towards the Ultimate Conservative Difference Scheme. V. A Second-Order Sequel to Godunov's Method. *Journal of Computational Physics*, *32*(1), pp.101-136.

Xie, Z.T., Coceal, O. and Castro, I.P., 2008. Large-Eddy Simulation of Flows Over Random Urban-Like Obstacles. *Boundary-Layer Meteorology*, *129*(1), p.1.

APPENDIX A. THE BASELINE LES INPUT FILES

```
#<Problem_Description>
#
# Flow around a building array
# 3D, time-dependent
# LES turbulence model
#
# </Problem_Description>

Begin Sierra Fuego

    Title Flow Around Building Array

$-------------------------------------------------
$   Specify mesh name and settings
$-------------------------------------------------
    Begin Finite Element Model Water_flow
        Database Name = ../meshes/Medium45.g
        Database Type = ExodusII

$-------------------------------------------------
$       Assign material properties to element blocks
$-------------------------------------------------
        Begin Parameters For Block block_1
            Material Water
        End   Parameters For Block block_1
    End   Finite Element Model Water_flow

   BEGIN FINITE ELEMENT MODEL output_plane
        Database Name = ../meshes/inflow_moved1.e
        Database Type = EXODUSII

$        BEGIN PARAMETERS FOR BLOCK block_1
$            MATERIAL gas
$        END   PARAMETERS FOR BLOCK block_1
    END   FINITE ELEMENT MODEL output_plane


   BEGIN FINITE ELEMENT MODEL output_plane1
        Database Name = ../meshes/InflowBC1.e
        Database Type = EXODUSII

        BEGIN PARAMETERS FOR BLOCK block_1
            MATERIAL gas
        END   PARAMETERS FOR BLOCK block_1
    END   FINITE ELEMENT MODEL output_plane1


$-------------------------------------------------
$   Define material properties to be used
$-------------------------------------------------
    Begin Property Specification For Fuego Material Water
        Specific_heat                    = 4.18e07
        Reference Temperature            = 294.15 $k
        density                          = 997.97       $ kg/m^3
        viscosity                        = 0.00098        $ Pa*s
        REFERENCE mixture_fraction       = 0.0
        SCHMIDT_NUMBER                   = 0.9
        PRANDTL_NUMBER                   = 0.9

    End   Property Specification For Fuego Material Water

$-------------------------------------------------
$   Define global constants
$-------------------------------------------------

  Begin Global Constants turb
    Turbulence Model Prandtl Number = 0.9
    Turbulence Model Schmidt Number = 0.9
```

```
    GRAVITY VECTOR = 0.0, -9.80665, 0  #mks units
  END   Global Constants turb

$-------------------------------------------------
$   Define velocity functions
$-------------------------------------------------


 BEGIN DEFINITION FOR FUNCTION gasVolFcn
    TYPE IS PIECEWISE LINEAR
    BEGIN VALUES

         0.0   1.0
         0.095 1.0
         0.096 0.9
         0.105 0.9
         0.106 1.0
         0.107 1.0

    END VALUES
  END DEFINITION FOR FUNCTION gasVolFcn


$-------------------------------------------------
$   Define linear solver settings
$-------------------------------------------------
    Begin Trilinos Equation Solver Continuity
        Solution Method = GMRES
        Preconditioning Method = Multilevel
        Restart Iterations = 100
        Maximum Iterations = 100
        Residual Norm Tolerance = 1.0e-5
        Residual Norm Scaling = R0
    End   Trilinos Equation Solver Continuity

    Begin Aztec Equation Solver Scalar
        Solution Method = GMRES
        Preconditioning Method = Symmetric-gauss-seidel
        Preconditioning Steps = 1
        Restart Iterations = 50
        Maximum Iterations = 50
        Residual Norm Tolerance = 1.0e-4
        Residual Norm Scaling = R0
    End   Aztec Equation Solver Scalar


$  RESTART = automatic

$-------------------------------------------------------
$   Procedure domain - solution control, region settings
$-------------------------------------------------------

    Begin Fuego Procedure Fuego_procedure

$-------------------------------------------------
$       Define temporal solution parameters
$-------------------------------------------------
        Time Start = 0.0, Stop = 20.0, Status Interval = 10

        Begin Solution Control Description
            Use System Main

            begin initialize mytransient_init
$                 advance Fuego_region

$                 transfer average_to_fluid
$                    transfer average_to_fluid
$                 transfer average_to_average
                  advance average_refgion
                  advance average_region1
                     Advance Fuego_region
```

```
            end   initialize mytransient_init

            Begin System Main
                 use initialize mytransient_init

                Begin transient mytransient
$                 advance average_refgion
                    transfer average_to_fluid
                    Advance Fuego_region
                 advance average_region1
                 advance average_refgion
                End   transient mytransient

            End   System Main

$-------------------------------------------------
$           Define time integration parameters
$-------------------------------------------------
            Begin Parameters For transient mytransient
                Start Time  = 0.0
                Initial deltat = 0.0005
$                Initial deltat = 1.5e-3
                Termination Time Is 20.00

                Begin Parameters for Fuego Region Fuego_region
$                    Transient Step Type is Automatic
                   transient step type is fixed
$                  CFL Limit = 1.0
$                    Time Step Change Factor = 1.5
                End   Parameters for Fuego Region Fuego_region
            End   Parameters For transient mytransient

        End   Solution Control Description

$-------------------------------------------------
$          Transfers
$-------------------------------------------------
$        begin transfer average_to_average
$            interpolate surface nodes from average_refgion to average_region1
$            send block block_1 to block_1
$           send field ru state none to ru state none
$           send field rv state none to rv state none
$           send field z_velocitya state none to rw state none
$$           send field tke state none to tke_bc state none
$
$            SEARCH SURFACE GAP TOLERANCE = 0.1
$        end transfer  average_to_average

        begin transfer average_to_fluid
            interpolate surface nodes from average_refgion to Fuego_region
           send block surface_1 to surface_3
           send field x_velocitya state none to x_velocitya state none
           send field y_velocitya state none to y_velocitya state none
           send field z_velocitya state none to z_velocitya state none
$           send field tke state none to tke_bc state none
$
$            SEARCH SURFACE GAP TOLERANCE = 0.1
        end transfer  average_to_fluid

$     begin transfer shell_to_fluids_x
$       interpolate surface nodes from average_refgion to Fuego_region
$       send block surface_1 to block_1
$$       send field x_velocity_bc state none to x_velocity_bc state none
$$       send field y_velocity_bc state none to y_velocity_bc state none
$$       send field z_velocity_bc state none to z_velocity_bc state none
$       SEARCH SURFACE GAP TOLERANCE = 0.1
$     end


$-------------------------------------------------
```

```
$       Region domain - EQs, BCs, ICs, post-processing
$-----------------------------------------------

        Begin Fuego Region Fuego_region

$-----------------------------------------------
$   Define Unit Conversions
$-----------------------------------------------
       SET LENGTH UNIT CONVERSION FACTOR = 100.0  $ meters rather than cm
       SET MASS   UNIT CONVERSION FACTOR = 1000.0 $ kg rather than g
       SET TIME   UNIT CONVERSION FACTOR = 1.0    $ seconds - keep
       SET TEMPERATURE UNITS = Kelvin             $ Default

$-------------------------------------------------------
$           Specify solution steering options
$-------------------------------------------------------
$            Use Solution Steering With Interval = 4

$-------------------------------------------------------
$           Solution options - equations, solver options
$-------------------------------------------------------
            Begin Solution Options

$-------------------------------------------------
$               Specify coordinate system
$-------------------------------------------------
               Coordinate System = 3D

$-------------------------------------------------
$               Specify equations to solve
$-------------------------------------------------
               Activate Equation Continuity
               Activate Equation X_momentum
               Activate Equation Y_momentum
               Activate Equation Z_momentum
               Activate Equation Mixture_Fraction
               Activate Equation Turbulent_Kinetic_Energy

               Use Equation Solver Continuity For Equation Continuity
               Use Equation Solver Scalar     For Equation X_momentum
               Use Equation Solver Scalar     For Equation Y_momentum
               Use Equation Solver Scalar     For Equation Z_momentum
               Use Equation Solver Scalar     For Equation Mixture_Fraction
               Use Equation Solver Scalar     For Equation Turbulent_Kinetic_Energy

$-------------------------------------------------
$               Define nonlinear solver parameters
$-------------------------------------------------
               Minimum Number Of Nonlinear Iterations = 1
               Maximum Number Of Nonlinear Iterations = 1

$-------------------------------------------------
$               Specify pressure smoothing
$-------------------------------------------------
               Projection Method = Fourth_order Smoothing With Timestep Scaling

$-------------------------------------------------
$               Specify upwinding parameters
$-------------------------------------------------
               Upwind Method Is Upw   For Equation X_momentum
               Upwind Method Is Upw   For Equation Y_momentum
               Upwind Method Is Upw   For Equation Z_momentum
               Upwind Method Is Upw   For Equation Mixture_Fraction
               Upwind Method Is Upw   For Equation Turbulent_Kinetic_Energy

               First Order Upwind Factor = 0.0  For Equation X_momentum
               First Order Upwind Factor = 0.0  For Equation Y_momentum
               First Order Upwind Factor = 0.0  For Equation Z_momentum
               First Order Upwind Factor = 0.0  For Equation Mixture_Fraction
               First Order Upwind Factor = 0.0  For Equation Turbulent_Kinetic_Energy
```

```
               Hybrid Upwind Factor = 0.0 For Equation X_momentum
               Hybrid Upwind Factor = 0.0 For Equation Y_momentum
               Hybrid Upwind Factor = 0.0 For Equation Z_momentum
               Hybrid Upwind Factor = 0.1 For Equation Mixture_Fraction
               Hybrid Upwind Factor = 0.1 For Equation Turbulent_Kinetic_Energy

$ how will this work?
           Maximum Wall time = 47.9 hours

$-----------------------------------------------
$              Specify under-relaxation
$-----------------------------------------------
               Under Relax Momentum By 1.0
               Under Relax Pressure By 1.0
               Under Relax Turbulent_Kinetic_Energy by 1.0

$-----------------------------------------------
$              Define turbulence model
$-----------------------------------------------
               Begin Turbulence Model Specification
$                   Turbulence Model = Dsmag
$                   Under Relax Turbulent_viscosity By 0.7

                    Turbulence Model = Ksgs
                    Under Relax Turbulent_viscosity By 0.75
                    Include Molecular Viscosity  In  K-E Diffusion Coefficient


               End   Turbulence Model Specification

$-----------------------------------------------
$              Define buoyancy model
$-----------------------------------------------
$               Begin Buoyancy Model Specification Bouyant
$                   Buoyancy Reference Temperature = 294.15
$                   Buoyancy Model = Differential

$               End   Buoyancy Model Specification

$-----------------------------------------------
$              Define darcy flow
$-----------------------------------------------

         # specify properties for the solid phase
         BEGIN MULTIPHASE MODEL SPECIFICATION myMult
            # turn on model for porous media (Darcy flow)
            ENABLE POROUS MEDIA MODEL
            multiphase particle_diameter = 0.001
            multiphase solid_velocity = 0.0
         END MULTIPHASE MODEL SPECIFICATION myMult

            End   Solution Options

$-------------------------------------------------------
$           Specify which mesh model to use for this region
$-------------------------------------------------------
            Use Finite Element Model Water_flow

$-----------------------------------------------
$           Specify initial conditions
$-----------------------------------------------
            Begin Initial Condition Block IC_block
                Volume Is block_1
                Pressure = 0.0
                X_velocity = 0.0
                Y_velocity = 0.0
                Z_velocity = 0.0
                Temperature = 294.15
                Mixture_Fraction = 0.0
                Turbulent_Kinetic_Energy = 1e-6
                function for gas_volume_fraction = gasVolFcn IN THE Z DIRECTION
```

```
            End   Initial Condition Block IC_block

$-------------------------------------------------
$           Define boundary conditions
$-------------------------------------------------

            # Inflow
            Begin Inflow Boundary Condition On Surface surface_3

        external field for x_velocity = x_velocitya
        external field for y_velocity = y_velocitya
        external field for z_velocity = z_velocitya

$                X_velocity = 0.0
$                Y_velocity = 0.0
$                Z_velocity = .323 $ avg from inlet data
$                function for Z_velocity = inlet_vel20 IN THE X DIRECTION
                Temperature = 294.15
                Mixture_Fraction = 0.0
                Turbulent_Kinetic_Energy = 1.0e-6

            End   Inflow Boundary Condition On Surface surface_3


            # Inflow-secondary
            Begin Inflow Boundary Condition On Surface surface_6
                X_velocity = 0.0
                Y_velocity = .044 $ avg injection velocity (given)
                Z_velocity = 0.0
                Temperature = 294.15
                Mixture_Fraction = 1.0
                Turbulent_Kinetic_Energy = 1e-6

            End   Inflow Boundary Condition On Surface surface_6

            # Open
            Begin Open Boundary Condition On Surface surface_1
                Pressure = 0.0
                Temperature = 294.15
                Mixture_Fraction = 0.0
                Turbulent_Kinetic_Energy = 1e-6 $ low TI

            End   Open Boundary Condition On Surface surface_1


            # Wall Surface sides
            Begin Wall Boundary Condition On Surface surface_2
                Temperature = 294.15
                post process yplus
            End   Wall Boundary Condition On Surface surface_2

            # Wall Surface (ground)
            Begin Wall Boundary Condition On Surface surface_4
                Temperature = 294.15
                post process yplus
            End   Wall Boundary Condition On Surface surface_4

            # Wall Surface (top)
            Begin Wall Boundary Condition On Surface surface_5
                Temperature = 294.15
                post process yplus
            End   Wall Boundary Condition On Surface surface_5



$-------------------------------------------------------
$           Define parameters for checkpoint/restart file
$-------------------------------------------------------
            Begin Restart Data Restart
                Input Database Name = rsout/waterChannel.rsout
                Output Database Name   = rsout/waterChannel.rsout
```

```
                At Time 2.5 Increment = 2.5
                exists = add_suffix
            End   Restart Data Restart

      BEGIN AVERAGING AVG
        REYNOLDS AVERAGE FIELD X_velocity AS ru
        REYNOLDS AVERAGE FIELD Y_velocity AS rv
        REYNOLDS AVERAGE FIELD Z_velocity AS rw
        REYNOLDS AVERAGE FIELD mixture_fraction AS avg_mix
        REYNOLDS AVERAGE FIELD yplus as avg_yp
        STARTING TIME = 5.1
      END AVERAGING AVG

$=====================================================================
$
$  Begin the heartbeat output for this region
$
$=====================================================================

            Begin Heartbeat Output out_1
                Stream Name is flow_mid.txt
$                At Time 0.0 Interval is 0.01
                At Step 0, Increment = 1
                Variable is Global time as Time
                Variable is Node mixture_fraction nearest location -0.0086620580695 -
0.03587499818206 -0.06829640269279 as conc
                Variable is Node x_velocity nearest location -0.0086620580695 -0.03587499818206 -
0.06829640269279 as u
                Variable is Node y_velocity nearest location -0.0086620580695 -0.03587499818206 -
0.06829640269279 as v
                Variable is Node z_velocity nearest location -0.0086620580695 -0.03587499818206 -
0.06829640269279 as w
                Termination Time is 360.0
            End Heartbeat Output out_1

            Begin Heartbeat Output out_1
                Stream Name is flow_bottom.txt
$                At Time 0.0 Interval is 0.01
                At Step 0, Increment = 1
                Variable is Global time as Time
                Variable is Node mixture_fraction nearest location -0.0086620580695 -
0.04812499818206 -0.06829640269279 as conc
                Variable is Node x_velocity nearest location -0.0086620580695 -0.04812499818206 -
0.06829640269279 as u
                Variable is Node y_velocity nearest location -0.0086620580695 -0.04812499818206 -
0.06829640269279 as v
                Variable is Node z_velocity nearest location -0.0086620580695 -0.04812499818206 -
0.06829640269279 as w
                Termination Time is 360.0
            End Heartbeat Output out_1

            Begin Heartbeat Output out_1
                Stream Name is flow_top.txt
$                At Time 0.0 Interval is 0.01
                At Step 0, Increment = 1
                Variable is Global time as Time
                Variable is Node mixture_fraction nearest location -0.0086620580695 -
0.02362499818206 -0.06829640269279 as conc
                Variable is Node x_velocity nearest location -0.0086620580695 -0.02362499818206 -
0.06829640269279 as u
                Variable is Node y_velocity nearest location -0.0086620580695 -0.02362499818206 -
0.06829640269279 as v
                Variable is Node z_velocity nearest location -0.0086620580695 -0.02362499818206 -
0.06829640269279 as w
                Termination Time is 360.0
            End Heartbeat Output out_1



$-------------------------------------------------
$           Define contents of binary plot file
```

```
$-------------------------------------------------
            Begin Results Output Label Output
                Database Name = exodus/waterChannel.e
                At Time 0.0, Increment = 1
                At Time 5, Increment = 0.025
                At Time 10, Increment = 0.01
                At Time 13, Increment = 0.1
                Title Flow Around Building Array
                Nodal Variables = X_velocity As U-x
                Nodal Variables = Y_velocity As U-y
                Nodal Variables = Z_velocity As U-z
                Nodal Variables = Pressure As P
                Nodal Variables = Mixture_Fraction As Mix
                Nodal Variables = Turbulent_Kinetic_Energy As Tke
                Nodal Variables = Turbulent_viscosity As Tmu
                Nodal Variables = yplus
$                NODAL Variables = gas_volume_fraction AS gasVol
                exists = add_suffix
            End   Results Output Label Output

            Begin Results Output Label Output2
                Database Name = exodus/waterChannel2.e
                At Time 20.0, Increment = .05
                Title Flow Around Building Array

                NODAL Variables = ru As reynolds_x
                NODAL Variables = rv As reynolds_y
                NODAL Variables = rw As reynolds_z
                NODAL Variables = avg_mix
                NODAL Variables = avg_yp
                exists = add_suffix
         End   Results Output Label Output2


        End   Fuego Region Fuego_region

        BEGIN INPUT_OUTPUT REGION average_refgion

            USE FINITE ELEMENT MODEL output_plane

$             Begin Results Output Label output
$                 DATABASE Name = exodus/outputplanedummy.e
$                 At Time 0.0 Interval is 0.1
$                 At Time 1200.0 Interval is 1.0
$                 TITLE XTF problem test
$                 NODAL Variables = pressure       AS Press
$                 NODAL Variables = x_velocity     AS U-x
$                 NODAL Variables = y_velocity     AS U-y
$                 NODAL Variables = z_velocity     AS U-z
$                 NODAL Variables = gas_volume_fraction AS gasVol
$                 NODAL Variables = temperature    AS T
$                 NODAL Variables = density     As D
$$                 NODAL Variables = radiative_flux
$                 NODAL Variables = mass_fraction AS Y
$                 NODAL Variables = soot AS Soot
$                 NODAL Variables = turbulent_kinetic_energy AS tke
$$                 NODAL Variables = turbulent_dissipation AS ted
$
$             End   Results Output Label output
$             create nodal field x_velocitya of type real and dimension 1
$             create nodal field y_velocitya of type real and dimension 1
$             create nodal field z_velocitya of type real and dimension 1


        END   INPUT_OUTPUT REGION average_refgion
        BEGIN INPUT_OUTPUT REGION average_region1

            USE FINITE ELEMENT MODEL output_plane1

            create nodal field ru of type real and dimension 1
            create nodal field rv of type real and dimension 1
```

```
            create nodal field rw of type real and dimension 1

            Begin Results Output Label output
                DATABASE Name = exodus/outputplanedummy.e
                At Time 0.0 Interval is 0.1
                At Time 1200.0 Interval is 1.0
                TITLE XTF problem test
$                NODAL Variables = pressure       AS Press
$                NODAL Variables = x_velocity     AS U-x
$                NODAL Variables = y_velocity     AS U-y
$                NODAL Variables = z_velocity     AS U-z
                NODAL Variables = ru
                NODAL Variables = rv
                NODAL Variables = rw
$                NODAL Variables = gas_volume_fraction AS gasVol
$                NODAL Variables = temperature    AS T
$                NODAL Variables = density     As D
$                NODAL Variables = radiative_flux
$                NODAL Variables = mass_fraction AS Y
$                NODAL Variables = soot AS Soot
$                NODAL Variables = turbulent_kinetic_energy AS tke
$$                NODAL Variables = turbulent_dissipation AS ted
                exists = add_suffix

            End   Results Output Label output

        END   INPUT_OUTPUT REGION average_region1


    End   Fuego Procedure Fuego_procedure

End   Sierra Fuego
```

This page left blank

APPENDIX B. ADDITIONAL PLOTS

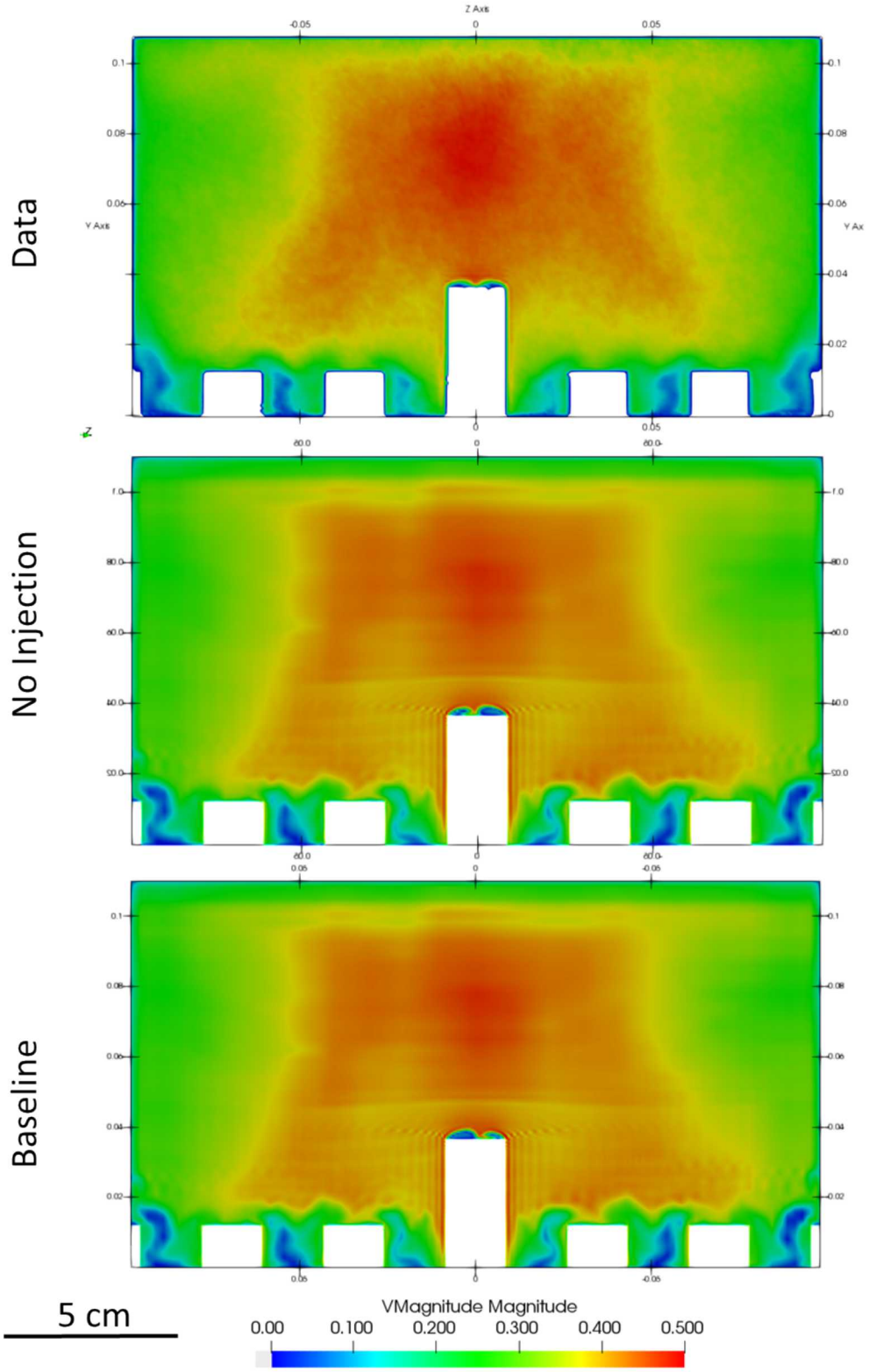

Appendix_Figure 1-1. Velocity Magnitude data and Predictions for the Baseline LES

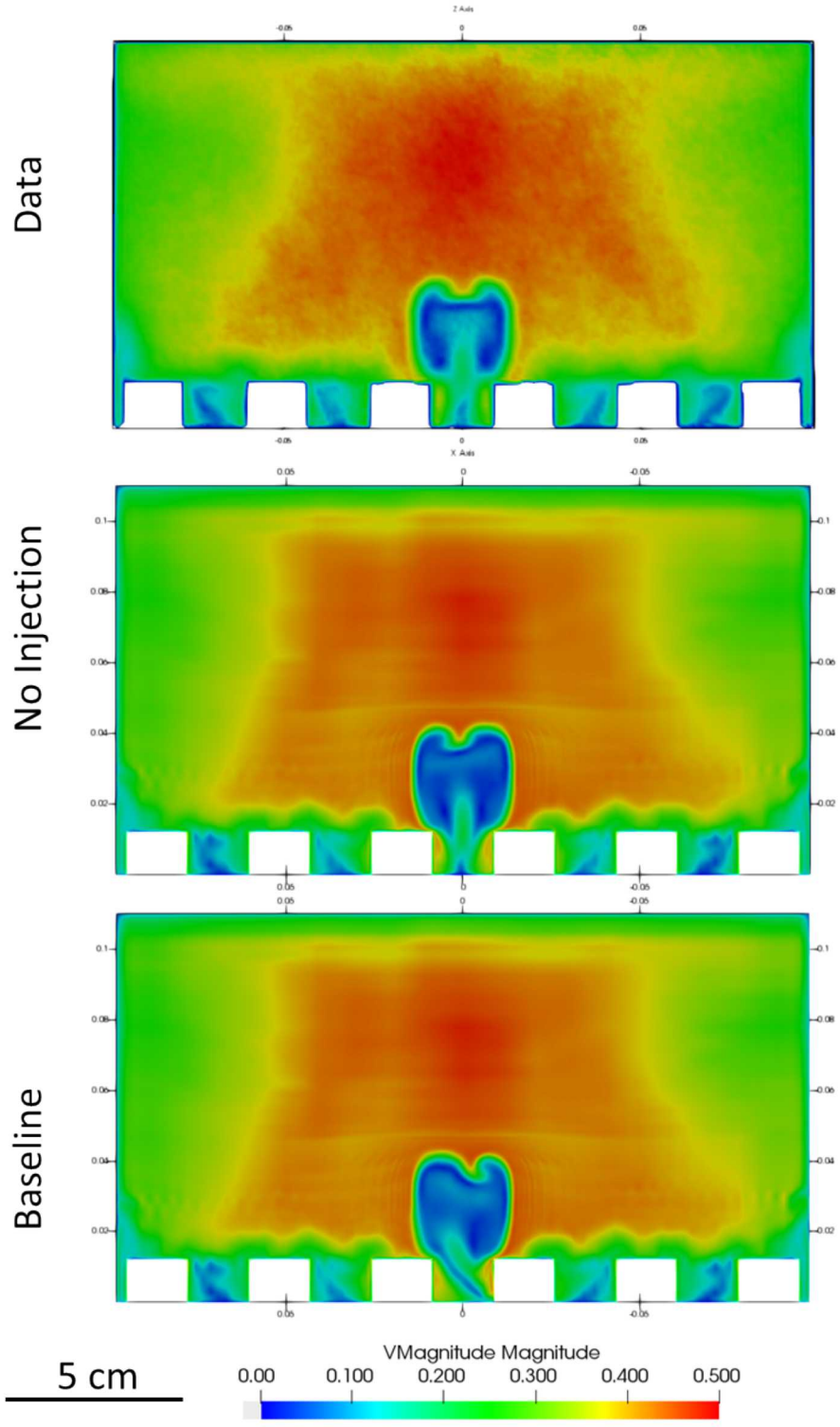

Appendix_Figure 1-2. Velocity Magnitude Data and Predictions for the 4 Plane

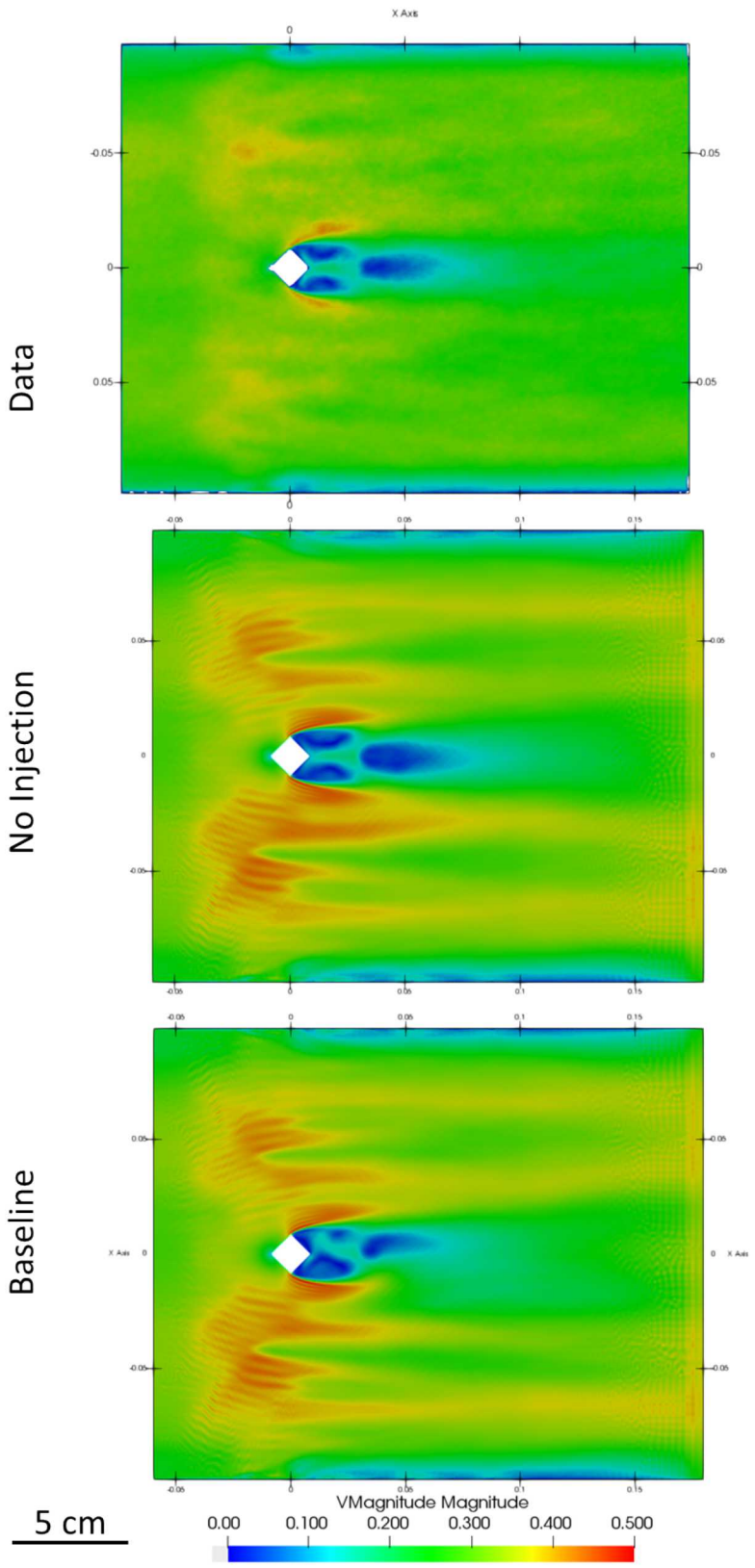

Appendix_Figure 1-3. Velocity Magnitude Data and Predictions for the 3/6 H Plane

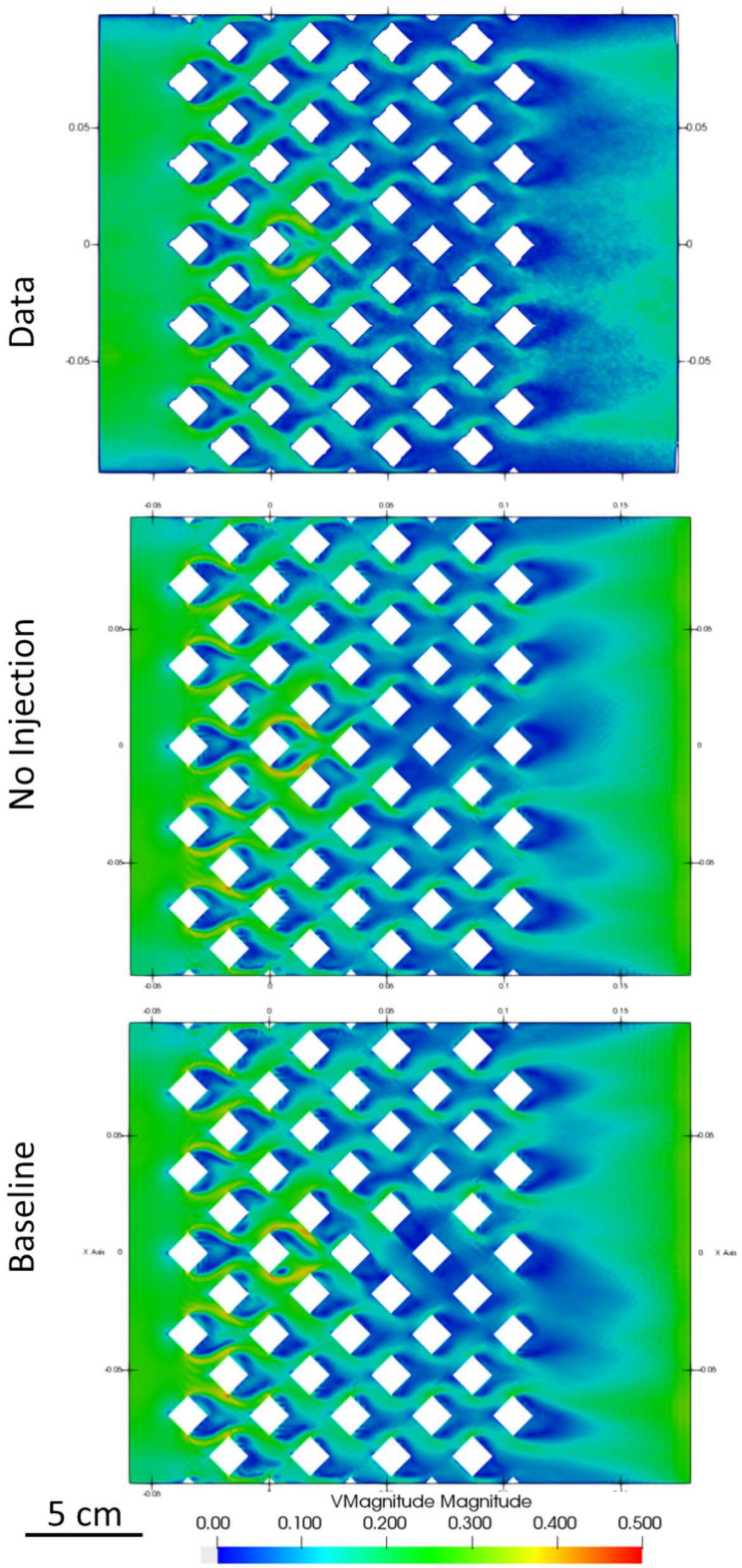

Appendix_Figure 1-4. Velocity Magnitude Data and Predictions for the 1/6 H Plane

Similar comparison plots are produced for the three vector components as were produced for the velocity magnitude and concentration. Appendix_Figure 1-5 shows the x-velocity (spanwise)

component compared between model and simulation. These results are poor, with neither the slope nor the R2 suggesting similarity between the two. The experiment suggests a negatively biased x-velocity, with peak magnitudes about double that of the positive direction. The simulations suggest a more uniform distribution of the velocity about the zero. X-velocity may be the most difficult component to predict correctly in this model, as the flow was not induced in this direction and only varies based on the aerodynamic movement around the objects. The other two component results compare better, with the y-velocity (Appendix_Figure 1-6) and z-velocity (Appendix_Figure 1 7) with slopes significantly closer to unity, but R2 values suggesting mixed results. Comparisons are best in the z-direction, with the highest R2 and the slope closest to unity.

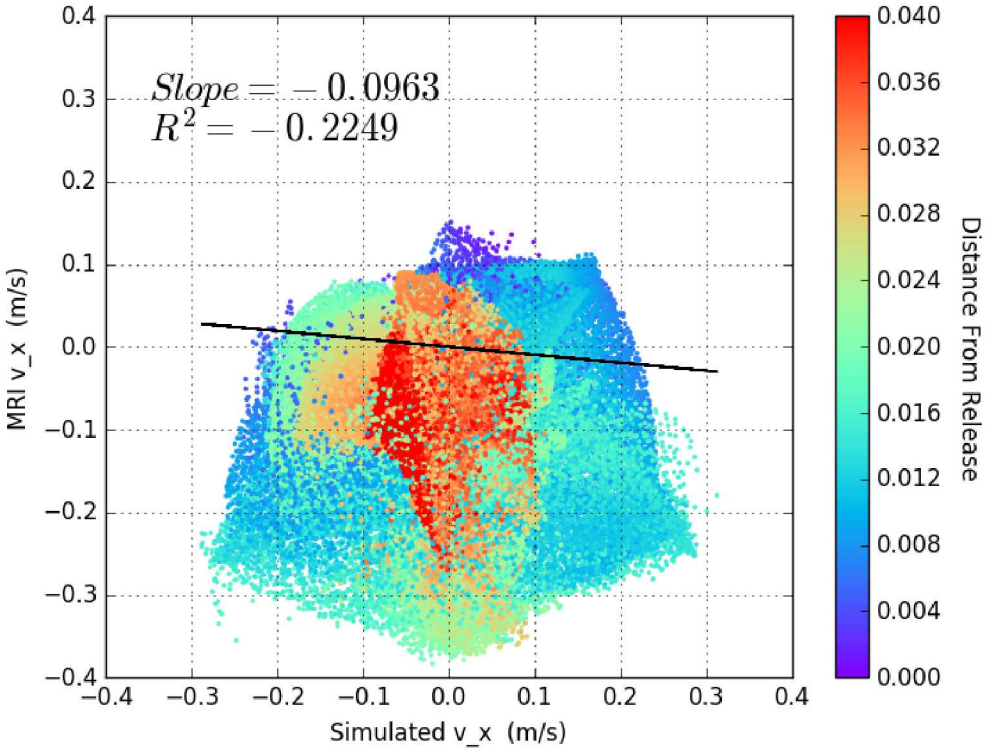

Appendix_Figure 1-5. 3D Comparison of the X-Velocity for a 0.025 Concentration Clip

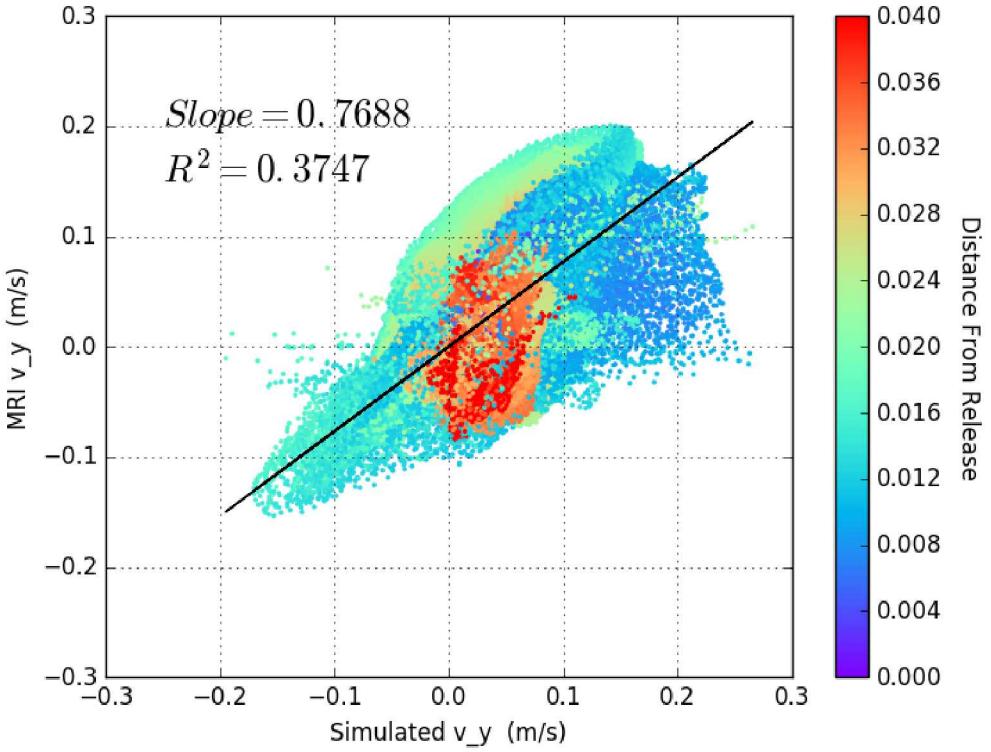

Appendix_Figure 1-6. 3D Comparison of the y-Velocity for a 0.025 Concentration Clip

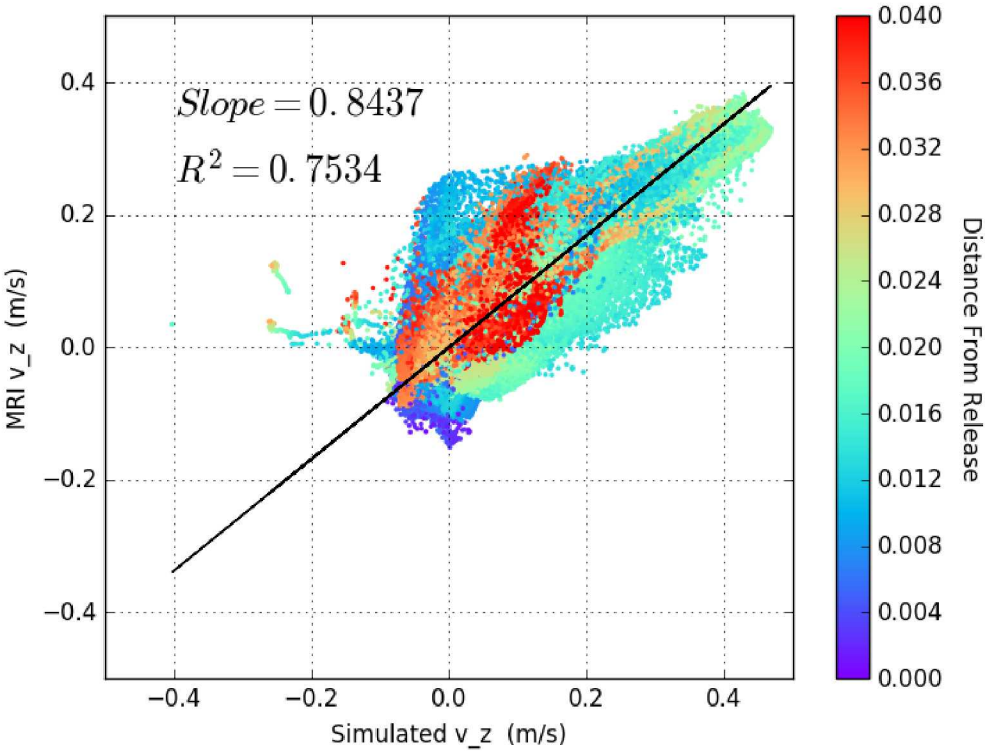

Appendix_Figure 1 7. 3D Comparison of the z-Velocity for a 0.025 Concentration Clip

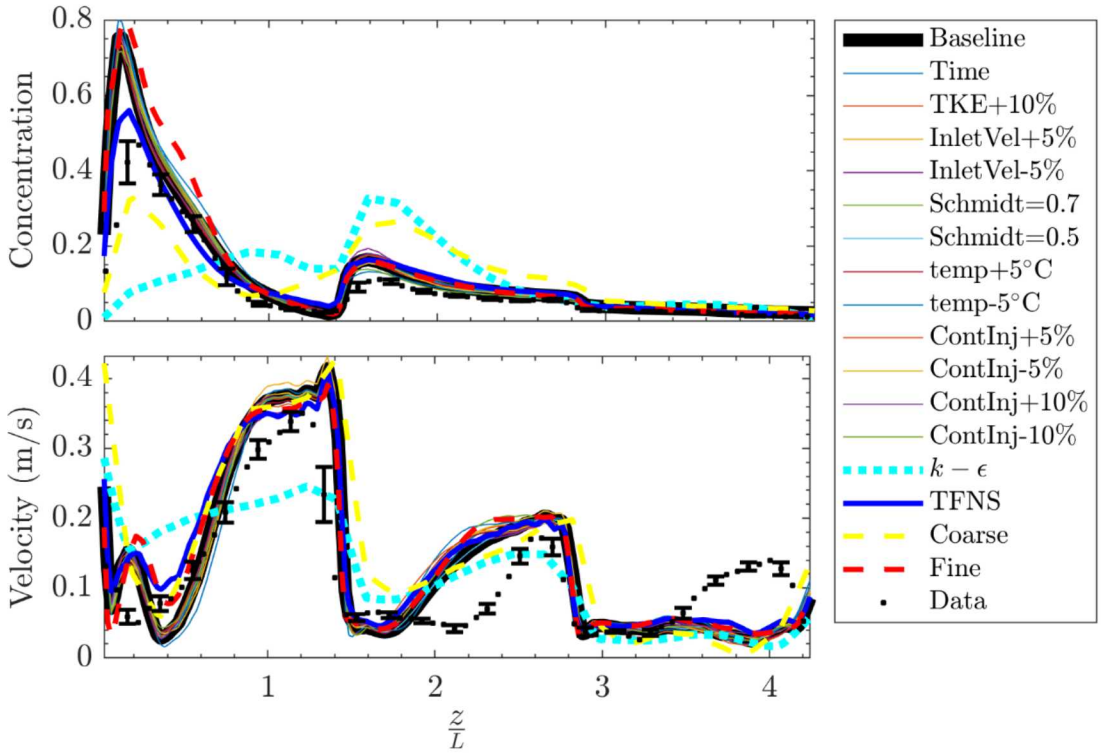

Appendix_Figure 1 8. All Concentration (Top) and Velocity Magnitude (Bottom) Simulation Results with Experimental Data for a Streamwise Line at 1/6 H

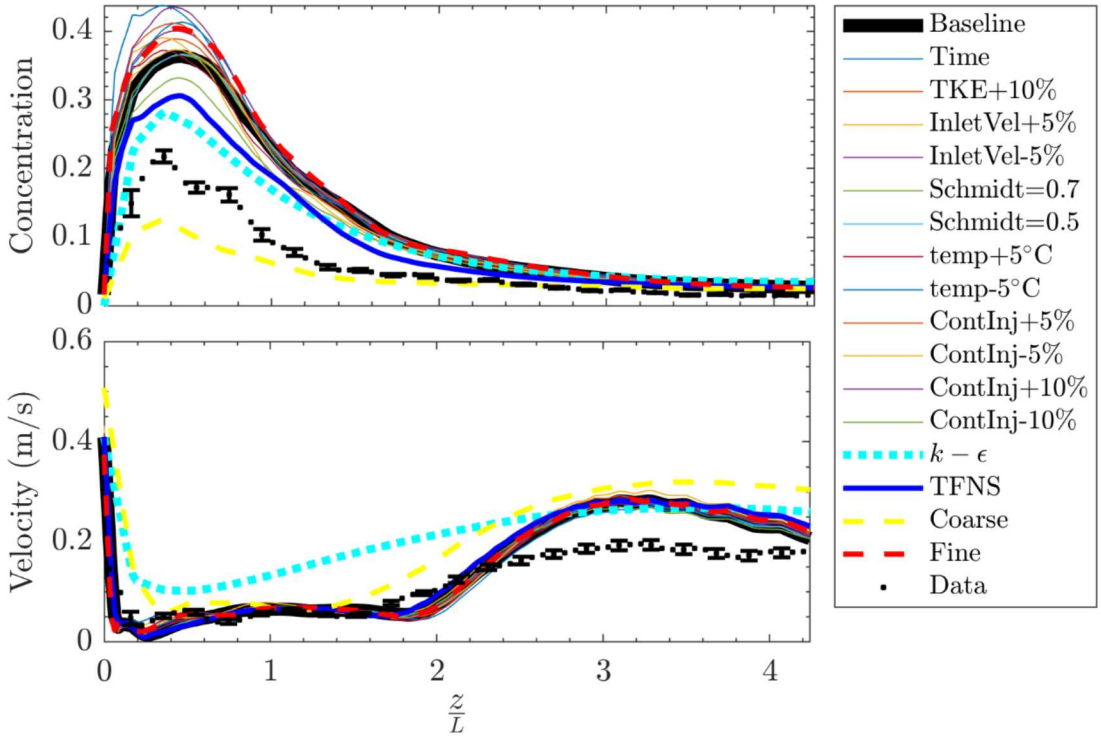

Appendix_Figure 1 9. All Concentration (Top) and Velocity Magnitude (Bottom) Simulation Results with Experimental Data for the Streamwise Line at 1/2 H

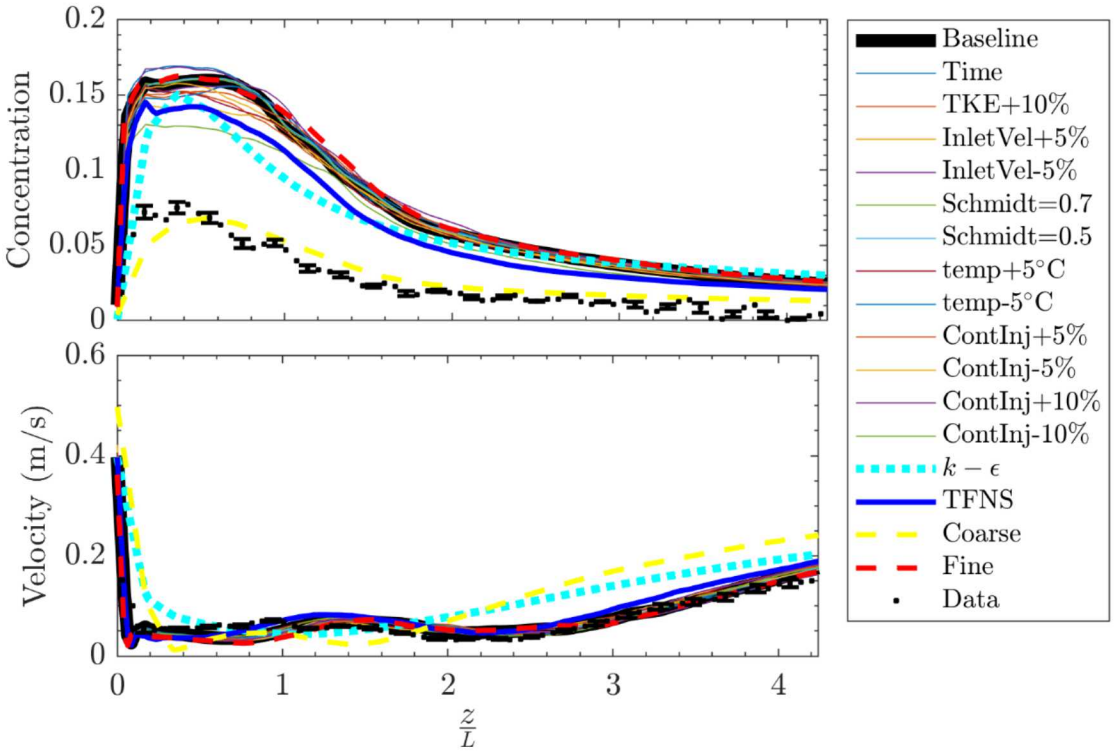

Appendix_Figure 1 10. All Concentrate (Top) and Velocity Magnitude (Bottom) Simulation Results with Experimental Data for the Streamwise Line at 5/6 H

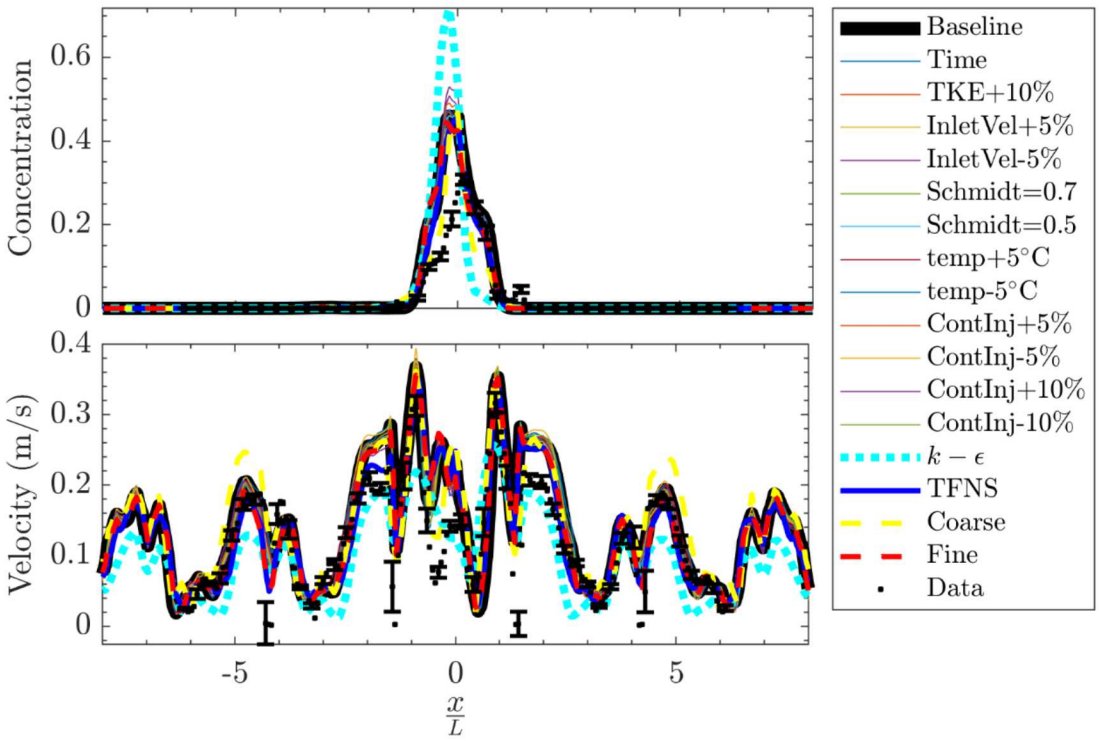

Appendix_Figure 1 11. All Concentration (Top) and Velocity Magnitude (Bottom) Simulation Results with Experimental Data for the Spanwise Line at 1/6 H

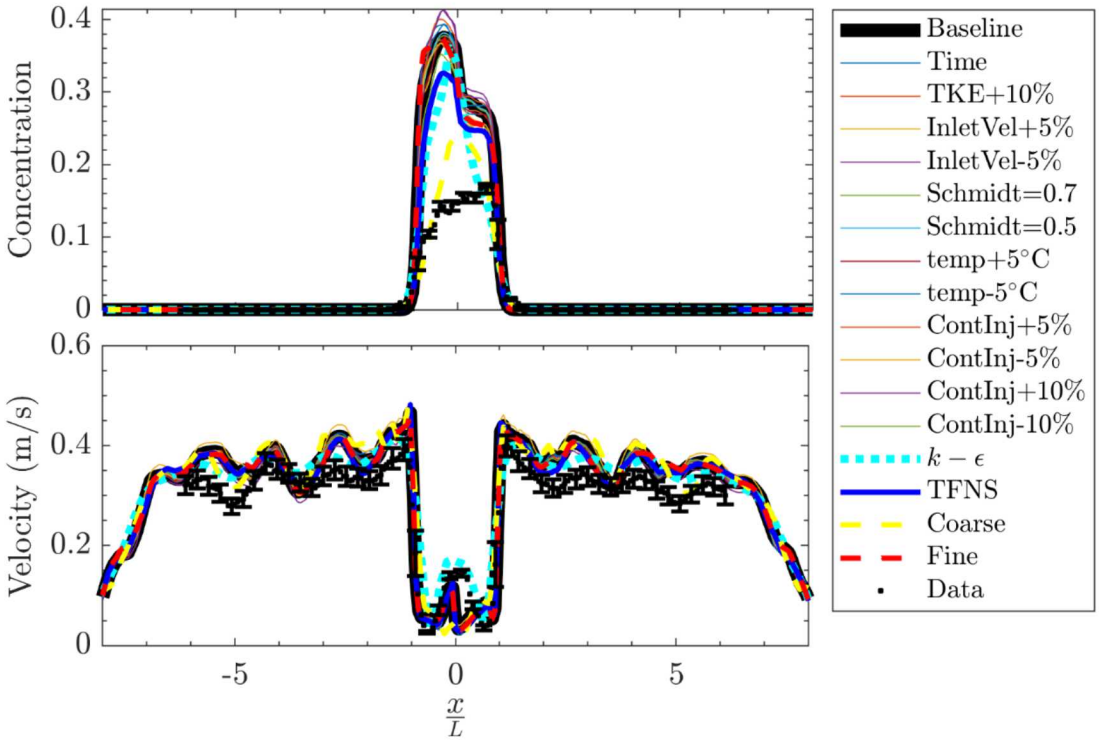

Appendix_Figure 1 12. All Concentration (Top) and Velocity Magnitude (Bottom) Simulation Results with Experimental Data for the Spanwise Line at 1/2 H

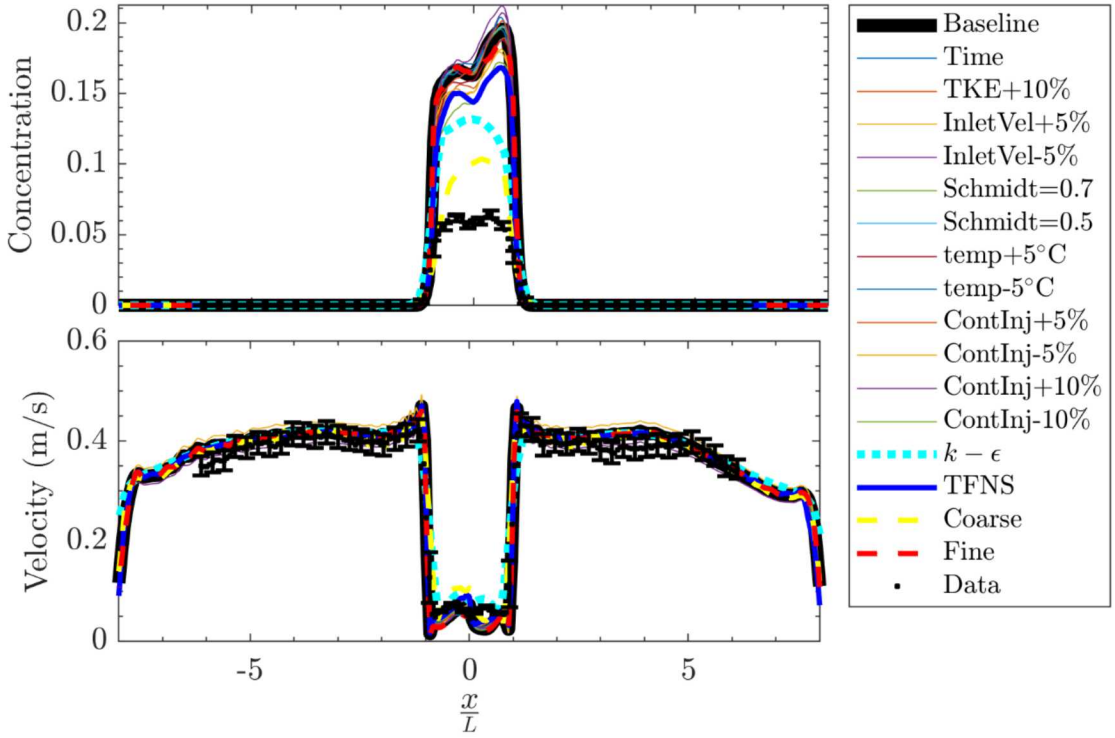

Appendix_Figure 1 13. All Concentration (Top) and Velocity Magnitude (Bottom) Simulation Results with Experimental Data for the Spanwise Line at 5/6 H

DISTRIBUTION

Email—Internal

Name	Org.	Sandia Email Address
Michael Clemenson	6772	mdcleme@sandia.gov
Paul Crozier	1541	pscrozi@sandia.gov
Ann Dallman	6775	ardallm@sandia.gov
Kevin Dowding	1544	kjdowdi@sandia.gov
Andrew Glen	6633	aglen@sandia.gov
Neal Grieb	2471	npgrieb@sandia.gov
Dale Jackson	6772	dcjacks@sandia.gov
Andrew Kurzawski	1532	akurzaw@sandia.gov
Blake Lance	1544	blance@sandia.gov
Carlos Lopez	1532	carlope@sandia.gov
Anay Luketa	1532	aluketa@sandia.gov
Jeff Mercier	6770	jamerci@sandia.gov
Karen Rogers	1530	ksroger@sandia.gov
Angel Urbina	1544	aurbina@sandia.gov
Tyler Voskuilen	1541	tvoskui@sandia.gov
Technical Library	01977	sanddocs@sandia.gov

Email—External (encrypt for OUO)

Name	Company Email Address	Company Name
Col. Mike Benson	Michael.benson@westpoint.edu	U.S. Military Academy
Chris Elkins	celkins@stanford.edu	Stanford University
Sam Jones	Samuel.jones@slcc.edu	Salt Lake Community College

This page left blank

This page left blank

Sandia National Laboratories

Sandia National Laboratories is a multimission laboratory managed and operated by National Technology & Engineering Solutions of Sandia LLC, a wholly owned subsidiary of Honeywell International Inc. for the U.S. Department of Energy's National Nuclear Security Administration under contract DE-NA0003525.